Spring 1-1-2019

Daily GRACE Water Storage Estimates for Improving Hydrology Models and Forecasting

Michael Joseph Croteau
University of Colorado at Boulder, croteaumj@gmail.com

Daily GRACE Water Storage Estimates for Improving Hydrology Models and Forecasting

by

Michael J. Croteau

B.S., University of Notre Dame, 2010

M.Ed., University of Notre Dame, 2012

M.S., University of Colorado Boulder, 2014

A thesis submitted to the

Faculty of the Graduate School of the

University of Colorado in partial fulfillment

of the requirements for the degree of

Doctor of Philosophy

Ann and H. J. Smead Department of Aerospace Engineering Sciences

2019

This thesis entitled:
Daily GRACE Water Storage Estimates for Improving Hydrology Models and Forecasting
written by Michael J. Croteau
has been approved for the Ann and H. J. Smead Department of Aerospace Engineering Sciences

Prof. R. Steven Nerem

Dr. Bryant Loomis

Prof. Jay McMahon

Prof. Tomoko Matsuo

Prof. Ben Livneh

Date

The final copy of this thesis has been examined by the signatories, and we find that both the content and the form meet acceptable presentation standards of scholarly work in the above mentioned discipline.

Croteau, Michael J. (Ph.D., Aerospace Engineering Sciences)

Daily GRACE Water Storage Estimates for Improving Hydrology Models and Forecasting

Thesis directed by Prof. R. Steven Nerem

Abstract

The Gravity Recovery and Climate Experiment (GRACE) has created a more than 15 year record of time variable gravity and enabled studies of regional terrestrial water storage (TWS) changes. These and other studies have primarily been limited to analyses of long wavelength signals due to the inherent 30-day temporal resolution associated with the majority of GRACE products. This dissertation seeks to improve on this limitation by creating a daily estimate of TWS using mass concentrations (mascons) as an iteration of the Goddard Space Flight Center's (GSFC) monthly global mascon product. The developed solution couples the 30-day high spatial resolution of that product with lower spatial resolution daily estimates. Key to this study is the development of an optimized regularization strategy for resolving daily fields that maximizes signal recovery and a characterization of bias in the solution due to this regularization. A rigorous analysis shows that the resulting daily estimated mascons have latitudinally-dependent resolution, with approximately 450 km spatial resolution in polar regions and 800-1,200 km spatial resolution at low latitudes. This analysis shows strong signal recovery relative to bias effects for basins larger than 800,000 km^2 and marginal recovery for basins 300,000-800,000 km^2, while signal recovered in basins smaller than 250,000 km^2 are dominated by bias errors. The solution developed in this dissertation is the first daily TWS product with global land coverage estimated from individual daily GRACE Level-1B observations.

Acknowledgements

First, I would like to sincerely thank my advisor, Prof. Steve Nerem, for his support throughout my graduate school career. Entering grad school, I knew I wanted to work on something related to astrodynamics, and preferably something in the Earth Sciences. I would not have had the chance to succeed in satellite geodesy if not for Steve's influence and advice. I'm grateful that he took a chance on me, a high school math teacher with practically no astrodynamics or geodesy experience.

I'd like to thank Prof. Jay McMahon, Prof. Tomoko Matsuo, Prof. Ben Livneh, and Dr. Bryant Loomis for serving on my Ph.D committee and for their advice and support from my Comprehensive Exam through to the completion of my dissertation. I'd especially like to thank Dr. Bryant Loomis, who has served as a mentor and second advisor to me throughout grad school at CU and summers at GSFC and has been a friend and fellow baseball fan.

Thank you to Scott Luthcke for his support over multiple summers at GSFC and throughout my time in grad school, to Terry Sabaka and Andy Griffin for their help and great discussions during summers at GSFC, to David Wiese and Phil Thompson for their support and collaborations, to Prof. David Go for encouraging me to pursue grad school, and to all my CU and ND professors.

Thank you so much to my parents, Joe and Marcia Croteau, and my sister and her husband, Angela and Greg Marx, who have always loved and supported me. Also, thanks to my friends, particularly Greg Lucas, Dimitri Krattiger, Matt Talpe, Ryan Hardy, Jake Larson, John Fullard, Sean Quinn, Jennifer King, and Keaton Van Beveren, as well as the whole Nerem group.

Finally, thank you to NASA Headquarters for their support of this work under the NASA Earth and Space Science Fellowship, Grant NNX16AO35H.

Contents

Chapter

Tables

Table

Figures

Figure

Chapter 1

Introduction

We live in a dynamic world, driven not just by our day-to-day activities but often more so by the environment around us. Earth's climate sustains life and makes a thriving human society possible, but day-to-day weather patterns and longer-term climate variations mean that we live in a world where we must constantly seek to improve our understanding of our planet and how we interact with it. No climate component impacts us more than water, as precipitation and water availability, drought and flooding, snow and ice storage and melt, and local and global sea level are all dynamic systems driven by redistributions of water globally. These and innumerable other components of the global water cycle impact nearly every person on Earth, from municipal water managers seeking to best regulate local water supplies, to coastal communities seeking to understand local sea level rise, to farmers whose entire annual income can hinge on proper drought planning. Importantly, these water cycle impacts pose the greatest risk to the poorest communities around the world, where flooding, drought, coastal erosion, and much more can devastate communities with none of the needed resources to recover and rebuild. Therefore, if we as a society want to secure the future livelihoods of everyone from the richest coastal towns to the poorest flood- or drought-prone communities, we must start by understanding these water signals, and therefore must determine ways to quantify these changes on the long-term (secular), seasonal, and short-term levels.

Over the past few decades, scientists have developed numerous ways to better understand where water is (and is not) and how water storage changes over time. *In situ* measurements of soil moisture, local sea level and tides, precipitation, river and lake levels, and more provide

excellent local relative measurements, allowing individuals, municipalities, and scientists to better understand local water challenges. However, such measurements come with a challenge that is difficult to overcome: to understand the global water cycle, we need global measurements. While local measurements in first world municipal areas are often taken for granted, collecting such measurements across remote or poor areas becomes logistically impossible *in situ*. And even where we have good knowledge of surface water variability, having an equally good understanding of groundwater storage variability poses further challenges. Global measurement systems are needed, and satellite remote sensing provides a solution.

1.1 Remotely sensing Earth signals via satellite observations

In order to create a global understanding of water-related climate variables, numerous satellite missions have been launched over the past few decades, each tasked with observing a specific part of the water-driven climate. Radar altimetry missions including multiple OSTM/Jason missions have enabled records of the ocean's mean sea surface, changing sea surface height anomalies, global mean sea level, and anthropogenic sea level rise from 1992-present (*Nerem et al.*, 2010; *Church and White*, 2011; *Hamlington et al.*, 2014, and others). Laser and radar altimetry missions such as ICESat and CryoSat-2 have quantified polar ice heights and ice sheet evolution (*Shuman et al.*, 2006; *Shepherd et al.*, 2012; *Zwally et al.*, 2015, and others). Over land, other missions have used interferometric synthetic-aperture radar or optical measurements to target soil moisture, vegetation, and other surface water measurements to improve our knowledge of hydrological systems. These missions have proven successful in their own right, but their contributions are limited to surface mass variations. No single one of these missions can capture the total water column of an area, including water trapped in the canopy and top layers of soil through river and lake systems and into the deepest parts of groundwater and aquifers. To measure this complete picture of terrestrial water storage (TWS), NASA and the German Aerospace Center, Deutsches Zentrum fr Luft- und Raumfahrt

(DLR), partnered together to launch the Gravity Recovery and Climate Experiment (GRACE) mission, tasked with measuring and mapping Earth's time-variable gravity field (*Tapley et al.*, 2004a). Gravity, the attraction of two objects with mass, varies spatially as mass on the Earth's surface varies geographically and in time as surface water and ice mass transport continuously redistribute surface mass.

1.2 Geodesy

Outside the specialized field of Geodesy and certain surrounding physical science fields, gravity as a concept is both fairly abstract and relatively simple. Anyone fortunate enough to have completed a high school physics curriculum will be familiar with Newton's Universal Law of Gravitation and understand that gravity is the natural result of two bodies of non-zero mass acting on one another through a form of mutual attraction (*Newton*, 1687; *National Governors Association Center for Best Practices*, 2010). With such an understanding, gravity is often considered a constant value on Earth's surface and that it changes inversely with the square of the distance between the two bodies. However, Earth's gravitational field is not due to a point mass located at the center of the Earth or a single value that can be considered as a constant, as in many simple kinematics applications. Instead, in the field of Geodesy - by one definition "a branch of applied mathematics concerned with the determination of the size and shape of the earth and the exact positions of points on its surface and with the description of variations of its gravity field" (*Merriam-Webster*) - we focus on variations in gravity of Earth and other planetary bodies, spatially and in time.

As a field, Geodesy dates back to ancient times, to the first Greek philosophers interested in Earth's shape, who questioned if the Earth was flat or round. A more modern landmark in the evolution of the field of Geodesy came in the 1700s, when the Acadèmie Royale des Sciences tasked two missions with studying Earth's precise shape by measuring the variation in a degree of latitude at the equator and the North Pole, a story told with intriguing historical context in *Hoare*

(2005). To summarize that endeavor, by the 1700s Earth's roundness was well understood, but new controversy existed as to the nature of that roundness. Namely, was Earth spherical or ellipsoidal, and if the latter, was it an oblate or prolate ellipsoid? Newton and others suggested an oblate ellipsoid due to Earth's rotational forces, but others disagreed. The two missions, one led by Louis Godin and Pierre Bouguer (after whom the *Bouguer anomaly* is named, a gravitational anomaly due to the height at which gravity is measured and local terrain effects) to equatorial Peru and the other by Pierre Louis Moreau de Maupertuis to the Arctic, proved Earth's oblateness, or equatorial bulge. In doing so, the field of Geodesy made an extraordinary leap forward in our knowledge of Earth. Since then, countless work has been done refining our understanding of Earth's size, shape, and gravity field.

One of the major advances resulting from the French missions to measure Earth's oblateness was the rise to prominence of gravimetry in measuring Earth's shape and constraining density models of Earth's interior, as told in *Nerem et al.* (1995). As technological advances made gravimetric devices more precise and more easily transportable, leaps forward in surveying and defining the terrestrial reference frame were made. With the dawn of the satellite era in 1957 when Sputnik first orbited the Earth, orbital tracking measurements became available to see the global effects of Earth gravity on satellites, and in turn better characterize those gravitational effects. These measurements, in conjunction with airborne and terrestrial gravimetry, have led to increasingly more precise understandings of gravitational variations around the Earth.

Satellite geodesy as a science dates to the earliest satellites, whose observed orbital perturbations due to Earth's non-uniform gravity field improved models of Earth's shape and structure. NASA's Apollo missions displayed an early need for planetary geodesy, as large mass anomalies on the surface of the Moon posed real challenges in Lunar orbital maneuvering. Deep Space Network tracking was used to observe orbital perturbations in Lunar orbit and advance surface mass models of the Moon to ensure astronaut safety during orbit and landings (*Muller and Sjogren*, 1968). As soon as the mid-1970s, satellite missions were flown specifically for geodesy purposes, with the Laser Geodynamics Satellite (LAGEOS-1) launch in 1976 marking the first of many spherical satellites

covered in retroreflectors to enable high precision laser ranging from Earth, and in turn very accurately measure orbital perturbations due to Earth's gravity field. Like in lunar orbit, a very good understanding of gravitational perturbations in Earth orbit allows orders of magnitude improvements to precise orbit determination, vital in almost all applications of spaceflight. Since then, newer and more advanced missions designed to characterize Earth's gravitational field have taken flight, highlighted by the Gravity Field and Steady-State Ocean Circulation Explorer (GOCE) mission, which mapped what remains our most precise estimate of Earth's mean gravity field, and GRACE's measurements of time-variable gravity (*Pail et al.*, 2010; *Tapley et al.*, 2004a). An interesting piece of trivia related to satellite geodesy arising from these many numerous missions is that Earth is not the planetary body whose global gravity field is most well understood . Instead, thanks to the Gravity Recovery and Interior Laboratory (GRAIL) mission, our understanding of the lunar gravity field is at a significantly higher resolution than Earth (though very precise local geodetic measurements mean that certain portions of Earth's gravity may be more well understood), as the lack of a Lunar atmosphere allowed that mission to fly much closer to the lunar surface and the time-variable elements of the lunar gravity field are much slower processes than on Earth (*Lemoine et al.*, 2013; *Brown and McDonnell*, 2012; *Drake*, 2012).

1.3 The Gravity Recovery and Climate Experiment

The GRACE mission was launched March 17, 2002 as a joint-venture between NASA and DLR targeting the creation of a long-term record of variations in Earth's gravity field. From 2002 to 2017, the GRACE mission enabled a more than 15-year record of Earth gravity solutions vital to the Earth Sciences (*Tapley et al.*, 2004a). From 2011 through the end of the mission, these estimates grew increasingly more challenging due to continued degradation of onboard systems, primarily driven by decreased battery life and associated issues such as the elimination of thermal control and loss of the accelerometer on-board one of the two satellites (*Tapley et al.*, 2016; *Tapley*,

2018). By mission end in October 2017, further battery degradation and diminished fuel reserves ultimately led to mission end of life, with June 2017 serving as the final month of science data (*Cole and Buis*, 2017; *Tapley*, 2018). All together, the GRACE mission provided 163 months of time-variable gravity estimates, as well as atmospheric occultation estimates for weather models and atmospheric density estimates for neutral density models (*Tapley*, 2018). GRACE Follow-On (GRACE-FO), which launched in May 2018, is set to continue the GRACE record into the future (*Flechtner et al.*, 2016). This record has become a primary medium for studying glacial ice mass loss in Greenland, Antarctica, and other regions and also for tracking extended drought, flooding, and other large-scale hydrological signals (*Luthcke et al.*, 2006; *Velicogna and Wahr*, 2006; *Rodell et al.*, 2006, 2018).

The GRACE and GRACE-FO missions each consist of a pair of identical satellites in low-earth orbit, nominally 450-500 km in altitude (*Tapley et al.*, 2004a). A nearly circular, polar orbit (89.5° inclination) provides global coverage of Earth's gravity field (*Tapley et al.*, 2004a). Over the course of the GRACE mission, the altitude of these satellites slowly decreased due to atmospheric drag effects, ultimately falling below 400 km during the mission's extended science phase before eventually de-orbiting after October 2017 end of mission. GRACE-FO's initial orbit altitude of approximately 490 km allows for measurements to be of like kind. GRACE's polar orbit provides full global coverage, while a circular low altitude orbit provides the most detailed picture of the observed gravity field, as higher altitudes result in smaller gravitational perturbation effects. An even lower orbit would allow GRACE to capture an even more detailed picture of the gravity field, but increased atmospheric drag would impose too costly a requirement for continuous thrusting for maintaining altitude unless drag compensation becomes significantly more affordable.

The twin GRACE satellites, circling Earth in identical orbits and separated by approximately 220 km along that orbit, are linked by a K-band microwave ranging signal and directly measure the changes in the distance and velocities between the two satellites to accuracies smaller than 10 micrometers (*Wahr et al.*, 1998; *Tapley et al.*, 2004a). As a point of reference, this is equal to measuring the distance between an object in Seattle, WA and an object in Portland, OR to better

than the thickness of a human hair. Onboard GPS instruments are used to determine the precise positioning of both satellites, and terrestrial-based laser ranging systems are used to verify these position estimates. Star tracker cameras on two axes provide spacecraft attitude information in conjunction with orbital data. By using onboard accelerometers to account for non-conservative forces such as atmospheric drag and solar radiation pressure, these measurements are combined to estimate the monthly averaged global gravity field perturbing the orbits of the satellite pair from all residual signals present in the microwave range and range-rate measurements. The gravity field and gravitational accelerations are covered in more depth in Chapter 2.

1.4 GRACE Products

For much of the GRACE mission, time-variable gravity estimates have been strictly in the form of global sets of spherical harmonics, developed and released in parallel by the University of Texas at Austin's Center for Space Research (CSR), NASA's Jet Propulsion Laboratory (JPL), and the German Research Center for Geosciences (GFZ) (*Tapley et al.*, 2004a). These techniques have proven useful because they allow for the computation of a global solution averaged over a certain time period (*Wahr et al.*, 1998), and have been used to study changes in global hydrologic and cryospheric water storage. Regions with large ice mass loss, droughts, and strong annual and inter-annual variations in water storage have been studied on timescales of years dating across the entire GRACE mission (*Velicogna and Wahr*, 2006; *Rodell et al.*, 2006).

GRACE spherical harmonic solutions are developed as unconstrained products, and named as "Level-2" data products. Such spherical harmonic estimates represent the gravity field as a set of differential Stokes coefficients to a set degree and order as a mathematical expansion of the gravity field, covered in Chapter 2. These products range from 60×60 to 96×96 degree and order realizations of the gravity field, with resolutions on the order of 300-400 km. These solutions follow a standardized protocol, with each official center implementing a unique estimation system

for determining these unconstrained fields (*Bettadpur*, 2018).

Due to the spatial and temporal coverage limits of the GRACE mission and processing requirements of the GRACE release products, Level-2 spherical harmonic products have most often been distributed as monthly fields, and often are delayed in release by one to two months. Basin and regional studies of water storage have largely relied on the application of signal localization techniques to the global spherical sets, such as the averaging kernel method described in *Swenson and Wahr* (2002). These techniques must account for signal leakage effects across basin boundaries due to the limited resolution of GRACE observations and the unconstrained nature of Level-2 products, and further must account for striping and ringing effects caused by correlated errors and truncation of the Stokes coefficients at a maximum degree and order (*Wahr et al.*, 1998; *Swenson and Wahr*, 2002, 2006). These techniques further constrain the ability of GRACE monthly estimates to accurately return regional mass estimates (*Luthcke et al.*, 2006).

So that non-experts in fields outside geodesy might easily be able to make use of GRACE time-variable gravity fields, a new type of product referred to as a "Level 3" or Tellus product (named after the JPL portal through which these products are available) was introduced. These products are gridded versions of the unregularized spherical harmonic solutions, with certain corrections applied for non-water signals such as land motion as well as attempts at containing leakage through post-processing (*Chambers*, 2012; *Swenson*, 2012; *Swenson and Wahr*, 2006). However, these products are only implementations of the various post-processing techniques used with GRACE spherical harmonics, and therefore are limited by the filtering choices applied to these products.

In recent years, work has been done using mass concentrations (mascons) to provide an alternative to the spherical harmonic modeling technique. These mascon solutions use various regularization techniques to better resolve localized gravity variations, solving for mass variations in a finite number of equal-area mascon cells distributed across the globe (*Luthcke et al.*, 2013; *Watkins et al.*, 2015; *Save et al.*, 2016). Because each individual mascon is unique from those surrounding it, mascons can be solved for individually, regionally, or as a global set, and these regional studies of long-term mass change become as simple as the summing of mascons within a

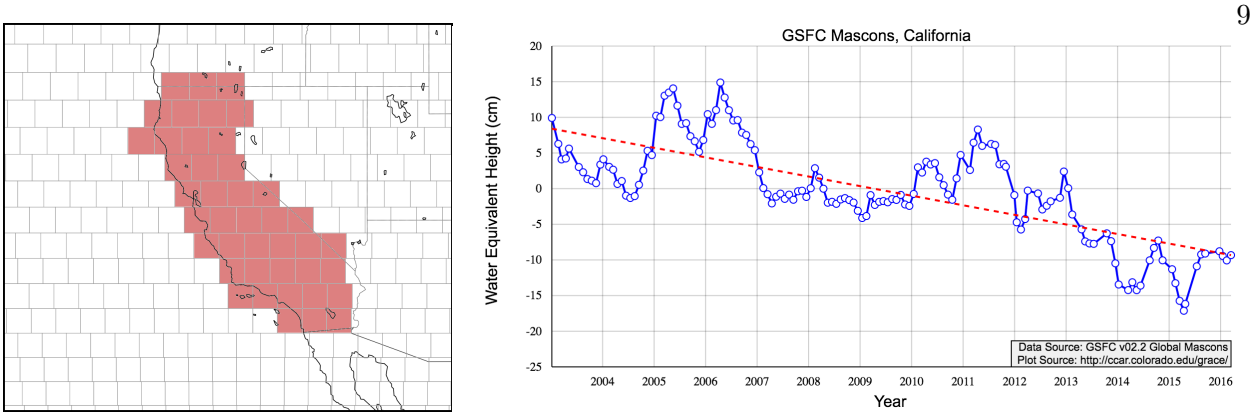

Figure 1.1: GRACE products have enabled the study of regional long-term mass fluctuations, such as the multi-year drought in California, shown here from the GSFC monthly mascon solution. Mascon solutions allow easy basin analysis by simply summing signals from each mascon over a given basin of appropriate size and shape. *Plot taken from the Mascon Visualization Tool:* `http://ccar.colorado.edu/grace/` (*Croteau and Nerem*, 2016).

region. Figure 1.1 shows an example of this, depicting the multi-year drought over the California basin recovered by the Goddard Space Flight Center's (GSFC) monthly GRACE Global Mascon solution. Spatial regularization techniques using correlations and constraints can be designed and built into the estimation process for mascons, enabling solutions to be computed that otherwise might be under-constrained (*Sabaka et al.*, 2010; *Luthcke et al.*, 2013). Alternative types of *a priori* information pertaining to the data and expected resulting gravity field can be used, such as model-driven covariance maps or information from recovered spherical harmonic fields to drive a solution to convergence (*Watkins et al.*, 2015; *Save et al.*, 2016).

Mascons offer an alternative solution method to spherical harmonics by developing global solutions of surface mass distribution using discrete, independent mass cells at or below the spatial resolution of GRACE. Mascon formulations have long been utilized in quantifying variations in surface mass distributions, dating back to unmanned satellites prior to Apollo to understand the lunar gravity field and aid in Apollo navigation (*Muller and Sjogren*, 1968). More recently, GRACE-derived regional and global mascon formulations have been shown to accurately recover expected

mass fluctuations, including water storage changes in the Amazon basin as well as ice mass loss in polar regions such as the Greenland Ice Sheet (*Rowlands et al.*, 2005; *Luthcke et al.*, 2006). These and similar works take advantage of a key characteristic of mascons: that individual mascons can be determined as distinct subsets of the larger global set. This dissertation uses a mascon formulation to resolve daily estimates for TWS, and this formulation is described in Chapter 2.

1.5 Scientific Contributions of GRACE

The 15+ year record from GRACE has led to new scientific insights in wide ranging areas of research. As an example metric illustrating the wide reach of GRACE data in the Earth Sciences, hundreds of studies analyzing GRACE data were presented at the 2017 AGU Fall Meeting in New Orleans, Louisiana in sessions covering Geodesy, Hydrology, Glaciology, and Ocean Sciences, and dozens more investigated future GRACE-like missions (*AGU*, 2017). GRACE data has provided new and otherwise impossible insights into these and other fields by providing a global, unbiased picture of time-variable gravity, and with it invaluable information on global water transport. This section serves to provide a sampling of the many varied contributions the GRACE mission has made to these fields.

1.5.1 Hydrology

Seasonal and secular TWS signals are a major component of GRACE time-variable gravity estimates. Monthly GRACE estimates have allowed for the recovery of seasonal water storage in river basins worldwide, beginning with some of the earliest scientific results from the GRACE mission. *Swenson and Wahr* (2002) presented a method for basin averages from GRACE spherical harmonic solutions using spatial averaging kernels. This and other techniques have been used to characterize terrestrial and groundwater storage changes in the Amazon, Mississippi, India, and many more basins (*Tapley*, 2004; *Rodell et al.*, 2006).

Monthly GRACE fields have contributed significantly in characterizing basin-wide drought conditions globally. *Thomas et al.* (2014) developed a technique for relating current TWS conditions with historical climatology and determining the magnitude and significance of drought conditions each month, and showed strong correlations between that index and other meteorological drought records. Likewise, anomalous increases in TWS have been detected, most notably during the 2011 La Niña that was said to be "so strong, the oceans fell," where excess terrestrial water storage over interior Australia was shown to have caused an extended drop in global mean sea level (GMSL) of 5 mm from 2010 through mid-2011 (*Boening et al.*, 2012). *Tourian et al.* (2018) demonstrated a method for using GRACE to quantify the total drainable water storage in humid climates such as the many sub-basins of the Amazon system.

As GRACE provides a global picture of the total water column, extensive efforts have been made in the fields of modeling and data assimilation to incorporate GRACE TWS estimates into assimilative models and forecasting tools. *Livneh and Lettenmaier* (2012) showed that GRACE data can be combined with meteorological and evapotranspiration data to estimate multiple components of the terrestrial water budget using land surface models, though the GRACE monthly temporal resolution and coarser spatial resolution (compared to the other datasets) contributed the largest uncertainties to the study and highlighted challenges with using multiple independent data sets in determining the water budget. *Zaitchik et al.* (2008) demonstrated improvements to groundwater modeling skill in the Catchment Land Surface Model (CLSM) and in correlations with river gauge flow measurements in the Mississippi River basin. *Houborg et al.* (2012) showed that the incorporation of GRACE data into a system based on the CLSM showed statistically significant improvements in the hydrological modeling skill of the system across large portions of the United States, suggesting GRACE could improve regional drought detection. *Kumar et al.* (2016) showed similar results using the North American Land Data Assimilation System (NLDAS). Data assimilation has also been used to downscale GRACE information and vertically partition GRACE TWS into various water storage components, combining GRACE observations with other data such as surface soil moisture (*Girotto et al.*, 2016). Later work discussed some of the benefits and

cautionary tales of these data assimilation efforts, pointing to assimilation efforts in India that did not properly account for groundwater pumping, which in turn led to realistic TWS recovery but erroneous evapotranspiration results (*Girotto et al.*, 2017).

To date, GRACE has been primarily used for studies of longer-wavelength signals such as annual cycles and long-term drought due to the monthly resolution of most GRACE products. However, for applications such as drought monitoring, water resource management, and data assimilation, monthly resolution poses problems associated with temporal aliasing and delays in information availability. This dissertation studies how a daily solution might be able to provide better temporal information at the cost of spatial resolution, which could then be used to better inform these applications in the future.

1.5.2 Glaciology

Along with hydrologic signals, changes in glacial ice mass are the largest water signals in the GRACE record. These signals have been the focus of extensive study, as efforts to quantify and map these mass losses are extremely important for understanding climate change implications. Ice melt experienced in Greenland, Antarctica, Alaska, and smaller mountain glaciers not only transforms the gravity field of the local area, but this melt leads directly to sea level rise as ocean mass increases with runoff. As an example of the catastrophic potential of glacial ice melt, estimates show that if the entire Antarctic and Greenland ice sheets were to melt, the total resulting rise in global mean sea level would be approximately 60 and 6 meters, respectively (*Church et al.*, 2013). Though such total collapse would not be likely to occur even over 1000 years, this is still an important point to consider as even small increases in local sea level would lead to severe consequences due to increased storm surge and coastal flooding, even without accounting for feedback effects of more energy content stored in the oceans (*Tebaldi et al.*, 2012).

Among numerous methods for estimating ice melt, GRACE can measure continental-scale mass loss by tracking changes in the gravitational attraction of glaciers, while other methods of estimating ice mass loss (for example, by measuring changes in glacial height with laser altimetry)

require knowledge of firm density and compaction, ice flow, and more. However, mass loss estimates from GRACE are contaminated by glacial isostatic adjustment (GIA), the crustal rebounding effect due to past deformation during the last ice age. Therefore, when computing mass change estimates in glacial regions affected by GIA, a GIA model such as *A et al.* (2013) is commonly applied to separate secular gravity signals due to crustal motion from those due to ice melt. Estimates from GRACE show ice melt ranging from 230-280 Gt/yr for the Greenland Ice Sheet and 80-180 Gt/yr for Antarctica, with these mass losses primarily originating in the West Antarctic Ice Sheet and coastal Greenland, and non-negligible accelerations have also begun to be detected (*Luthcke et al.*, 2013; *Velicogna et al.*, 2014). Similar estimates show that Greenland contributes 0.66 mm/yr to GMSL rise, while Antarctica adds 0.19 mm/year, and melt in mountain glaciers in the Gulf of Alaska, Patagonia, and Himalayas account for 0.51 mm/yr (*Nerem et al.*, 2018). Interdisciplinary efforts such as the ice sheet mass balance inter-comparison exercise (IMBIE) have used GRACE ice mass loss estimates in conjunction with other data and surface mass balance models to further characterize glacial ice mass changes over the past few decades (*Shepherd et al.*, 2018). As the GRACE-FO mission moves forward, the further lengthening of this record will continue to be a major contribution from the GRACE missions, and efforts to detect both trends and accelerations in ice melt will become more precise.

While glacial mass balance is not a key motivation for this dissertation, the work presented is very relevant to many such applications. Greenland, Antarctica, and other high-latitude glacial regions are located in the most observable portions of the gravity field at daily timescales. Due to the GRACE polar orbit, orbit groundtracks are focused at the poles, and provide both the best overlapping observation geometry and most dense spatial coverage. Therefore, the daily solution resulting from this work is directly applicable to topics such as surface mass balance modeling with GRACE. Additionally, atmospheric mis-modeling over Antarctica due to poor meteorological coverage can result in large errors for mass balance over that continent from GRACE, and daily solutions may provide new insights to better inform these atmospheric models (*Hardy et al.*, 2017).

1.5.3 Oceanography

Fluctuations in total ocean mass content and ocean mass distribution are significant gravitational features and observable to GRACE, though these signals are much smaller than those for TWS and glaciology. Ocean mass is in natural harmony with land hydrology, as seasonal fluctuations in TWS are in constant exchange with the oceans. Wet periods where more rain falls over land than other times of year lead to decreases in ocean mass, while evaporation and runoff see that water eventually make its way in large part back into the oceans and subsequent periods with less land precipitation lead to increases in ocean mass. In addition, over the GRACE time period the oceans have seen a notable upward trend in mass primarily due to glacial ice melt discussed in Section 1.5.2.

Secular increases in GMSL due to glacial ice melt are perhaps one of the most sought after measurements from GRACE in oceans. Increases in GMSL are the result of two causes: steric (or temperature-driven) sea level rise and eustatic (or mass-driven) sea level rise. Steric sea level rise is due to thermal expansion of ocean water due to warming of the water. These effects do not cause any change in ocean mass, and are therefore not observable by GRACE, though *in situ* measurements from globally distributed floats allow this component of sea level rise to be estimated. On the other hand, eustatic sea level rise is directly measurable with GRACE, as increases in ocean mass directly lead to changes in Earth's gravity field. Taken together, steric and eustatic sea level rise should account for the total sea level rise as observed by satellite altimetry missions such as OSTM/Jason. Annual amplitudes of GMSL variations due to mass fluctuations were shown to be 1 cm, with regional patterns as high as 4 cm locally (*Johnson and Chambers*, 2013). *Chambers et al.* (2017) showed closure of the so-called "sea level budget" for long period trends by examining these signals, though showed disagreements at inter-annual timescales. In addition to GMSL, efforts such as *Chambers and Bonin* (2012) have investigated regional variations in ocean mass content from GRACE so as to better understand ocean mass effects on Earth's time-variable gravity field. GRACE also has been used to improve understanding of ocean currents and regional variation

through ocean bottom pressure (OBP) measurements (*Chambers and Bonin*, 2012; *Johnson and Chambers*, 2013). *Landerer et al.* (2015) showed that Lower North Atlantic Deep Water can be observed by GRACE alone, allowing recovery of interannual OBP anomalies. GRACE has been used in quantifying the extent to which sea level rise is accelerating due to ocean mass change (*Nerem et al.*, 2018).

The daily GRACE solutions developed in this dissertation do not focus on oceans and thus will not directly contribute to oceanography with GRACE. However, the developed methods can be extended to potentially improve sub-monthly tidal models. Such an extension will require efforts to best regularize an ocean solution, as done for TWS in this dissertation in Chapter 3.

1.5.4 Solid Earth

Though a primary focus of this dissertation, changes in water storage globally are not the only time-variable gravity signals observed by GRACE. Two solid earth signal types are of particular note, as they comprise large portions of the recovered monthly estimates and could cause confusion or invalid conclusions in analyses of water storage signals if not properly taken into account. These are glacial isostatic adjustment (mentioned briefly in Section 1.5.2) and large earthquakes.

Glacial Isostatic Adjustment, or GIA (sometimes historically referred to as Post-Glacial Rebound), is the result of Earth's viscoelastic response to large changes in surface mass loading as a result of the Pleistocene ice age, lasting from approximately 3 million to 11 thousand years ago (*Caron et al.*, 2018). This period saw large-scale increases in grounded glaciation over significant portions of Earth's more northern latitudes. In North America, kilometer thick glaciers extended through modern day Canada into portions of the northern United States, causing a downward deformation of Earth's crust in these and surrounding areas, and in turn forcing Earth's viscoelastic mantle outward and away from the glaciated areas. Similar glaciers extended through parts of Europe, Asia, and Antarctica. Since the period when these large ice masses melted, the compressed Earth has been slowly rebounding to an uncompressed state. As this rebound occurs, mantle material flows back into place, leading to positive mass changes where glaciers once compressed

the surface and negative mass changes outside these areas where the mantle material is flowing from. GIA occurs on timescales of tens of thousands of years, and appears in the GRACE history as a linear trend, with the largest signals located over parts of North America, Scandinavia, and Antarctica. GRACE makes no distinction between these mass trends and trends in TWS or ice melt, and therefore GIA models must be used to remove these non-water signals from the GRACE record in order to assess trends in surface water changes. Efforts such as those by *A et al.* (2013) and *Caron et al.* (2018) use statistical techniques in conjunction with models of Earth composition and mantle viscosity and *in situ* observations from GPS and relative sea level measurements in determining models of GIA. These various models can differ significantly, resulting in wide ranges in corrected ice mass loss estimates for less constrained regions such as portions of Antarctica.

During the GRACE mission, a number of very large earthquakes caused permanent and measurable changes in Earth's gravity field. Perhaps the two most notable events were the December 2004 Sumatra-Andaman quake (magnitude 9.4) and 2011 Tohoku quake (magnitude 9.0), whose impacts on Earth's gravity field were characterized by *Han et al.* (2006, 2008) and *Zhang et al.* (2016), respectively. Both earthquakes resulted in co-seismic shifts in the gravity field marked by a bi-modal distribution of mass increase on one side of the earthquake and mass decrease on the other side followed by post-seismic exponential decay over the following months.

The daily GRACE solutions developed here do not specifically target solid earth changes to the gravity field as a signal of interest. Many solid earth signals such as GIA are on long timescales and monthly solutions with better spatial resolution already provide the information potentially relevant to these signals. Earthquakes are an interesting case, as they occur relatively quickly and daily fields might best capture the timing of those changes. However, if such a field is recovered after the earthquake, it does not significantly add anything to capture this at low spatial resolutions with a daily solution since the earthquake's time will already be known. On the other hand, a recent study by *Panet et al.* (2018) on the Tohoku 2011 earthquake suggests that there might be pre-seismic loading signals visible in the GRACE record that could be a precursor to the earthquake. In this case, if a reliable prediction mechanism were to be developed, daily solutions

might be able to provide advanced warning of dangerous pre-seismic surface loading sometime in the future. Until this effect is better understood, however, daily solution efforts are best directed elsewhere.

1.5.5 Other Notable Contributions

In addition to the already presented fields, GRACE data has been used for a variety of other purposes as well. While there are too many examples to list, a sampling is presented here to demonstrate the wide variety of research benefiting from GRACE data. *Wahr et al.* (2015) discussed how trends in Release 5 GRACE spherical harmonic solutions include degree-2, order-1 (see Chapter 2) non-mass secular signals resulting from pole tide effects due to glacial ice melt, which contaminate mass change signals of interest for scientists, and this result ultimately fixed a mis-modeling error in developing surface mass change products. Using GRACE's two onboard GPS instruments, radio occultation measurements have allowed improvements in meteorological models (*Beyerle et al.*, 2005). The long record of GRACE observations has also contributed to improvements in our understanding of the mean static gravity field and geoid (developed in the Chapter 2) both alone and in combination with other satellite gravity measurements such as from GOCE (*Pail et al.*, 2010).

1.6 Problem of Interest: Improving the Temporal Information from GRACE

The GRACE mission has provided insights into a wide variety of Earth processes, in a sense allowing scientists to "weigh" the continents and oceans in ways never before possible. Unfortunately, a tradeoff between spatial and temporal resolution must be made due to the choice of a polar orbit. The monthly resolution of GRACE's traditional release products causes issues with fully utilizing GRACE data to tune hydrological models and forecasting. Additionally, a one- to two-month delay in the release of these products limits the usefulness of these products for near

real-time applications. As a result, efforts to use this data in assimilative hydrological models have thus far been limited to using GRACE as a low temporal resolution, objective constraint on hydrologic models (*Famiglietti and Rodell*, 2013). To make better use of GRACE information for such purposes, better temporal and spatial information is needed.

In order to increase the temporal coverage of GRACE data products, various groups have developed sub-monthly datasets on 10-day and weekly intervals. At least one group has developed daily Kalman smoothed spherical harmonic solutions utilizing spatial and temporal constraints in the solution process to best characterize variations in water storage (*Kurtenbach et al.*, 2012; *Mayer-Gürr et al.*, 2016). With all of these solutions, however, limitations are imposed by the daily coverage of the GRACE orbit, which does not observe the entire Earth on any given day. In fact, in a single day, large portions of Earth are more than three times as far away from the GRACE orbit as regions that GRACE flies directly over, meaning that GRACE only provides partial coverage on daily timescales, as shown in Figure 1.2. As these solutions are derived in spherical harmonic space - inherently requiring a global estimate of the gravity field - difficulties arise in validating the accuracy of portions of each estimate that receive little or no coverage during the timespan of each 10-day, weekly, or daily estimate. To attempt to overcome these challenges, *Kurtenbach et al.* (2012) drives the Kalman filter estimation process with geophysical models tuned to propagate forward each day's estimate. This solution is called the ITSG-Grace2016 Daily solution, and is co-estimated as spherical harmonics to degree and order 40 with a higher resolution monthly estimate. In order to parameterize the Kalman smoother, assumptions are made about signal continuities between days, resulting in a daily-updated solution but not individual daily information.

To date, two other attempts - both at CSR - have been made at the creation of a daily mascon product. In both cases, the methodologies have differed substantially from that proposed by this project. *Sakumura et al.* (2016) used a 21-day sliding window to create a mascon solution with daily resolution using regularization methods described in *Save et al.* (2016). This solution is notable for improving the temporal resolution of GRACE mascon products and for developing a daily product that is entire driven by GRACE observations, but the designed 21-day sliding window

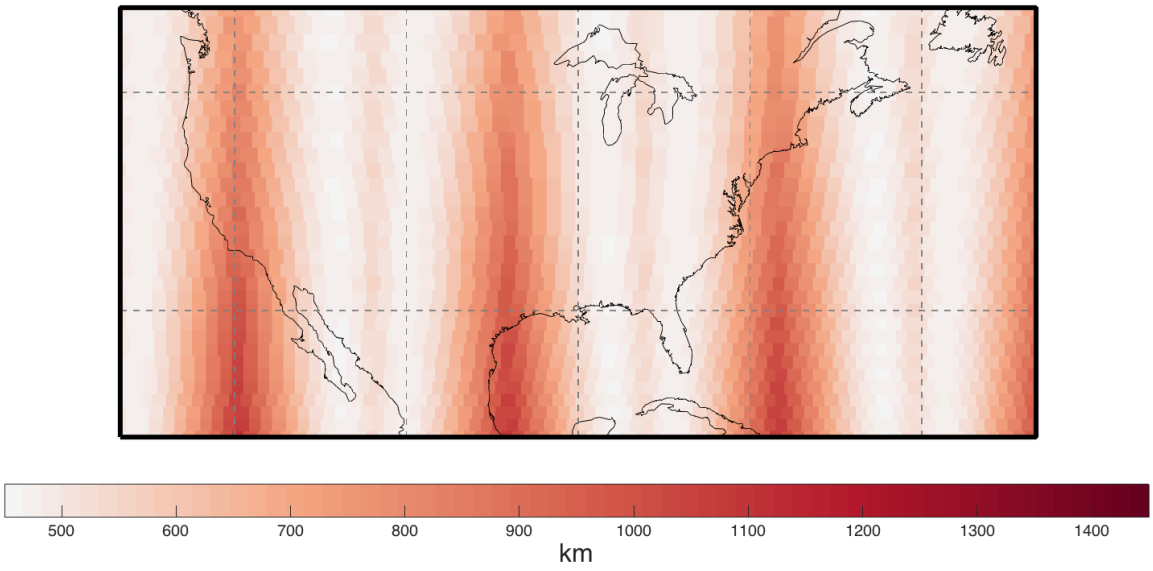

Figure 1.2: Minimum distance of mascons from GRACE orbit for a sample day. In a given day, the GRACE mission offers only partial coverage of the Earth, with some mascons (dark red) more than 3 times as far from the day's track as mascons that are flown directly above (white).

means that daily estimates are not independent, and the resolution of the solution is thus not truly daily. Ongoing work at CSR on a "swath" formulation, which updates only those mascons closest to the GRACE groundtrack each day from strictly one day's worth of data, also attempts to resolve daily variations in mascon space. This swath constrains mascons by distance to the orbital track, with those mascons farthest from the GRACE orbit on a given day constrained such that they are not allowed to vary for that day. However, the choice of a swath design adds complications to the design and validation portions of a daily estimate, and necessitates certain assumptions be made. Chapter 3 discusses this particular design option in more detail, and why a decision was made to pursue a novel third path to daily solutions in this dissertation: combining low-spatial and high-temporal resolution daily estimates for a global set of land mascons with high-spatial resolution monthly estimates to create a mixed or hierarchical GRACE TWS estimate on daily timescales.

The work presented in this dissertation uses the unique characteristics of mascons to develop

a global solution that is updated daily using the new data for each day. This solution provides a GRACE daily-updated TWS estimate at the highest achievable temporal resolution. This solution is computed using a least squares approach derived from the technique used to calculate the current GSFC monthly mascon solution. In developing this solution, this research will address the following questions:

(1) To what extent can daily GRACE gravity field estimates better resolve sub-monthly local and regional terrestrial water storage?

(2) What limitations exist on the extent to which GRACE can recover sub-monthly terrestrial water storage, and how might the design of a daily solution be optimized to minimize these limitations?

Resulting from this research is a daily GRACE solution that can describe large spatial scale TWS changes daily, with applications related to basin water storage. This solution delivers a new objective data set for use in drought and flood monitors and hydrologic forecasting.

1.7 Overview of dissertation

This document details the development of a daily GRACE mascon solution, covering necessary background theory as well as solution design, signal content, and resolution.

Chapter 2 discusses prerequisite theory underlying our modern understanding of the gravity field, examines least squares estimation as it relates to GRACE, and presents the gravity field as a global set of mascon cells. In this chapter, the technical knowledge and techniques required to complete this work is presented, outlining the representation of the gravity field as a set of spherical harmonics and the realization of this field in mascon space. Earth's gravitational potential is derived from Newton's law of universal gravitation and is expressed in a spherical frame using a global set of Stokes coefficients. Resulting gravitational accelerations on a satellite experiencing this potential are provided as part of an explanation of how GRACE observes the gravity field, and geoid and

surface mass representations of the gravity field are presented. Finally, weighted least squares with *a priori* information is discussed.

Chapter 3 builds on Chapter 2 by presenting the developed daily mascon solution. Mascon solution regularization is a key focus of this chapter, as this regularization both enables improved realizations of the gravity field with respect to leakage and correlated errors and provides a mechanism through which signal resolution can be estimated and compared with models. Proper design of the solution regularization strategy includes the majority of decision-making and effort during development, and solution analyses are conducted in part to prove a good regularization strategy has been developed.

Chapter 4 presents a simulation study that was conducted to test the designed estimation system and quantify the expected spatial information content of the daily solutions. With real GRACE data, the "truth" is unknown. This simulation provides an opportunity to quantify the recovery skill of the developed solution using a known signal. Results of the simulation are then used to validate further analysis of the real daily solution.

Chapter 5 builds on insights from the simulation study to further quantify the spatial information recovered by the solution. The spatial information contained in the solution is quantified globally, and includes the quantification of leakage effects into and out of basins due to the designed regularization discussed in Chapter 3. A rigorous analysis of recovered TWS is presented in the form of a multi-basin analysis as compared to TWS model output from the North American Land Data Assimilation System (NLDAS). As a point of comparison between mid and high latitudes, polar basins are then briefly considered.

Chapter 6 summarizes this work and presents conclusions of the study. Future considerations are suggested as extensions of this research.

Chapter 2

Theory

This chapter discusses background knowledge and theory necessary for the development of the daily GRACE solutions presented in this dissertation. Modeling of Earth's gravitational field is discussed, beginning with Newton's universal law of gravitation and covering the representation of the gravity field as a set of spherical harmonic coefficients, ultimately covering the realization of the gravity field as a global set of mascons. As part of this discussion, the geoid (an equipotential surface approximating sea level) is covered, as is computation of surface mass variability as they relate to changes in the gravitational field. Least squares estimation is then briefly discussed.

2.1 Earth's gravitational potential

Like all celestial bodies, Earth is a heterogeneous mass of varying shape and composition, and thus varying gravitational potential. General kinematics often represents acceleration due to Earth gravity as a single value (e.g., 9.81 meters per second per second), but in fact this is a simplification of a more dynamic topic. Here, Earth's gravity field is derived following *Kaula* (2000) and *Vallado* (2001). For a fully rigorous derivation, the reader is encouraged to consult *Kaula* (2000).

Newton's universal law of gravitation states that the force of attraction between two bodies of mass is directly proportional to the amount of mass of those two bodies and inversely proportional

to the square of the distance between those two bodies, following:

$$\mathbf{F} = G\frac{mM}{r^2}\hat{\mathbf{r}}, \tag{2.1}$$

where m and M are the masses of the two bodies, $\mathbf{r}$ is the distance vector between the two bodies and r is the scalar distance between these bodies ($r = |\mathbf{r}| = \sqrt{x^2 + y^2 + z^2}$), $\hat{\mathbf{r}}$ is the normalized unit vector of $\mathbf{r}$, and G is a universal constant. In the S.I. system, with meters as the standard unit of distance, kilograms as the standard unit of mass, and seconds as the standard unit of time, G is approximately equal to 6.67×10^{-11} $\mathrm{m}^3/\mathrm{kg}/\mathrm{s}^2$. Applying Newton's second law to an Earth-fixed Cartesian frame and assuming constant mass m,

$$\mathbf{F} = m\mathbf{a}, \tag{2.2}$$

the equation for vector acceleration of m in the Earth-fixed frame due to the gravitational attraction from Earth's mass M is then

$$\mathbf{a} = \frac{GM}{r^2}\hat{\mathbf{r}}. \tag{2.3}$$

This acceleration $\mathbf{a}$ can be defined as the gradient of gravitation potential, V, as

$$\mathbf{a} = \nabla V, \tag{2.4}$$

where V for a single particle of mass m_i can be expressed as

$$V = \frac{Gm_i}{r} = Gm_i\left(x^2 + y^2 + z^2\right)^{-\frac{1}{2}}. \tag{2.5}$$

For a large body of mass such as Earth, the body can be considered as a continuous body of many infinitesimal particles of varying densities ρ at unique cartesian (or rectangular) positions $r(x, y, z)$, and the total potential of the body is the integral of these particles in space:

$$V = G\sum_i \frac{m_i}{r_i} = G\int_x\int_y\int_z \frac{\rho(x,y,z)}{r(x,y,z)}\, dz\, dy\, dx \tag{2.6}$$

.

From the total potential, the acceleration is then

$$\mathbf{a} = \begin{bmatrix} \frac{\partial V}{\partial x} \\ \frac{\partial V}{\partial y} \\ \frac{\partial V}{\partial z} \end{bmatrix} = \begin{bmatrix} -GM\left(x^2+y^2+z^2\right)^{-\frac{3}{2}} x \\ -GM\left(x^2+y^2+z^2\right)^{-\frac{3}{2}} y \\ -GM\left(x^2+y^2+z^2\right)^{-\frac{3}{2}} z \end{bmatrix} = \begin{bmatrix} -GM\frac{x}{r^3} \\ -GM\frac{y}{r^3} \\ -GM\frac{z}{r^3} \end{bmatrix} \tag{2.7}$$

Taking the second derivative of each term,

$$\begin{bmatrix} \frac{\partial^2 V}{\partial x^2} \\ \frac{\partial^2 V}{\partial y^2} \\ \frac{\partial^2 V}{\partial z^2} \end{bmatrix} = \begin{bmatrix} -GM\left(\frac{1}{r^3} - \frac{3x}{2r^5}2x\right) \\ -GM\left(\frac{1}{r^3} - \frac{3y}{2r^5}2y\right) \\ -GM\left(\frac{1}{r^3} - \frac{3z}{2r^5}2z\right) \end{bmatrix} = \begin{bmatrix} GM\left(-\frac{1}{r^3} + \frac{3x^2}{r^5}\right) \\ GM\left(-\frac{1}{r^3} + \frac{3y^2}{r^5}\right) \\ GM\left(-\frac{1}{r^3} + \frac{3z^2}{r^5}\right) \end{bmatrix} \tag{2.8}$$

In Cartesian space, Laplace's Equation gives

$$\nabla^2 f = \frac{\partial^2 f}{\partial x^2} + \frac{\partial^2 f}{\partial y^2} + \frac{\partial^2 f}{\partial z^2} = 0. \tag{2.9}$$

Substituting from Equation 2.8 for $\nabla^2 V$,

$$\nabla^2 V = GM\left(-\frac{1}{r^3} + \frac{3x^2}{r^5}\right) + GM\left(-\frac{1}{r^3} + \frac{3y^2}{r^5}\right) + GM\left(-\frac{1}{r^3} + \frac{3z^2}{r^5}\right) = 0, \tag{2.10}$$

and reducing,

$$\nabla^2 V = GM\left(-\frac{3}{r^3} + \frac{3\left(x^2+y^2+z^2\right)}{r^5}\right) = 0 \tag{2.11}$$

For many Earth applications, including geodesy, it is common to transform from a cartesian frame into a spherical coordinate frame, defining our coordinates in terms of latitude ϕ, longitude λ, and radius r, where

$$\begin{aligned} x &= r\cos\phi\cos\lambda, \\ y &= r\cos\phi\sin\lambda, \\ z &= r\sin\phi. \end{aligned} \tag{2.12}$$

Differentiating and solving the system of equations for dx, dy, and dz, it is straightforward to determine

$$\begin{aligned} dr &= \cos\phi\cos\lambda\ dx + \cos\phi\sin\lambda\ dy + \sin\phi\ dz, \\ d\phi &= -r^{-1}\sin\phi\cos\lambda\ dx - r^{-1}\sin\phi\sin\lambda\ dy + r^{-1}\cos\phi\ dz, \\ d\lambda &= -r^{-1}\cos^{-1}\phi\sin\lambda\ dx + r^{-1}\cos^{-1}\phi\cos\lambda\ dy. \end{aligned} \tag{2.13}$$

The partial derivative of the potential with respect to x, y, and z can then be determined by

$$\begin{aligned}
\frac{\partial V}{\partial x} &= \frac{\partial V}{\partial r}\frac{\partial r}{\partial x} + \frac{\partial V}{\partial \phi}\frac{\partial \phi}{\partial x} + \frac{\partial V}{\partial \lambda}\frac{\partial \lambda}{\partial x} \\
&= \frac{\partial V}{\partial r}\cos\phi\cos\lambda - \frac{\partial V}{\partial \phi}r^{-1}\sin\phi\cos\lambda - \frac{\partial V}{\partial \lambda}r^{-1}\cos^{-1}\phi\sin\lambda, \\
\frac{\partial V}{\partial y} &= \frac{\partial V}{\partial r}\frac{\partial r}{\partial y} + \frac{\partial V}{\partial \phi}\frac{\partial \phi}{\partial y} + \frac{\partial V}{\partial \lambda}\frac{\partial \lambda}{\partial y} \\
&= \frac{\partial V}{\partial r}\cos\phi\sin\lambda - \frac{\partial V}{\partial \phi}r^{-1}\sin\phi\sin\lambda + \frac{\partial V}{\partial \lambda}r^{-1}\cos^{-1}\phi\cos\lambda, \\
\frac{\partial V}{\partial z} &= \frac{\partial V}{\partial r}\frac{\partial r}{\partial z} + \frac{\partial V}{\partial \phi}\frac{\partial \phi}{\partial z} + \frac{\partial V}{\partial \lambda}\frac{\partial \lambda}{\partial z} \\
&= \frac{\partial V}{\partial r}\sin\phi + \frac{\partial V}{\partial \phi}r^{-1}\cos\phi.
\end{aligned}$$

After computing the second partial derivative terms, Laplace's Equation is expressed in spherical coordinates as

$$r^2\nabla^2 V = \frac{\partial}{\partial r}\left(r^2\frac{\partial V}{\partial r}\right) + \cos^{-1}\phi\,\frac{\partial}{\partial \phi}\left(\cos\phi\frac{\partial V}{\partial \phi}\right) + \cos^{-2}\phi\,\frac{\partial^2 V}{\partial \lambda^2} = 0. \tag{2.14}$$

To solve Laplace's Equation, the potential can be expressedas

$$V = R(r)\Phi(\phi)\Lambda(\lambda), \tag{2.15}$$

a function where the total potential is the product of a function of r only, a function of ϕ only, and a function of λ only. Substituting this expression into 2.14 and reducing, the equation becomes

$$R^{-1}\frac{\partial}{\partial r}\left(r^2\frac{\partial R}{\partial r}\right) + \Phi^{-1}\cos^{-1}\phi\,\frac{\partial}{\partial \phi}\left(\cos\phi\frac{\partial \Phi}{\partial \phi}\right) + \Lambda^{-1}\cos^{-2}\phi\,\frac{\partial^2 \Lambda}{\partial \lambda^2} = 0. \tag{2.16}$$

As R, Φ, and Λ are separable functions with independent variables, the partial derivatives can then be realized as absolute derivatives, and Equation 2.16 as

$$R^{-1}\frac{d}{dr}\left(r^2\frac{dR}{dr}\right) + \Phi^{-1}\cos^{-1}\phi\,\frac{d}{d\phi}\left(\cos\phi\frac{d\Phi}{d\phi}\right) + \Lambda^{-1}\cos^{-2}\phi\,\frac{d^2\Lambda}{d\lambda^2} = 0. \tag{2.17}$$

The first part of the function is only a function of r, and therefore must be constant. Setting this term to $-l(l+1)$, where l is a positive integer, and differentiating gives

$$r^2\frac{d^2R}{dr^2} + 2r\frac{dR}{dr} - l(l+1)R = 0 \tag{2.18}$$

As each power x for $\frac{d^x}{dr^x}R$ is multiplied by a term r^x, Equation 2.18 suggests that R is of the form r^k, it is straightforward to substitute this into the equation as

$$r^2\frac{d^2(r^k)}{dr^2} + 2r\frac{d(r^k)}{dr} - l(l+1)r^k = 0 \tag{2.19}$$

and solving the equation,

$$\begin{aligned} 0 &= r^2k(k-1)r^{k-2} + 2rkr^{k-1} - l(l+1)r^k, \\ &= k(k-1)r^k + 2kr^k - l(l+1)r^k, \\ &= r^k\left(k(k-1) + 2k - l(l+1)\right), \\ &= k^2 + k - l(l+1), \end{aligned}$$

which has the solutions $k = l$ and $k = -(l+1)$, and R therefore is

$$R = Ar^l + Br^{-(l+1)} \tag{2.20}$$

where A and B are arbitrary constants of integration. A boundary condition for gravitational potential is that the potential must be 0 at infinity. Substituting, it can be determined that $A = 0$ from

$$\begin{aligned} 0 &= A(\infty)^l + B(\infty)^{-(l+1)}, \\ &= A(\infty)^l + B\frac{1}{(\infty)^{(l+1)}}, \\ &= A(\infty)^l, \end{aligned}$$

and

$$R = Br^{-(l+1)}. \tag{2.21}$$

Further substituting into Equation 2.17 and reducing, it is possible to obtain

$$l(l+1)\cos^2\phi + \frac{\cos\phi}{\Phi}\frac{d}{d\phi}\left(\cos\phi\frac{\partial\Phi}{\partial\phi}\right) + \frac{1}{\Lambda}\frac{d^2\Lambda}{d\lambda^2} = 0. \tag{2.22}$$

The final term from this equation is the only term in the equation that is dependent on longitude. For the equation to hold, this term must therefore be constant. Setting this constant to $-m^2$,

$$\frac{1}{\Lambda}\frac{d^2\Lambda}{d\lambda^2} = -m^2 \tag{2.23}$$

and integrating, a solution for Λ is determined as

$$\Lambda = C\cos m\lambda + S\sin m\lambda, \tag{2.24}$$

where C and S are arbitrary constants.

Then, substituting $-m^2$ into Equation 2.17, a form of the equation that is only a function of ϕ can be developed:

$$\begin{aligned} 0 &= l(l+1)\cos^2\phi + \frac{\cos\phi}{\Phi}\frac{d}{d\phi}\left(\cos\phi\frac{d\Phi}{d\phi}\right) - m^2 \\ &= l(l+1)\Phi + \frac{1}{\cos\phi}\frac{d}{d\phi}\left(\cos\phi\frac{d\Phi}{d\phi}\right) - m^2\frac{\Phi}{\cos^2\phi} \\ &= \frac{1}{\cos\phi}\frac{d}{d\phi}\left(\cos\phi\frac{d\Phi}{d\phi}\right) + \left[l(l+1) - \frac{m^2}{\cos^2\phi}\right]\Phi. \end{aligned}$$

From here, a series of substitutions and various developed assumptions presented in *Kaula* (2000) to solve for Φ can be used, ultimately determining

$$\Phi = P_{lm}(\sin\phi) = \cos^m\phi\sum_{t=0}^{k} T_{lmt}\sin^{l-m-2t}\phi \tag{2.25}$$

where k is the integer part of $(l-m)/2)$, $P_{lm}(\sin\phi)$ is called a Legendre associated function, and l and m are a set of subscripts.

Substituting Equations 2.21, 2.25, and 2.24 into Equation 2.15 and solving for the solution to the Laplace Equation, the total potential is then

$$V(r,\phi,\lambda) = \sum_{l=0}^{\infty}\sum_{m=0}^{l}\frac{1}{r^{l+1}}P_{lm}\left(\sin\phi\right)\left[C_{lm}\cos m\lambda + S_{lm}\sin m\lambda\right]. \tag{2.26}$$

In geodesy, subscripts l and m are referred to as the degrees and orders of the spherical expansion. As degree and order increase, the potential components of those degrees and orders are higher harmonic frequency signals and therefore increasingly finer-detail refinements to the potential. Figure 2.1 shows the unitless spatial patterns of C and S spherical harmonic coefficients through degree and order 4. Note that there are no S terms of order $m = 0$ shown, as $(S_{lm}\sin m\lambda)|_{m=0} = 0$ for all λ. Also, it is helpful to define a few terms relating to the spherical harmonic coefficients C_{lm} and S_{lm}: *zonal* coefficients are those coefficients with order $m = 0$ and describe mass distributions

along latitudinal sections, *sectoral* coefficients are those where the order m equals the degree l and describe mass distribution along longitudinal sections, and *tesseral* coefficients are all other coefficients and describe all other mass distributions in checkerboard-like patterns.

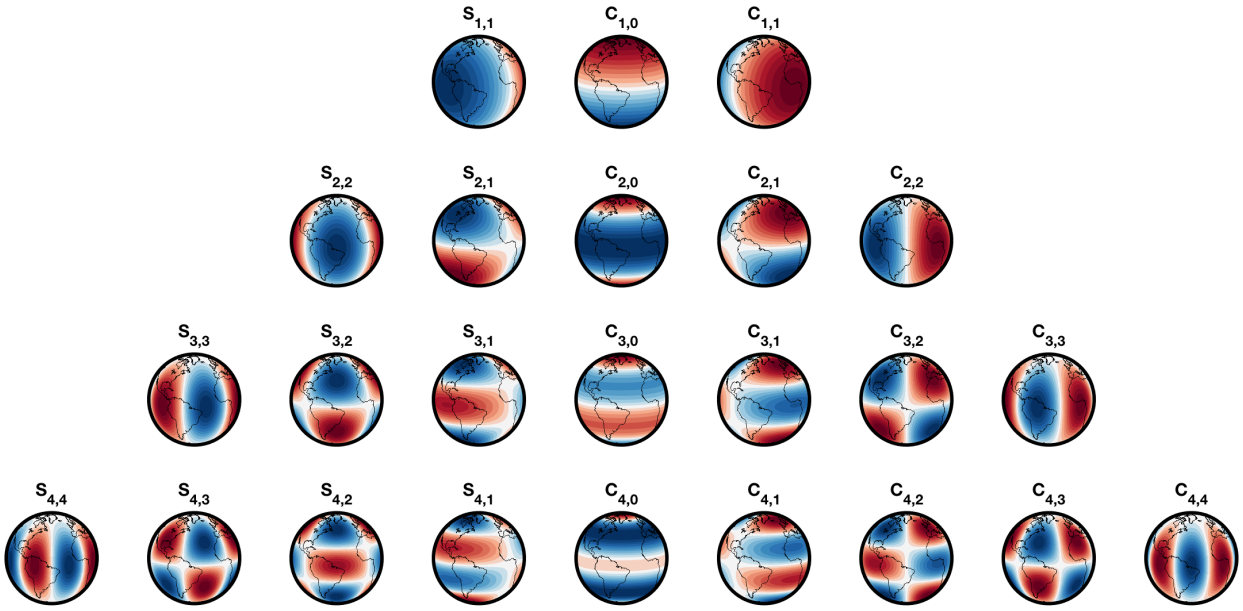

Figure 2.1: Spherical harmonic spatial patters through degree and order 4. *Zonal* harmonics are the center column, where $m = 0$. *Sectoral* coefficients are the first and last plots in each row where $l = m$. *Tesseral* coefficients are the remaining plots. Note that the total mass term, $C_{0,0}$, is not shown. Reds and blues of equal darkness on any single plot are equal in magnitude and opposite in sign, and magnitudes increase linearly with darkness.

For computational reasons, it is useful to normalize the spherical harmonic representation of the potential in Equation 2.26. This aids in both making the coefficients more readily comparable and in ensuring computational efficiency and stability on traditional double-precision float computer architectures. Following GRACE Level-2 processing standards from *Bettadpur* (2018), the potential at any time t is expressed in terms of a set of normalized Legendre functions $\tilde{P}_{lm}$ and spherical

harmonics $\overline{C}_{lm}$ and $\overline{S}_{lm}$ as

$$\boxed{V(r,\phi,\lambda,t) = \frac{\mu_\oplus}{r}\sum_{l=0}^{\infty}\left(\frac{a_\oplus}{r}\right)^l \sum_{m=0}^{l}\tilde{P}_{lm}\left(\sin\phi\right)\left[\overline{C}_{lm}(t)\cos m\lambda + \overline{S}_{lm}(t)\sin m\lambda\right],} \tag{2.27}$$

where Earth gravitational parameter $\mu_\oplus = GM_\oplus$, $M_\oplus$ is the mass of the Earth, and $a_\oplus$ is a mean equatorial radius. The Earth gravitational parameter is often used in geodesy rather than G and $M_\oplus$ separately because the product of these two terms is more well known than either term individually. The associated Legendre polynomials are normalized by

$$\tilde{P}_{lm}\sin(\phi) = N_{lm}P_{lm}(\sin\phi), \tag{2.28}$$

where

$$N_{lm} = \sqrt{\frac{(2-\delta_{0m})(2l+1)(l-m)!}{(l+m)!}} \tag{2.29}$$

and the Kronecker delta δ_{0m} is defined as 1 for $m = 0$ and as 0 otherwise. The normalized spherical harmonic terms are likewise normalized by

$$\begin{Bmatrix}\overline{C}_{lm}\\ \overline{S}_{lm}\end{Bmatrix} = \frac{1}{(2l+1)M_\oplus}\int_{r'}\int_{\phi'}\int_{\lambda'}\left(\frac{r'}{a_\oplus}\right)^l \tilde{P}_{lm}\left(\sin\phi'\right)\begin{Bmatrix}\cos m\lambda'\\ \sin m\lambda'\end{Bmatrix} dM \tag{2.30}$$

and integration is done globally for mass elements dM for the entire Earth system. Together, this normalized potential is consistent with other geodetic work, including other gravity field representations such as EGM96 (*Bettadpur*, 2018).

In spherical harmonics, the degree 0 term accounts for the total mass of the system, while the degree 1 terms account for the center of mass relative to the center of whatever reference frame is used to represent the system's potential. In Earth satellite geodesy, it is convention to define the origin of the reference frame as the center of mass of the Earth system, therefore eliminating degree 1 terms from Equation 2.27. In addition, while the potential can be expressed to an infinite degree and order, it is typical in geodesy and in GRACE to truncate that expansion at some maximum N_{max}. Taking this into account and recognizing that the degree 0 component of the summation is simply $\mu_\oplus/r$, the fully normalized potential equation can then be expressed as

$$V(r,\phi,\lambda,t) = \frac{\mu_\oplus}{r} + \frac{\mu_\oplus}{r}\sum_{l=2}^{N_{max}}\left(\frac{a_\oplus}{r}\right)^l \sum_{m=0}^{l}\tilde{P}_{lm}\left(\sin\phi\right)\left[\overline{C}_{lm}(t)\cos m\lambda + \overline{S}_{lm}(t)\sin m\lambda\right]. \tag{2.31}$$

2.2 Gravitational accelerations and GRACE

A satellite in orbit about Earth experiences accelerations due to the Earth's gravitational potential. These accelerations are what actually allow GRACE to work. The GRACE mission is composed of two satellites, that continuously measures the range and range-rates between the satellites using microwave interferometric ranging. These satellites fly in a leader-follower configuration, where one satellite first flies over gravitational anomalies before the second then follows it over the same anomaly. For a positive anomaly, the leading satellite is accelerated towards that anomaly as it approaches, increasing the range between the satellites and measuring a positive range-range. Then, as the satellite flies over and begins to move past the anomaly, the extra gravitational force acts in the opposite direction, decelerating the first satellite and decreasing the range between the satellites. Finally, as the second satellite approaches, flies over, and passes the anomaly, that satellite is first accelerated forward before being decelerated and ultimately maintaining the original configuration with respect the the lead satellite prior to approaching the gravitational anomaly. GRACE uses position measurements from GPS and laser ranging, attitude measurements from star tracker instruments, non-conservative force estimates from on-board accelerometers, and range and range-rate measurements between the satellites to then map these gravitational anomalies and form a complete picture of the gravity field. In this section, the classical formulation of acceleration due to gravitational potential is briefly summarized.[1]

Accelerations due to gravitational potential in cartesian coordinates, $\partial V/\partial \mathbf{r}$, can be computed from r, ϕ, and λ by the chain rule as in *Vallado* (2001):

$$\mathbf{a} = \frac{\partial V}{\partial r}\left(\frac{\partial r}{\partial \mathbf{r}}\right)^T + \frac{\partial V}{\partial \phi}\left(\frac{\partial \phi}{\partial \mathbf{r}}\right)^T + \frac{\partial V}{\partial \lambda}\left(\frac{\partial \lambda}{\partial \mathbf{r}}\right)^T, \tag{2.32}$$

[1] An interesting analogy illustrating how gravity anomalies affect GRACE can be made to cycling. If two bicyclists are traveling at the same speed, one in front of the other, and approach a valley, the first cyclist will begin to accelerate downhill away from the second. Reaching the bottom, that cyclist will begin to head uphill and decelerate. Meanwhile, the second cyclist has started down the hill, and closes the gap between the cyclists. When that second cyclist reaches the bottom, she too will begin to decelerate as she climbs uphill. Eventually, both cyclists reach level ground, and are the same distance apart, once again traveling at the same speed. If the cyclists can adequately determine the rates at which these events occurred, they could then calculate things like the slope and depth of the valley.

where

$$\frac{\partial V}{\partial r} = \frac{-\mu_\oplus}{r^2} \sum_{l=2}^{\infty} \sum_{m=0}^{l} \left(\frac{r_\oplus}{r}\right)^l (l+1) P_{l,m}(\sin\phi)[C_{lm}\cos m\lambda + S_{lm}\sin m\lambda],$$

$$\frac{\partial V}{\partial \phi} = \frac{\mu_\oplus}{r} \sum_{l=2}^{\infty} \sum_{m=0}^{l} \left(\frac{r_\oplus}{r}\right)^l \left(P_{l,m+1}(\sin\phi)\Pi'_{l,m} - m\tan\phi P_{l,m}(\sin\phi)\right)[C_{lm}\cos m\lambda + S_{lm}\sin m\lambda],$$

$$\frac{\partial V}{\partial \lambda} = \frac{\mu_\oplus}{r} \sum_{l=2}^{\infty} \sum_{m=0}^{l} \left(\frac{r_\oplus}{r}\right)^l m P_{l,m}(\sin\phi)[S_{lm}\cos m\lambda - C_{lm}\sin m\lambda], \tag{2.33}$$

where

$$\Pi'_{lm} = \sqrt{\frac{(n+m+1)(n-m)(2-\delta_{0m})}{2}}.$$

Derivatives of the position vector are determined directly, as

$$\frac{\partial r}{\partial \mathbf{r}} = \frac{\mathbf{r}^T}{r},$$

$$\frac{\partial \phi}{\partial \mathbf{r}} = \frac{1}{\sqrt{r_I^2 + r_J^2}} \left(-\frac{\mathbf{r}^T r_K}{r^2} + \frac{\partial r_K}{\partial \mathbf{r}}\right),$$

$$\frac{\partial \lambda}{\partial \mathbf{r}} = \frac{1}{r_I^2 + r_J^2} \left(r_J \frac{\partial r_J}{\partial \mathbf{r}} - r_J \frac{\partial r_I}{\partial \mathbf{r}}\right).$$

The term for $\partial\phi/\partial\mathbf{r}$ has a singularity at the poles. A scale factor $\Pi'_{l,m+1}/\Pi_{l,m}$ is added to the $P_{l,m+1}(\sin\phi)$ term in the $\partial V/\partial\phi$ partial derivative, to cancel out the spherical harmonic normalization factors (*Jones*, 2010).

Finally, solving for the acceleration terms gives

$$a_I = \left(\frac{1}{r}\frac{\partial V}{\partial r} - \frac{r_K}{r^2\sqrt{r_I^2 + r_J^2}}\frac{\partial V}{\partial \phi}\right) r_I - \left(\frac{1}{r_I^2 + r_J^2}\frac{\partial V}{\partial \lambda}\right) r_J$$

$$a_J = \left(\frac{1}{r}\frac{\partial V}{\partial r} - \frac{r_K}{r^2\sqrt{r_I^2 + r_J^2}}\frac{\partial V}{\partial \phi}\right) r_J + \left(\frac{1}{r_I^2 + r_J^2}\frac{\partial V}{\partial \lambda}\right) r_I$$

$$a_K = \frac{1}{r}\frac{\partial V}{\partial r} r_K + \frac{\sqrt{r_I^2 + r_J^2}}{r^2}\frac{\partial V}{\partial \phi}$$

2.3 Earth's shape and the geoid

While Earth is often discussed as a spherical planet, this is actually not a good approximation of the Earth. Even when not considering many of the small variations in the Earth surface or in Earth gravity, Earth's mean equatorial radius (6378.137 km) is more than 20 km larger than its polar radius (6356.751 km). Due to Earth's rotation and viscous composition, the permanent shape of the Earth is deformed by a so-called "equatorial bulge," best approximated not as a sphere but rather as an oblate spheroid, shown in Figure 2.2. An oblate spheroid is an ellipsoid defined by two larger, equal radii a along two axes ($\hat{x}$ and $\hat{y}$) and one smaller radius b along the third axis ($\hat{z}$) as

$$\frac{x^2}{a^2} + \frac{y^2}{a^2} + \frac{z^2}{b^2} = 1. \tag{2.34}$$

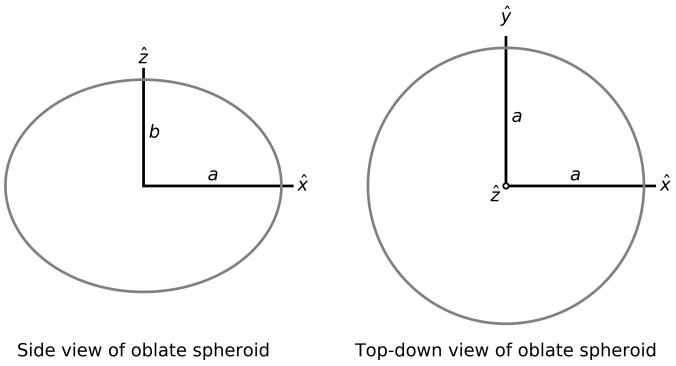

Figure 2.2: Side and top-down cross sections of an oblate spheroid, a special case of the ellipsoid. The $\hat{z}$ axis is the axis of rotation.

This shape can be defined by a mathematical term called "flattening" (f), which relates the Earth's mean equatorial radius a to its polar radius b by

$$f = \frac{a-b}{a}, \qquad f_\oplus = \frac{6378.137 - 6356.751}{6378.137} \approx \frac{1}{298.257}. \tag{2.35}$$

As such, flattening is a measure of the Earth's oblateness. There are many ellipsoids that could be used to approximate Earth's shape, depending on if it is desired to best match Earth's ocean surfaces, the surface over North America, and so on. The most widely used of these in satellite

geodesy is called the WGS 84 reference ellipsoid, determined by the World Geodetic Survey as the ellipsoid that best approximates the total mean sea surface. Another example ellipsoid is the TOPEX/Poseidon Ellipsoid, which differs on the order of one meter from WGS 84 and was designed to best approximate the oceans between $\pm 66°$ latitude.

In gravimetry, an important surface called the "geoid" is defined as the surface globally on which the vector direction of the force of gravity at any location on the surface is exactly perpendicular to the surface. This surface is defined from the total potential of gravity, W, that combined Earth's gravitational potential and its rotational effects by

$$W(r, \phi, \lambda) = V(r, \phi, \lambda) + \frac{1}{2}\omega^2 r^2 \cos^2 \phi. \tag{2.36}$$

If Earth's gravity field were perfectly spherical and earth had no rotation (as would be the case for a stationary point mass or a uniform sphere), a geoid for such an Earth would also be a sphere. The geoid is then the surface for which $W(r, \phi, \lambda)$ is constant. Figure 2.3 illustrates the geoid as it relates to the surrounding topography and the reference ellipsoid. There are actually an infinite number of geoid surfaces, expanding outward from the center of mass of the Earth, with each surface centered about some reference radius or ellipsoid. The geoid surface is most often defined as heights relative to an ellipsoid, such as WGS 84. In GRACE, the geoid surface is the equipotential surface best approximated by the mean sea surface.

An expression for the geoid height in spherical harmonics can be expressed by determining the disturbing potential T from the potential of gravity W in Equation 2.36 less the normal gravity U defined by the reference ellipsoid. Both W and U account for the same rotational effects and same degree 0 total mass, and can be defined by expressing the reference ellipsoid in terms of spherical harmonics:

$$\overline{C}_{lm,T}(t) = \overline{C}_{lm,W}(t) - \overline{C}_{lm,U}, \tag{2.37}$$

$$\overline{S}_{lm,T}(t) = \overline{S}_{lm,W}(t) - \overline{S}_{lm,U}. \tag{2.38}$$

It is often the case that the reference ellipsoid is defined by only the lowest degree zonal harmonics

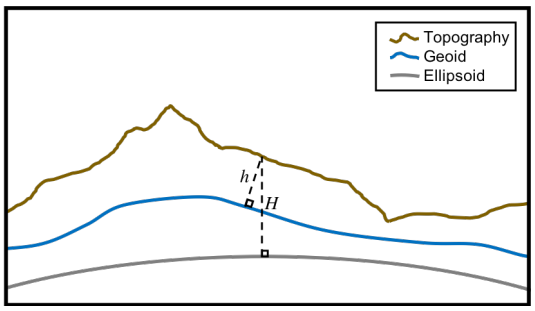

Figure 2.3: Illustration of the geoid as it relates to the reference ellipsoid and the surrounding topography. Elevation h is the height of the topography above or below the geoid surface and perpendicular to that surface. The force due to gravity is along this height. Height H is the height of the topography above the reference ellipsoid, called the orthometric height.

C_{20} and C_{40}. In any case, the disturbing potential can be expressed then as

$$T(r,\phi,\lambda,t) = \frac{\mu_\oplus}{r}\sum_{l=2}^{N_{max}}\left(\frac{a_\oplus}{r}\right)^l \sum_{m=0}^{l}\tilde{P}_{lm}\left(\sin\phi\right)\left[\overline{C}_{lm,T}(t)\cos m\lambda + \overline{S}_{lm,T}(t)\sin m\lambda\right]. \tag{2.39}$$

A relationship between the disturbing potential T and the geoid undulation N (or the height of the geoid above or below the reference ellipsoid) is given by Brun's equation as

$$N = \frac{T}{\gamma}, \tag{2.40}$$

where the normal gravity γ is defined by the mean gravitational acceleration as $\gamma = \frac{\mu_\oplus}{r^2}$ (*Jekeli*, 2009).

Evaluating for a spherical Earth ($r = a_\oplus$), the geoid undulation can then be expressed compactly (from here, dropping the T subscript in the spherical harmonics for neatness) as

$$N(\phi,\lambda,t) = a_\oplus\sum_{l=2}^{N_{max}}\sum_{m=0}^{l}\tilde{P}_{lm}\left(\sin\phi\right)\left[\overline{C}_{lm}(t)\cos m\lambda + \overline{S}_{lm}(t)\sin m\lambda\right]. \tag{2.41}$$

Figure 2.4 shows a map of geoid undulation heights from the EGM 96 model.

The time varying component of the geoid can then be defined as

$$\Delta N(\phi,\lambda,t) = a_\oplus\sum_{l=2}^{N_{max}}\sum_{m=0}^{l}\tilde{P}_{lm}\left(\sin\phi\right)\left[\Delta\overline{C}_{lm}(t)\cos m\lambda + \Delta\overline{S}_{lm}(t)\sin m\lambda\right], \tag{2.42}$$

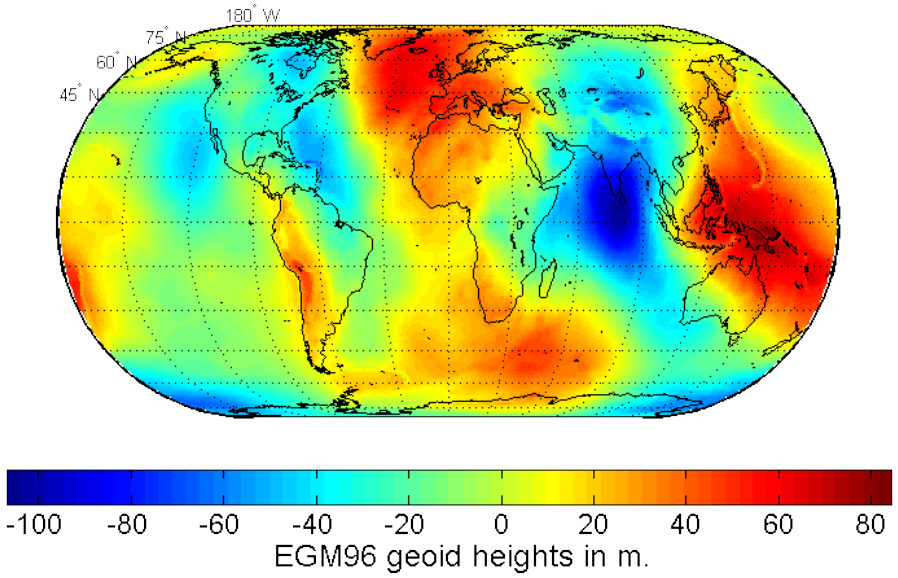

Figure 2.4: Map of geoid undulation heights from the Earth Gravitational Model 1996 (EGM 96) of Earth's mean gravity field (From: *Lemoine et al.*, 1998).

where $\Delta\overline{C}_{lm}(t)$ and $\Delta\overline{C}_{lm}(t)$ are defined by subtracting some mean coefficient field from the total time-varying coefficients (e.g., $\Delta\overline{C}_{lm}(t) = \overline{C}_{lm}(t) - \overline{\overline{C}_{lm}}$).

2.4 Surface mass variations in terms of spherical harmonics

The GRACE community is concerned primarily with the time-variable components of the gravity field. While understanding how these changes affect the geoid is important, it is often also useful to relate these changes in terms of actual surface mass variations. These mass changes can be computed by considering the surface mass density redistribution $\rho(r, \phi, \lambda)$ that cause these time-dependent changes in gravity, following *Wahr et al.* (1998); *Wahr* (2009):

$$\left\{\begin{matrix}\Delta C_{lm} \\ \Delta S_{lm}\end{matrix}\right\}_{surface} = \frac{3}{4\pi a_{\oplus}\rho_{ave}(2l+1)} \int \Delta\sigma(\phi,\lambda)\tilde{P}_{lm}(\sin\phi) \left\{\begin{matrix}\cos m\lambda \\ \sin m\lambda\end{matrix}\right\} \cos\phi \; d\phi \; d\lambda \; dr, \qquad (2.43)$$

where $\Delta\sigma$ is the change in surface mass density (mass/area) and ρ_{ave} is the average density of the Earth (5517 kg/m^3). It is not correct, however, to assume that the density anomaly is concentrated as a thin layer of surface mass change. Changes in surface loading induce deformation within the solid Earth, resulting in a density change within the Earth as well that makes up a non-negligible portion of the resulting gravity anomaly. These solid Earth loading terms can be represented by the load Love numbers k_l by

$$\begin{Bmatrix} \Delta C_{lm} \\ \Delta S_{lm} \end{Bmatrix}_{solid\ Earth} = k_l \begin{Bmatrix} \Delta C_{lm} \\ \Delta S_{lm} \end{Bmatrix}_{surface} \tag{2.44}$$

and the total surface mass density change can then be represented in spherical harmonics by

$$\begin{Bmatrix} \Delta C_{lm} \\ \Delta S_{lm} \end{Bmatrix}_{surface} = \frac{3}{4\pi a_{\oplus}\rho_{ave}} \frac{1+k_l}{(2l+1)} \int \Delta\sigma(\phi,\lambda)\tilde{P}_{lm}(\sin\phi) \begin{Bmatrix} \cos m\lambda \\ \sin m\lambda \end{Bmatrix} \cos\phi \; d\phi \; d\lambda \; dr. \tag{2.45}$$

Expanding $\Delta\sigma(\phi,\lambda)$ as a sum of orthogonal Legendre Coefficients, a total expression for changes in surface mass similar to the expression of geoid undulations is found(*Wahr*, 2009):

$$\Delta\sigma(\phi,\lambda) = \frac{a_{\oplus}\rho_{ave}}{3} \sum_{l=0}^{N_{max}} \sum_{m=0}^{l} \frac{2l+1}{1+k_l} \tilde{P}_{lm}(\sin\phi) \left[\Delta\overline{C}_{lm}\cos m\lambda + \Delta\overline{S}_{lm}\sin m\lambda\right]. \tag{2.46}$$

Finally, it is often useful to represent the mass change from Equation 2.46 in terms of the water gained or lost in the region. As discussed in the previous chapter, a majority of mass change signals observed by GRACE are water-driven signals. Therefore, to represent surface mass changes in a more meaningful term, a unit *water equivalent height* is often used rather than kg/m^2, where this height is a product of the mass change and the average density of water, $\rho_{H_2O} = 1000$ kg/m^3. For a given unit area dA, the water equivalent height in centimeters (or "cm w.e.") can be determined by

$$\Delta\sigma\ [\text{cm w.e.}] = \frac{\Delta\sigma\ [\text{kg/m}^2]}{\rho_{H_2O}\ [\text{kg/m}^3]} \times \frac{100\ \text{cm}}{\text{m}}. \tag{2.47}$$

Put together, surface mass variations in terms of water equivalent height are computed by

$$\Delta\sigma(\phi,\lambda)\ [\text{cm w.e.}] = \frac{100 a_{\oplus}\rho_{ave}}{3\rho_{H_2O}} \sum_{l=0}^{N_{max}} \sum_{m=0}^{l} \frac{2l+1}{1+k_l} \tilde{P}_{lm}(\sin\phi) \left[\Delta\overline{C}_{lm}\cos m\lambda + \Delta\overline{S}_{lm}\sin m\lambda\right]. \tag{2.48}$$

Estimates of surface mass variations in water equivalent height are then estimates of the depth of water over a unit area of the equivalent amount of mass as the variations. In other words, a change of "+10 cm w.e." would imply an increase in mass equivalent to 10 cm of water over that area. Figure 2.5 shows maps of geoid undulations and surface mass for April 2009 relative to the 2004.0-2010.0 mean field from GRACE at increasing spatial resolutions as defined by N_{max}. In determining these grids, 300 km Gaussian smoothing has been applied to remove correlated striping noise and glacial isostatic adjustment trends have been removed to show only water-driven signals. The maps show that the spatial patterns of geoid undulations contain gentler spatial variations than for surface mass changes, and also demonstrate the increased spatial resolution recovered with higher maximum degree and order N_{max}.

Having derived equations for the gravitational potential, geoid undulations, and surface mass variations, it is important to point out that, for all of these formulations, the only information needed to express each field are various constants and the same global set of normalized spherical harmonic coefficients. Therefore, it can be said that this set of spherical harmonics, or Stokes coefficients, fully describe all of these fields, and changes in gravitational potential, the geoid, or surface mass can all be fully described by changes in these coefficients. In addition, a highly optimized Matlab implementation of the geoid and surface mass equations has been included in Appendix B for reference and future use.

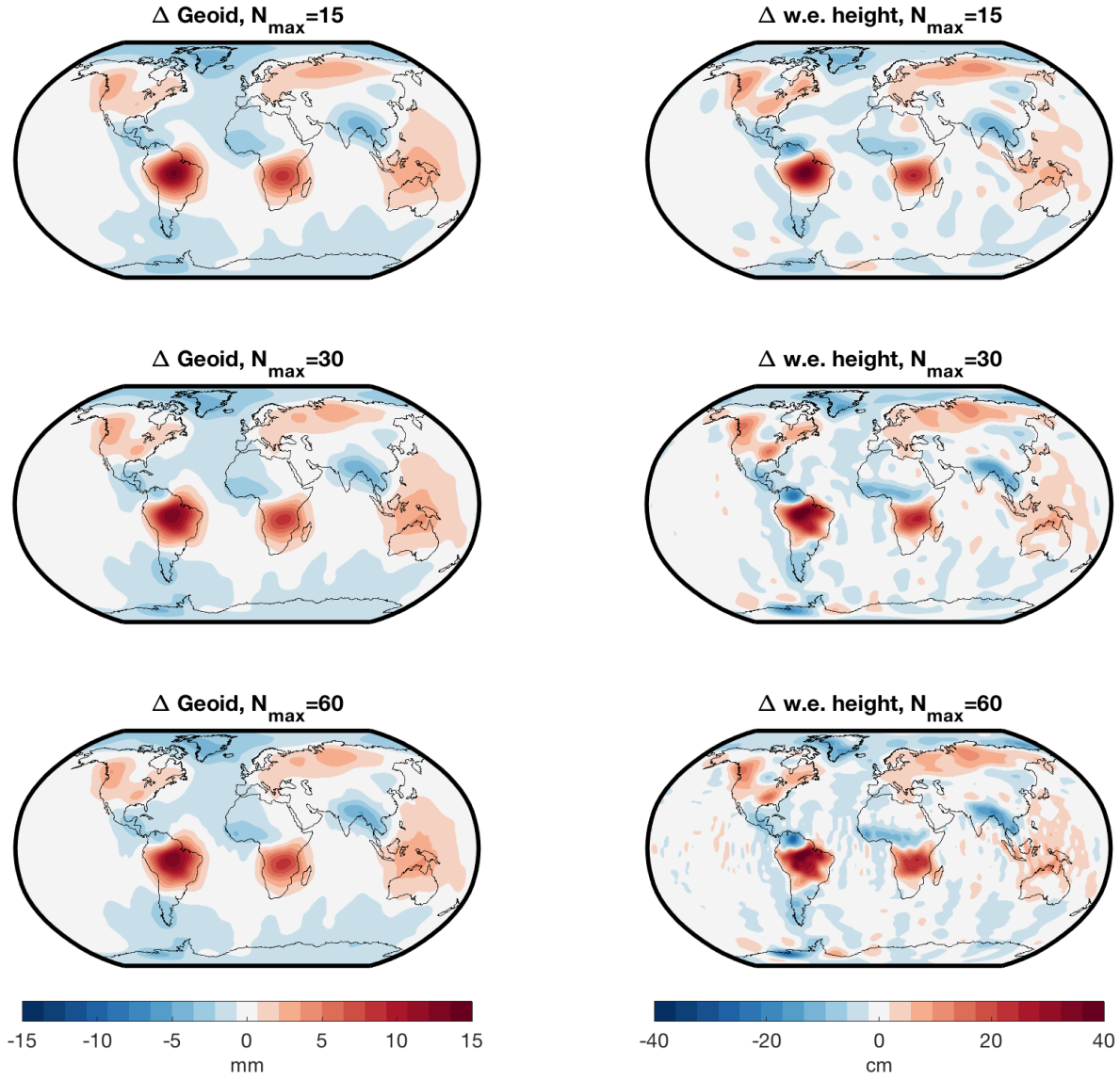

Figure 2.5: Maps of geoid undulations and surface mass changes at increasing N_{max} spherical harmonic expansions for April 2009 relative to the 2004.0-2010.0 mean from GRACE, with 300 km gaussian smoothing applied and GIA removed according to *A et al.* (2013).

2.5 The gravity field as a global set of mascons

In the previous section, surface mass variations were derived as a set of global spherical harmonic coefficients, the form in which traditional GRACE Level 2 data products are distributed. These Level 2 products are by definition unregularized, and various post-estimation techniques are applied in studies utilizing these products, as discussed in the previous chapter. This dissertation presents a new daily GRACE solution realized as a global set of regularized mass concentrations, or mascons. Whereas a spherical harmonic representation of the gravity field is truncated at some maximum degree and order N_{max}, a mascon representation in effect is a pixelation of the gravity field, with the chosen number of mascons similarly truncating the gravity field.

Here, the realization of the gravity field as a set of mascons is presented. Importantly, mascon solutions introduce the opportunity to use various regularization techniques to best capture information in the correct mascon cells, separate from other nearby but distinct cells (either geographically, geologically, or otherwise different) (*Luthcke et al.*, 2013; *Watkins et al.*, 2015). Mascons allow regularization to be spatially driven, whereas spherical harmonic regularization must be done in the frequency domain, and therefore regularization strategies dealing with things like coastal boundaries are more readily implemented in mascon space. The specific regularization strategy employed in this dissertation will be discussed in the next chapter. For now, it is only important to mention this as motivation for why mascons are used and not spherical harmonics. Similarly, the specific set of mascon cells will also be detailed at that time. Figure 2.6 shows an example set of mascon cells over the continental United States. As seen in the figure, each mascon represents the average mass signal over the cumulative area covered by each cell.

This dissertation builds on the monthly mascon solution process at GSFC to estimate daily mascons. This process utilizes a mascon formulation derived from Stokes coefficients, useful because gravity field estimation utilities at GSFC were originally defined in terms of these coefficients. The full derivation of the mascon formulation is found in *Luthcke et al.* (2013) and *Sabaka et al.* (2010), and is summarized in this section.

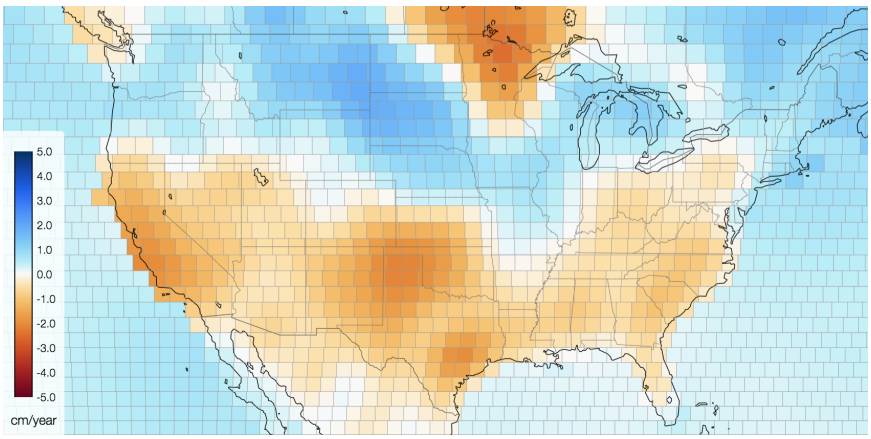

Figure 2.6: Example trend map of a set of mascon cells over the continental United States from GSFC Monthly Mascons v02.4. Each cell is representative of the total mass over the area covered by that cell. *Figure from the GRACE Mascon Visualization Tool, Appendix A.*

A global set of mascons is essentially a pixelation of the Earth into a set of discrete, equal area cells. Each cell represents the total surface mass of that cell, and mass distribution is assumed to be uniform within the cell. The mascon parameters are formulated by recognizing that a change in the gravitational potential of a region caused by the addition of a small uniform layer of mass at time t can be representing as a set of differential Stokes coefficients about a mean field. These differential coefficients can be computed as (*Chao et al.*, 1987)

$$\Delta\overline{C}_{lm}(t) = \frac{\left(1+k_l^{'}\right) R^2\sigma(t)}{(2l+1)\,M} \int \tilde{P}_{lm}(\sin\phi)\cos m\lambda \; d\Omega \tag{2.49}$$

$$\Delta\overline{S}_{lm}(t) = \frac{\left(1+k_l^{'}\right) R^2\sigma(t)}{(2l+1)\,M} \int \tilde{P}_{lm}(\sin\phi)\sin m\lambda \; d\Omega, \tag{2.50}$$

where $k_l^{'}$ is the loading Love number of degree l, R is the Earth's mean semi-major axis, $\sigma(t)$ is the mass of the uniform layer, M is the Earth's mass, ϕ and λ are geographic latitude and longitude, and Ω is the solid angle surface area of the mascon where $\sigma(t)$ is applied ($\Omega = dr\; d\phi\; d\lambda$). The uniform mass layer $\sigma(t)$ (kg m^{-2}) is expressed as the height $H(t)$ (in cm) of a uniform column of water totaling that mass by relating the density of water (1000 kg m^{-3}) to that mass, giving $\sigma(t) = 10\; H(t)$. The total mascon surface mass content is determined by accumulating the entire

spherical harmonic expansion. This allows mass change estimates to be expressed as a change in equivalent water thickness, useful in GRACE estimates as many of the dominant mass changes observed are due to changes in terrestrial water storage and ice mass change.

In this dissertation, a global set of 41,168 1-arc-degree equal-area mascons are defined, following the GSFC monthly solution's mascon definitions (*Luthcke et al.*, 2013). These mascons are defined from spherical harmonics to degree and order 60. An alternative formulation used in the JPL GRACE Mascon solution system defines a global set of mascons as a set of spherical caps (*Watkins et al.*, 2015). This system, not employed in this dissertation, estimates mascons directly from GRACE ranging measurements, and is functionally similar to the GSFC process. It should also be noted that, regardless the method used in defining a set of mascons, mascons can be defined as whatever size is deemed most appropriate. The JPL solution uses a 3-arc-degree definition to match the theoretical resolution of GRACE at the equator while this dissertation utilizes a 1-arc-degree mascon grid to better conform to coastlines.

2.6 Least squares estimation

With many physical systems, it is often the case that the observables measured by the systems and the desired information from the system are not the same thing, but that the observations are in some way related to the desired information. If the desired information, or state, is uniquely dependent on the observation, that information can be determined directly from the observations. However, for many systems the observations are both noisy and dependent on the desired information and the state that could result in those observations is non-unique. For such systems, the weighted least squares solution with *a priori* information can be used to determine a best estimate of the state. This is developed here, following *Tapley et al.* (2004b).

2.6.1 The least squares solution

The least squares solution addresses the problem where knowledge of an independent variable $\mathbf{X}$ is desired, but the only available information to determine that state is a set of parameters $\mathbf{Y}$ that are dependent on the state. In other words, the known information $\mathbf{Y}$ is a function of $\mathbf{X}$ by some operation $\mathbf{A}$ as in

$$\mathbf{Y} = \mathbf{A}\mathbf{X}. \tag{2.51}$$

Given some $\mathbf{X}$ and knowing the relating operation $\mathbf{A}$, it is straightforward to compute $\mathbf{Y}$. However, determining the state $\mathbf{X}$ from $\mathbf{Y}$ is often not so directly determinable.

In practical terms, the known dependent parameters are observations of the state, with some error ϵ. In general least squares estimation, a reference model is often used as a starting state guess, and state deviations are then estimated as a correction to that starting guess in estimating the final true state. For well observed linear systems, this initial guess can have large errors and the observations can be used to correct for these errors. In gravity estimation with GRACE observations, however, such a system would be non-linear and linear least squares estimation would break down. Instead, the system can be linearized by choosing a reference model state that is close to the truth, and representing the true state as deviations from that reference state with a first-order Taylor series expansion about the reference state. In such a setup, a state deviation vector $\mathbf{x}(t)$ of size n and observation deviation vector $\mathbf{y}(t)$ of size m are defined as

$$\mathbf{x}(t) = \mathbf{X}(t) - \mathbf{X}^*(t), \qquad \mathbf{y}(t) = \mathbf{Y}(t) - \mathbf{Y}^*(t) \tag{2.52}$$

where $\mathbf{X}(t)$ is the desired unknown state, $\mathbf{X}^*(t)$ is the reference starting model, $\mathbf{Y}(t)$ is the set of observations, and $\mathbf{Y}^*(t) = G(\mathbf{X}^*(t))$ is set of expected observations as a function of the reference state. The state deviations are then related to observation deviations, now defining $\mathbf{A}$, called the design matrix,

$$\mathbf{y}(t) = G(\mathbf{x}(t)) + \epsilon = \mathbf{A}\mathbf{x}(t) + \epsilon, \quad \mathbf{A} = \frac{\partial G}{\partial \mathbf{X}}. \tag{2.53}$$

When a best estimate of the state is computed, any remaining observation deviations will be due to the observation errors, ϵ.

The least squares solution determines an estimate of the state that minimizes the sum of the squares of the calculated observation residuals. To accomplish this, a term called the performance index is minimized, as first proposed by Gauss in 1809: (*Tapley et al.*, 2004b)

$$J(\mathbf{x}) = \frac{1}{2}\epsilon^T\epsilon. \tag{2.54}$$

Rearranging Equation 2.53 for ϵ and substituting into Equation 2.54, the performance index can be expressed as

$$J(\mathbf{x}) = \frac{1}{2}(\mathbf{y} - \mathbf{A}\mathbf{x})^T(\mathbf{y} - \mathbf{A}\mathbf{x}). \tag{2.55}$$

This equation is a quadratic function of $\mathbf{x}$, implying that the equation will have a unique minima for

$$\frac{\partial J}{\partial \mathbf{x}} = 0, \text{ and } \delta\mathbf{x}^T\frac{\partial^2 J}{\partial \mathbf{x}^2}\delta\mathbf{x} > 0 \tag{2.56}$$

for all $\delta\mathbf{x} \neq 0$. This also implies that the symmetric matrix $\partial^2 J/\partial\mathbf{x}^2$ is positive definite.

This first equation can then be determined by

$$\begin{aligned}
\frac{\partial J}{\partial \mathbf{x}} = 0 &= -\frac{1}{2}\frac{\partial(\mathbf{y} - \mathbf{A}\mathbf{x})^T(\mathbf{y} - \mathbf{A}\mathbf{x})}{\partial \mathbf{x}} \\
0 &= -\frac{1}{2}\left[(\mathbf{y} - \mathbf{A}\mathbf{x})^T\frac{\partial(\mathbf{y} - \mathbf{A}\mathbf{x})}{\partial \mathbf{x}} + (\mathbf{y} - \mathbf{A}\mathbf{x})^T\frac{\partial(\mathbf{y} - \mathbf{A}\mathbf{x})}{\partial \mathbf{x}}\right] \\
0 &= -(\mathbf{y} - \mathbf{A}\mathbf{x})^T\frac{\partial(\mathbf{y} - \mathbf{A}\mathbf{x})}{\partial \mathbf{x}} \\
0 &= -(\mathbf{y} - \mathbf{A}\mathbf{x})^T\mathbf{A} \\
0 &= -\mathbf{A}^T(\mathbf{y} - \mathbf{A}\mathbf{x})
\end{aligned} \tag{2.57}$$

The value of $\mathbf{x}$ that satisfies Equation 2.57 will be the best estimate, from here defined as $\hat{\mathbf{x}}$. Rearranging this equation gives the *normal equation*,

$$(\mathbf{A}^T\mathbf{A})\hat{\mathbf{x}} = \mathbf{A}^T\mathbf{y}. \tag{2.58}$$

Computing the second partial derivative gives

$$\begin{aligned}\frac{\partial^2 J}{\partial \mathbf{x}^2} &= \frac{\partial\left(-\mathbf{A}^T(\mathbf{y}-\mathbf{A}\mathbf{x})\right)}{\partial \mathbf{x}} \\ &= -\mathbf{A}^T(-\mathbf{A}) \\ \frac{\partial^2 J}{\partial \mathbf{x}^2} &= \mathbf{A}^T\mathbf{A} \end{aligned} \tag{2.59}$$

which is positive definite if $\mathbf{A}$ is full rank. This term, $(\mathbf{A}^T\mathbf{A})$, is called the *normal matrix* and is $n \times n$ symmetric, where n is the number of state parameters in $\mathbf{x}$. If this term is positive definite, the best estimate $\hat{\mathbf{x}}$ can be determined by

$$\hat{\mathbf{x}} = \left(\mathbf{A}^T\mathbf{A}\right)^{-1}\mathbf{A}^T\mathbf{y}. \tag{2.60}$$

The best estimate of the observation errors can then be computed by

$$\hat{\epsilon} = \mathbf{y} - \mathbf{A}\hat{\mathbf{x}}. \tag{2.61}$$

The total best estimate of the state then is the sum of the initial reference state and the best estimate of the state deviation,

$$\hat{\mathbf{X}} = \mathbf{X}^* + \hat{\mathbf{x}}. \tag{2.62}$$

2.6.2 Weighted least squares

A major shortcoming of the solution to the least squares solution, Equation 2.60, is that the observation data informing the solution is not weighted according to the accuracy of the observations. In other words, all information is considered equally, even if some information is more accurate than other. To improve on this design, observation-based weights can be assigned each term in Equation 2.53 as

$$\mathbf{y}(t) = \mathbf{A}\mathbf{x}(t) + \epsilon; \quad \mathbf{W}, \tag{2.63}$$

where $\mathbf{W}$ is an $m \times m$ symmetric matrix. If all observations are independent of one another, $\mathbf{W}$ will be a diagonal matrix, where the terms along the diagonal are the relative weights of each observation. A simple example of how this weighting matrix might look would be for a system

with four observations, where the 4th observation is half as accurate as the first three. For such a system, the weighting matrix might be

$$\mathbf{W} = \begin{bmatrix} 1 & 0 & 0 & 0 \\ 0 & 1 & 0 & 0 \\ 0 & 0 & 1 & 0 \\ 0 & 0 & 0 & 0.25 \end{bmatrix}.$$

The weighted least squares solution is then developed similarly to the standard solution, beginning with the performance index:

$$J(\mathbf{x}) = \frac{1}{2}\epsilon^T \mathbf{W} \epsilon. \tag{2.64}$$

As before, this can be expressed as

$$J(\mathbf{x}) = \frac{1}{2}(\mathbf{y} - \mathbf{A}\mathbf{x})^T \mathbf{W} (\mathbf{y} - \mathbf{A}\mathbf{x}). \tag{2.65}$$

Computing the first partial derivative and asserting that the first derivative vanishes at a minimum of $J(\mathbf{x})$,

$$\frac{\partial J}{\partial \mathbf{x}} = 0 = -\mathbf{A}^T \mathbf{W} (\mathbf{y} - \mathbf{A}\mathbf{x}). \tag{2.66}$$

The weighted normal equation is then expressed as

$$(\mathbf{A}^T \mathbf{W} \mathbf{A})\hat{\mathbf{x}} = \mathbf{A}^T \mathbf{W} \mathbf{y} \tag{2.67}$$

and if $\mathbf{A}^T\mathbf{W}\mathbf{A}$ is positive definite, the weighted least squares solution is then

$$\hat{\mathbf{x}} = \left(\mathbf{A}^T \mathbf{W} \mathbf{A}\right)^{-1} \mathbf{A}^T \mathbf{W} \mathbf{y}. \tag{2.68}$$

This can also be expressed as

$$\hat{\mathbf{x}} = \mathbf{P}\mathbf{A}^T \mathbf{W} \mathbf{y}, \tag{2.69}$$

where $\mathbf{P}$ is an $n \times n$ symmetric matrix called the variance-covariance matrix,

$$\mathbf{P} = \left(\mathbf{A}^T \mathbf{W} \mathbf{A}\right)^{-1}. \tag{2.70}$$

This matrix will be full rank and invertible if all the parameters of $\mathbf{x}$ are observable, or uniquely determinable from the observations $\mathbf{y}$. If this matrix is not full rank, additional information can be added *a priori* so as to regularize the solution and allow this matrix to be invertible.

2.6.3 Weighted least squares with *a priori* information

Least squares regularization adds *a priori* covariance ($\mathbf{P_m}$, also called the regularization matrix) and state deviation information ($\overline{\mathbf{x}}$) with errors η to the weighted least squares equation by defining

$$\Gamma = \mathbf{W}^{-1},$$
$$\hat{\mathbf{x}} = \left(\mathbf{A}^T\Gamma^{-1}\mathbf{A}\right)^{-1}\mathbf{A}^T\Gamma^{-1}\mathbf{y}$$

and

$$\mathbf{A}^* = \begin{bmatrix}\mathbf{A}\\ I\end{bmatrix}, \quad \mathbf{y}^* = \begin{bmatrix}\mathbf{y},\\ \overline{\mathbf{x}}\end{bmatrix}$$
$$\epsilon = \begin{bmatrix}\epsilon\\ \eta\end{bmatrix}, \quad \Gamma^* = \begin{bmatrix}[\Gamma_{m\times m} & [0]_{m\times n}\\ [0]_{n\times m} & \mathbf{P_m}^{-1}_{n\times n}\end{bmatrix},$$
$$\hat{\mathbf{x}} = \left(\mathbf{A}^{*T}\Gamma^{*-1}\mathbf{A}^*\right)^{-1}\mathbf{A}^{*T}\Gamma^{*-1}\mathbf{y}^*,$$

which is expressed succinctly as

$$\hat{\mathbf{x}} = \left(\mathbf{A}^T\mathbf{W}\mathbf{A} + \mathbf{P_m}\right)^{-1}\left(\mathbf{A}^T\mathbf{W}\mathbf{y} + \mathbf{P_m}\overline{\mathbf{x}}\right). \tag{2.71}$$

If the *a priori* state deviation $\overline{\mathbf{x}} = [0]$, this expression simplifies to

$$\boxed{\hat{\mathbf{x}} = \left(\mathbf{A}^T\mathbf{W}\mathbf{A} + \lambda\mathbf{P_m}\right)^{-1}\mathbf{A}^T\mathbf{W}\mathbf{y},} \tag{2.72}$$

where a scalar term λ has been introduced as an adjustable scaling parameter on $\mathbf{P_m}$, which will be helpful later in the mascon estimation design.

The regularization matrix allows constraints to be placed on the least squares estimate, ensuring the front half of the least squares solution is invertible and that a meaningful solution is

determined. By including regularization in the least squares estimate, we create a system that draws the solution away from overfitting observations to an *a priori* state. This matrix can take many forms, from a simple identity matrix, to a diagonal matrix with unique variance terms for each desired state component, to a full matrix with unique variance terms and off-diagonal covariance information. *Hoerl and Kennard* (1970) discussed ridge regression (also called Tikhonov regularization) as a method for solving ill-posed least squares problems by introducing diagonal terms in the weighting matrix to obtain biased estimates with reduced total errors. If *a priori* knowledge of the system includes information about the relative variabilities of state parameters, this can be introduced into the diagonal terms. The inclusion of off-diagonal terms in the regularization matrix allows for the inclusion of well known correlations between state parameters into the estimate. This helps draw the estimate towards a biased state more reflective of the realities of the physical system.

Finally, it is advantageous to define a final term $\mathbf{R}$ called the *resolution operator*, as in *Luthcke et al.* (2013) and *Loomis et al.* (2019, under review). If Equation 2.63 is substituted into Equation 2.72 and neglecting observation noise (i.e., $\epsilon = \mathbf{0}$) but defining $\mathbf{W}$ as before, the weighted least squares with *a priori* information equation can be expressed as

$$\hat{\mathbf{x}} = \left(\mathbf{A}^T\mathbf{W}\mathbf{A} + \mathbf{P_m}\right)^{-1}\mathbf{A}^T\mathbf{W}\mathbf{A}\mathbf{x}, \tag{2.73}$$

or

$$\hat{\mathbf{x}} = \mathbf{R}\mathbf{x}, \tag{2.74}$$

$$\boxed{\mathbf{R} = \left(\mathbf{A}^T\mathbf{W}\mathbf{A} + \mathbf{P_m}\right)^{-1}\mathbf{A}^T\mathbf{W}\mathbf{A}.} \tag{2.75}$$

The resolution operator is $n \times n$ and describes how the true state $\mathbf{x}$ is resolved as the estimated state $\hat{\mathbf{x}}$ by the weighted least squares with *a priori* information system, and is thus a measure of the effects of state observability, relative weighting, and regularization on the estimate. Each column i of the operator expresses the effects of regularization on each state parameter $\mathbf{x}_i$. If the regularization matrix is full rank, the resolution operator will also be full rank. Without regularization, the resolution operator would be an identity matrix if $\mathbf{A}^T\mathbf{W}\mathbf{A}$ is full rank.

The resolution operator has a number of applications, all relating to bias introduced into the best estimate of the state. This bias can be related as the difference between the truth and estimate,

$$l = \mathbf{x} - \hat{\mathbf{x}} \tag{2.76}$$

or, substituting for $\hat{\mathbf{x}}$ using Equation 2.74,

$$l = (I - \mathbf{R})\mathbf{x}. \tag{2.77}$$

This resulting bias matches that derived by *Hoerl and Kennard* (1970) when discussing ridge regression.

An impulse response can be defined by creating an impulse where one state parameter of $\mathbf{x}$ is 1 and all other parameters are 0, and then computing $\hat{\mathbf{x}} = \mathbf{R}\mathbf{x}$. The resulting impulse response vector represents the regularized best estimate of the truth impulse given the developed regularization, and can be examined for expected correlations between estimated state parameters. By extension, a multi-state impulse response can also be computed. For example, a mascon impulse response could be computed for a single mascon or a larger basin of mascons.

Chapter 3

Daily Solution Design and Development

In this dissertation, a new daily mascon solution is developed from GRACE Level-1B observations, building on the GSFC monthly Global Mascon Solution. The monthly GSFC solution is a set of 41,168 discrete, 1-arc-degree,[1] equal-area rectangular cells, resulting in bands of mascon cells at every latitude, ranging from 360 mascon cells at the equator to six mascon cells at $\pm 89^\circ$ latitude and one at each pole. Each cell represents a distinct portion of the Earth's surface, and the set as a whole achieves full global coverage. The daily solution developed here uses the same mascon definitions as the monthly solution, a design choice that was made to maximize uniformity between the two solutions. The daily solution design is then driven by different observability constraints and resulting regularization needs. This chapter covers the estimation of this daily solution via least squares as developed in the previous chapter, including the definitions and design of all terms in the weighted least squares with *a priori* information equation (Eqn. 2.72). The largest focus of this design is the development of a proper regularization scheme for daily estimates.

In GRACE gravity field estimation, observations comprised of K-band range-rate and GPS positioning are used to estimate a state consisting of the time-variable garavity field as well as a set of orbital arc parameters, while star tracker satellite orientation and accelerometer external force measurements are used to orient and correct these observations. In turn, the observation deviation vector is computed as the difference between measured and expected measurements given GRACE orbital information and a background gravity field model. This background gravity field for the

[1] A "1-arc-degree" mascon is approximately 111 km on each side.

GSFC monthly solution consists of a static field, an atmosphere and ocean de-aliasing (AOD) model, an ocean tidal model, solid earth and pole tide models, and a glacial isostatic adjustment (GIA) model. Recalling Equation 2.52,

$$\mathbf{x}(t) = \mathbf{X}(t) - \mathbf{X}^*(t),$$

the state deviation vector is computed as the best estimate of deviations between the true gravity field $\mathbf{X}(t)$ and the background reference field $\mathbf{X}^*(t)$ represented in terms of water equivalent thickness over a discrete set of mascon cells covering the surface of the earth, as well as the converged arc parameter deviations (*Luthcke et al.*, 2013). The daily product developed in this dissertation uses the same background model as the GSFC monthly solution, but also includes the converged monthly GSFC estimate as a time-variable component over each month. These monthly solutions were included as step functions over each month, as the monthly estimates represent the total average solution over each month. These models are summarized in Table 3.1. As a result, the signal content of the observation deviation vector, $\mathbf{y}(t) = \mathbf{Y}(t) - G(\mathbf{X}^*(t))$, is due to residual sub-monthly variations in the gravity field that are aliased into each monthly period during the monthly solution estimation. The state deviation vector then contains these sub-monthly variations at each mascon cell, and the goal of this research is to build a system which recovers these state deviations. As a result, this estimate is designed as a hierarchical product in which high-spatial and low-temporal resolution monthly solutions are coupled with lower-spatial and higher-temporal resolution daily estimates to maximize both the spatial and temporal information contained within the final estimate.

Figure 3.1 shows an example of recovered daily signal for a single basin in the first half of 2012. The recovered signal in this estimate will be considered later in Chapter 5, and this figure is included here to illustrate the daily solution as an estimated delta to the monthly solution. Note that 5-day boxcar smoothing has been applied to the final solution simply to highlight the magnitude and evolution of the recovered daily signal. Additionally, a data gap from mid-April through May due to a lack of useful GRACE observations during this time can be seen. Because

the monthly solution is included in the reference model for the least squares system, GRACE data gaps will have no additional impacts on the developed daily solutions beyond general processing difficulties already experienced with monthly GRACE solutions.

Table 3.1: Summary of reference forward model components for daily mascon estimation

Force Model	Description
Static Gravity Field	GOCO-05S with epoch of 2008.0
Tide Model	GOT4.7 (90×90) (*Ray*, 1999)
AOD	ECMWF+MOD2D (*Carrère and Lyard*, 2003)
Geocenter Correction	*Swenson et al.* (2008)
C_{20}	Replace C_{20} with estimate from *Cheng et al.* (2013)
C_{21}/S_{21} Pole Tide	*Wahr et al.* (2015)
Monthly Gravity Field	GSFC Global Mascons (*Luthcke et al.*, 2013)
GIA	*A et al.* (2013)

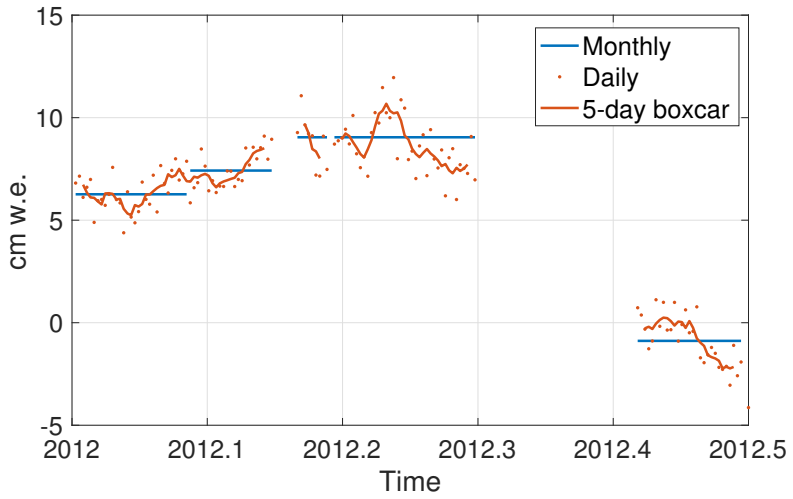

Figure 3.1: Daily solution recovery for an example basin, where the total daily signal is the sum of the forward-modeled monthly GSFC solution and the estimated daily deviations.

3.1 Mascon estimation with a least squares approach

This dissertation uses the weighted least squares with *a priori* solution to estimate the global set of mascons at each day. Recalling Equation 2.72,

$$\hat{\mathbf{x}} = \left(\mathbf{A}^T\mathbf{W}\mathbf{A} + \lambda\mathbf{P_m}\right)^{-1}\mathbf{A}^T\mathbf{W}\mathbf{y},$$

each term of the least squares solution must be properly defined and a regularization strategy must be developed to ensure a stable and meaningful solution. The state deviation vector $\hat{\mathbf{x}}$ consists of the desired mascon states each day, which will be estimated from the GRACE observation deviations $\mathbf{y}$ mentioned above. An observation weighting matrix $\mathbf{W}$ is used of the same form as in the monthly GSFC product. This weighting matrix accounts for uncertainties η due to measurement noise. This leaves the design matrix $\mathbf{A}$ and regularization matrix $\mathbf{P_m}$ to be defined in the next two sections.

Before continuing, given that this new solution is resolved on the same set of mascons as the monthly GSFC solution and uses that monthly solution in the reference state model, an important point is that the final estimated state is in effect an iteration of the GSFC monthly solution at daily timescales. Daily estimates are deviations from the GSFC monthly solution, and the total daily signal is then the linear combination of these daily estimates with the monthly solution:

$$\hat{\mathbf{X}}(t) = \mathbf{X}^*(t) + \hat{\mathbf{x}}(t). \tag{3.1}$$

3.2 The design matrix, A

The first important component of the least squares equation to determine is $\mathbf{A}$, the design matrix. Recalling Equation 2.53,

$$\mathbf{y}(t) = G(\mathbf{x}(t)) + \epsilon = \mathbf{A}\mathbf{x}(t) + \epsilon, \quad \mathbf{A} = \frac{\partial G}{\partial \mathbf{X}}.$$

In other words, $\mathbf{A}$ contains the partial derivatives of the observations in the system with respect to the desired state, or the information needed to map GRACE observations as mascon mass estimates. Therefore, an expression is needed for these partial derivatives. This section follows

Sabaka et al. (2010) and *Luthcke et al.* (2013) in defining these mascon parameters from differential Stokes coefficients.

The mascon state deviations are related to GRACE observation deviations by defining the design matrix as

$$\mathbf{A} = \frac{\partial G(\mathbf{X}^*)}{\partial \mathbf{X}} \equiv \mathbf{HL}, \qquad \mathbf{H} = \frac{\partial G(\mathbf{X}^*)}{\partial \mathbf{V}}, \qquad \mathbf{L} = \frac{\partial \mathbf{V}}{\partial \mathbf{X}}, \tag{3.2}$$

where $\mathbf{V}$ is the set of differential Stokes coefficients C_{lm} and S_{lm} to maximum degree and order N_{max}. This relates the mascon state to GRACE observations through $\mathbf{H}$, the partial derivatives of GRACE KBRR observations each day with respect to the differential Stokes coefficients, and $\mathbf{L}$, the partial derivatives of the differential Stokes coefficients with respect to the mascon state parameters.

An alternative way to express the relationship in Equation 3.2 is for a single mascon surface mass estimate H_j and single observation O_i by

$$\frac{\partial O_i}{\partial H_j(t)} = \sum_{l=1}^{l_{max}} \sum_{m=0}^{l} \frac{\partial O_i}{\partial \overline{C}_{lm}} \frac{\partial \Delta \overline{C}^j_{lm}(t)}{\partial H_j(t)} + \frac{\partial O_i}{\partial \overline{S}_{lm}} \frac{\partial \Delta \overline{S}^j_{lm}(t)}{\partial H_j(t)}. \tag{3.3}$$

This formulation shows the total accumulation of the mascon over all l and m through each Stokes coefficient. Regardless of form, this developed relationship is advantageous because it allows already developed software for determining the gravity field from GRACE as a set of differential Stokes coefficients to be useful in determining a mascon solution.

Like in the monthly mascons, this work leverages the GEODYN Orbital and Geodetic Parameter Estimation program to compute partial derivative terms of GRACE KBRR observations each day with respect to the differential Stokes coefficients as part of the KBRR reduction and Level-1 data processing. These partial derivatives are accumulated into $\mathbf{H}$ from above, which is size $N_{obs} \times k$.[2]

[2] where k is the number of stokes coefficients computed in the GEODYN setup. For $N_{max} = 60$, there are 3691 total C_{lm} and S_{lm} coefficients.

L is then determined from Equation 2.49, where the mascon surface mass variations were related to the set of Stokes coefficients by integrating over the mascon area for

$$\Delta\overline{C}_{lm}(t) = \frac{\left(1+k_l^{'}\right) R^2\sigma(t)}{(2l+1)\,M} \int \overline{P}_{lm}(\sin\phi)\cos m\lambda \; d\Omega$$
$$\Delta\overline{S}_{lm}(t) = \frac{\left(1+k_l^{'}\right) R^2\sigma(t)}{(2l+1)\,M} \int \overline{P}_{lm}(\sin\phi)\sin m\lambda \; d\Omega.$$

Partial derivatives for each differential Stokes coefficient with respect to each mascon j are then determined by

$$\frac{\partial\overline{C}_{lm}}{\partial\sigma_j} = \frac{\left(1+k_l^{'}\right) R^2}{(2l+1)\,M} \int \overline{P}_{lm}(\sin\phi)\cos m\lambda \; d\Omega, \tag{3.4}$$
$$\frac{\partial\overline{S}_{lm}}{\partial\sigma_j} = \frac{\left(1+k_l^{'}\right) R^2}{(2l+1)\,M} \int \overline{P}_{lm}(\sin\phi)\sin m\lambda \; d\Omega, \tag{3.5}$$

which are accumulated into **L** (size $k \times 41,168$). Computationally, it is helpful to note that these terms are time-invariant, meaning that they can be pre-computed and stored for more efficient mascon estimation.

3.3 Design of the mascon regularization matrix, $\mathbf{P_m}$

GRACE Level-1B data processing provides observation measurements every five seconds, or 17,280 observations per day. Spatially, these observations are spaced over approximately 15 polar orbits each day, and the nearest orbital pass for a mascon on any given day can range from directly above that mascon to more than 1,400 km away, shown in Figure 3.2. Depending on any given day's orbital geometry, certain mascons will be more or less well observed. Together, this poses a major observability problem: given the number of mascons in the estimated state and the low number of observations and poor coverage of some places by these observations, the matrix $\mathbf{A}^T\mathbf{W}\mathbf{A}$ will not be full rank and the system will not be able to meaningfully resolve a gravity field solution using the observation information alone.

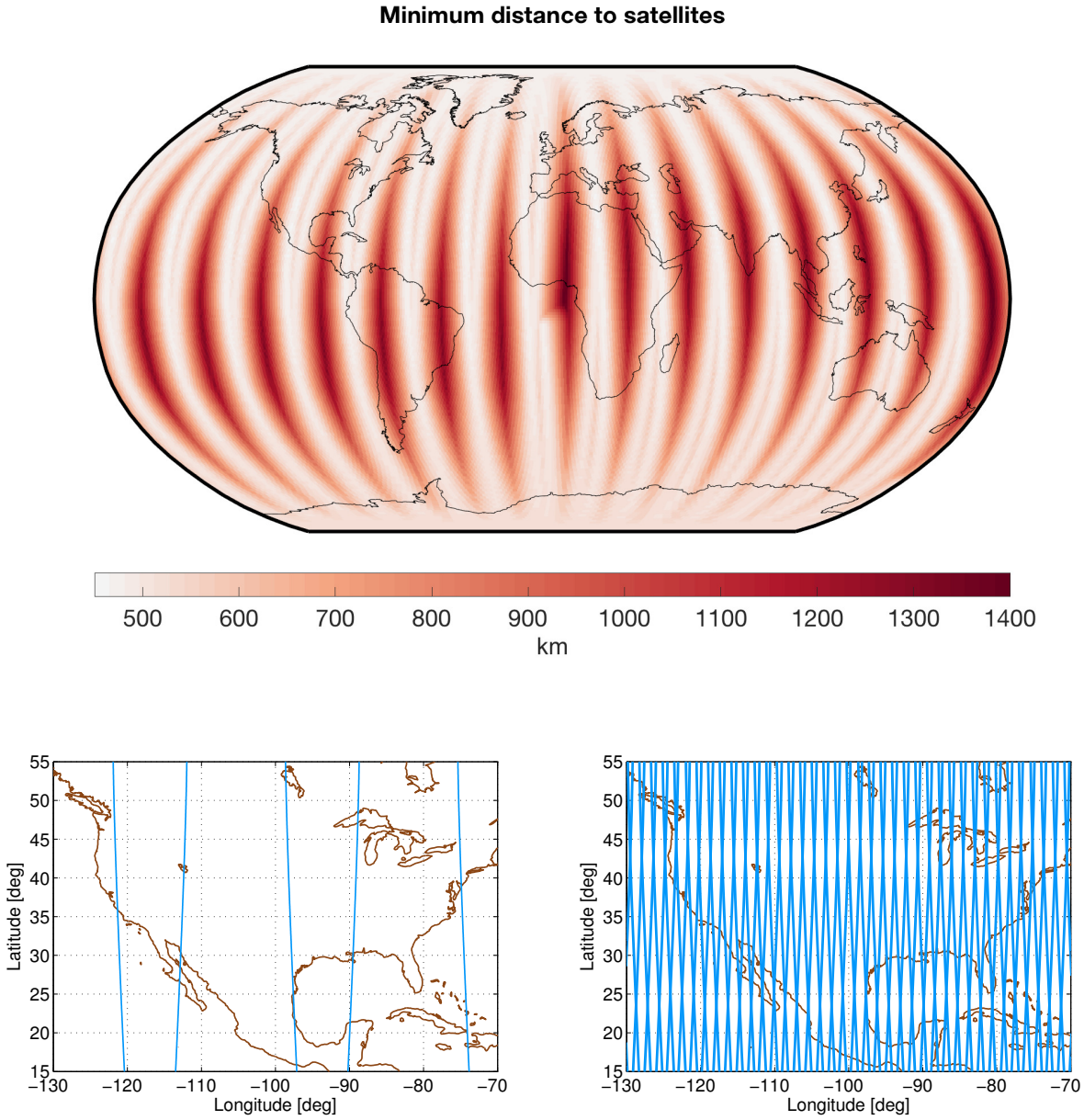

Figure 3.2: (Top) The distance of closest approach for each mascon relative to the GRACE orbit for an example day. (Bottom) 1-day coverage is compared to 30-day coverage over North America from GRACE.

In the monthly GSFC mascon solution, *a priori* covariance information is used to regularize the least squares solution and drive solution convergence. A major reason this is required is the geometry of observation data from GRACE. The mission's polar orbit provides excellent along-track coverage with many successive observations in this direction along a single track, helping isolate signals well across latitudes. On the other hand, GRACE shows relatively poor cross-track resolution, where signals can only be isolated in longitude by successive nearby orbital paths often separated by many days, especially at lower latitudes. In unregularized GRACE Level-2 spherical harmonic products, this leads to vertical striping in the recovered gravity field, which is then corrected for using various destriping algorithms (e.g., *Swenson and Wahr*, 2006). Regularization allows these effects to be handled as part of the Level-1B processing, rather than as a post-processing technique.

A daily solution has even greater need for regularization to overcome these additional observability issues. This section discusses the design of the regularization matrix $\mathbf{P_m}$ developed in this dissertation to enable meaningful estimations of daily solutions and discusses that design's relationship to the monthly GSFC solution regularization scheme. The final regularization design is a combination of multiple strategies each aimed at addressing specific observability issues. As discussed in Section 2.6.3, a simple diagonal matrix (even an identity) could be used to constrain the solution. However, the following sections present a full *a priori* variance-covariance constraint that makes use of cross-mascon correlations and unique state component weighting to better regularize the least squares solution and form a more well-posed system.

3.3.1 Cross-mascon correlations

A significant challenge in estimating a daily set of 41,168 mascons is a relative lack of observations on daily timescales. With fewer observations than unknowns, daily estimates must both overcome geometric observability problems and a problem of sparse information. To that effect, one strategy to improve observability is to effectively reduce the set of uniquely determined mascon state parameters by introducing correlations between mascons.

Sabaka et al. (2010) showed that exponentially decaying spatial and temporal constraints could be used for isolating a GRACE-recovered signal to the appropriate mascon cells in conjunction with regional constraints isolating mascons in a cryospheric region of interest from outside mascons. A combined regional and spatiotemporal constraint was defined between two mascons i and j in regions R_i and R_j as

$$W_{kk} = \begin{cases} \exp\left(2 - \frac{d_{ij}}{D} - \frac{t_{ij}}{T}\right), & R_i = R_j \\ 0, & R_i \neq R_j \end{cases}, \tag{3.6}$$

where d_{ij} is the distance between the two mascons, t_{ij} is the time between observations, and D and T are scale factors. Therefore, mascons in similar regions were tied together spatially and temporally, and mascons from non-similar regions were not tied together, as depicted in Figure 3.3. (*Sabaka et al.*, 2010). The driving principle behind this regularization is the requirement that all distinct mascon differences be close to zero in a statistical sense. These constraints were shown to

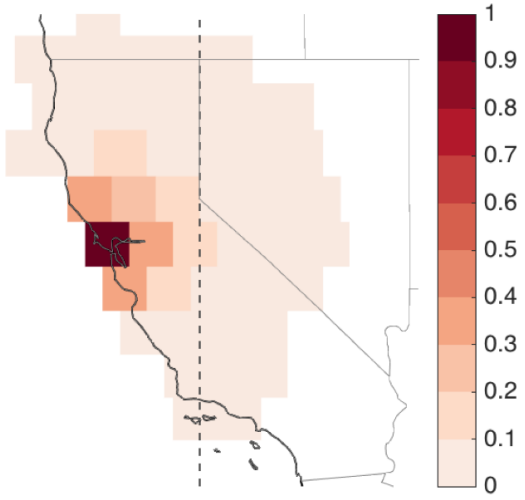

Figure 3.3: Each mascon is spatially correlated with similar mascons by an exponential function in Equation 3.7. This figure shows the correlations for the San Francisco mascon with surrounding mascons. Notice that mascons west of San Francisco (those in the Pacific Ocean) are not correlated with those over land, reducing leakage of recovered TWS signals into the oceans.

effectively ensure that mass loss signals were observed in those locations where such mass changes would be expected to occur (such as over land for glacial ice loss, and not over the oceans). These principles have enabled the development of the GSFC monthly GRACE mascon solution, using 11 regional boundaries including separate high and low elevation Greenland regions, Antarctica, the Gulf of Alaska glaciers, land, open ocean, and certain inland seas, though temporal constraints are no longer included in that solution.

In the daily solution developed in this dissertation, spatial constraints imposing cross-mascon correlations are employed. As a primary goal of this dissertation is to design a daily GRACE solution where each day is resolved independently of other days and quantify the effectiveness of such a solution, this solution also eliminates the temporal constraints from Equation 3.6, and defines spatial-only constraints as

$$W_{kk} = \begin{cases} \exp\left(1 - \frac{d_{ij}}{D}\right), & R_i = R_j \\ 0, & R_i \neq R_j \end{cases}, \tag{3.7}$$

where $D = 100$ km.

A significant difference between this daily spatial constraint implementation and the monthly implementation is in the design and number of regions, as lower spatial sampling necessitated that smaller regions be handled differently, as discussed below. In the developed daily solution, only four regions are defined: Greenland, Antarctica, Land, and Ocean. Whereas the monthly solution separates high elevation interior Greenland from low elevation coastal Greenland, the daily solution combines these as a single region. A major motivation for the original separation was to help isolate Greenland ice mass loss in lower coastal areas where long term ice mass loss is known to be taking place, but with the daily solution, these long-period changes are already determined by the monthly estimate, and improved observability by resolving the whole of Greenland as one region makes sense. Similarly, whereas the monthly solution separates the glacial portions of the Gulf of Alaska from the rest of the North American continent to help spatially isolate ice mass loss in the area, the daily solution combines the Gulf of Alaska region into the general Land region to improve sub-monthly observability. Land and Ocean then constitute the remaining two regions, which helps to isolate

TWS signals over land and eliminate leakage of these signals into the oceans.

Land and ocean regional definitions in the daily solution also differ slightly from the monthly solution. Certain small, relatively remote land masses were found to not be observable for many days, and too small for spatial correlations to properly tie these masses to better-observed land mascons nearby. As a result, mascons in Iceland, New Zealand, and the Arctic islands of Svalbard and Novaya Zemlya were redefined as ocean mascons and constrained accordingly. Without this change, the recovered mass signals in these basins were overwhelmingly dominated by noise, even in more-heavily constrained solutions with high λ values. Figure 3.4 shows examples of poorly recovered signals in Iceland and New Zealand, where the distance to GRACE's closest approach on any given day can vary by over 1000 km.

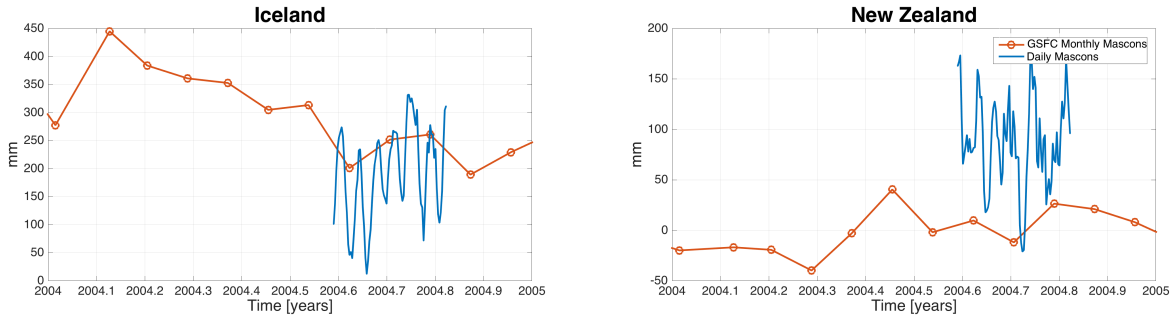

Figure 3.4: Small, isolated land masses such as New Zealand and Iceland are especially difficult to accurately estimate on daily timescales with GRACE due to very large fluctuations in the distance of the land mass to GRACE's nearest pass each day.

3.3.2 Mascon-dependent weighting

In addition to cross-mascon spatial constraints, a regularization matrix can be designed that constrains each mascon more or less based on any number of considerations. While an identity matrix can effectively constraint a least squares solution by applying a properly determined scaling factor to the identity, including unique weights for each state component can allow a better resolved estimate, as discussed in Section 2.6.3. Mascon solutions developed at JPL and CSR

have shown that mascon weighting based on some map of expected signal strength can improve the determinability of a mascon solution (*Watkins et al.*, 2015; *Save et al.*, 2016). JPL informs *a priori* covariance information from model outputs of TWS, more or less heavily constraining each mascon based on the expected signal recovery in those mascons according to the model. CSR uses a similar approach but bases these constraints on GRACE information itself. The GSFC monthly solution takes a different approach, primarily relying on their spatial constraints as a statistically-driven constraint model. However, they do introduce mascon-dependent weights in a few related ways through an iterative process. First, an initial iteration helps isolate the majority of time-variable gravity signals over land by applying lower constraints over land than over ocean, and then by binning range-acceleration residuals over mascons to build each additional iteration's mascon-dependent weighting scheme (*Loomis et al.*, 2019, under review). Additionally, the GSFC applies a latitude-dependent weight to all iterations, where better-observed high-latitude mascons are less constrained by spatial correlations. All these various constraining techniques demonstrate a characteristic of mascon solutions less easily seen in spherical harmonic solutions: the ability to drive the recovery of daily surface mass fluctuations with location-specific statistical constraint methods.

To best resolve model-independent daily estimates of TWS globally, this dissertation ultimately employs a mascon-dependent weighting strategy similar to that in the GSFC monthly solution. The two major components of this strategy are: 1) increase open ocean constraints by a factor of 10000 and inland sea constraints by a factor of 1000 as compared to land constraints, and 2) utilize latitude-dependent constraints that reflect better observability at higher latitudes. The first reflects that this solution is designed to recover terrestrial water storage signals rather than ocean signals, while the second allows better observed locations to more readily adjust to the GRACE observations. This latitudinal weighting was developed from GRACE error analysis by *Wahr et al.* (2006), which determined that GRACE signal recovery is best at higher latitudes, due to higher observation counts and better orbital geometry, and worst at latitudes just north and south of the equator, where orbit crossovers reduce the total spatial coverage of the GRACE orbit.

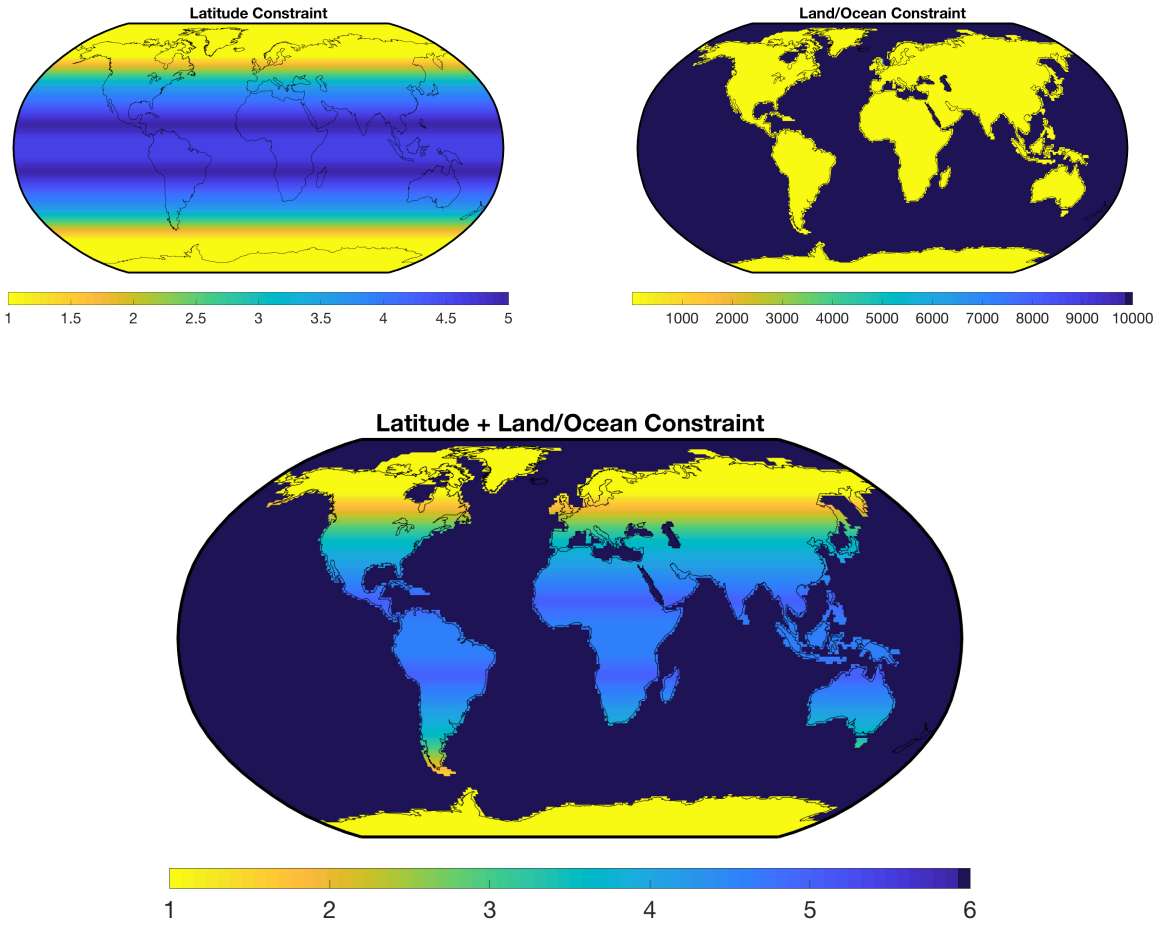

Figure 3.5: (Top-Left) Latitude-dependent weighting for each mascon, reflecting mascon observability due to orbit geometry. (Top-Right) Land-Ocean weighting constraining ocean mascons by a factor of 1000 more than land mascons. (Bottom) Combined effect of both weighting strategies.

This design therefore allows higher latitude mascons to vary more independently of spatial correlation constraints than lower latitude mascons. A map showing these combined effects is shown in Figure 3.5.

Changes to ocean mascons are in effect heavily constrained and strongly correlated across very large spatial scales, and therefore daily ocean signals are significantly dampened. This design choice was made largely due to the focus of this work on developing daily terrestrial water storage

estimates for hydrologic applications, allowing efforts to be concentrated on evaluating and best recovering these signals. Ocean mascons are not held fixed, but rather are highly constrained so as to significantly diminish spatial signal recovery over these mascons. This is not to say that ocean mass does not change on daily timescales, but rather assumes that these changes are 1) in part already captured by the ocean de-aliasing product in the reference forward model (see Table 3.1), and 2) that errors in the de-aliasing product are small enough that residual ocean signals are significantly smaller than residual land signals. In practical terms, this means that while all 41,168 mascons are included in the global solution, approximately 14,000 land and glacial mascons make up the predominant portion of the estimated daily fields, improving overall system observability. An additional resulting effect of this combined constraint is that daily signals over those small land masses that were redefined as ocean mascons are not meaningfully recovered in the developed solution.

3.3.3 Determination of global weighting factor, λ

When defining the weighted least squares with *a priori* solution, a scaling factor term λ was added. This factor is a relative weighting factor between the observation component and the *a priori* component of the estimation system, where larger values of λ more heavily weight the regularization constraint and smaller values more heavily weight daily observations. This parameter must therefore be tuned to meet some desired criteria in the resulting estimated state.

In addition to reducing leakage between regions, a primary motivation for developing a regularized solution is the reduction of striping and other correlated errors present in GRACE Level-2 spherical harmonic solutions. Rather than requiring signal post-processing to remove these correlated errors, a properly designed regularization strategy will account for these errors in the Level-1B processing and estimation step. Daily solutions are especially subject to these types of errors, as two adjacent orbital tracks may be separated by 1500 km or more, and poorly observed mascons between these tracks can be especially subject to correlated errors in a poorly regularized solution. Figure 3.6 shows two consecutive estimated days where poor solution regularization results in a

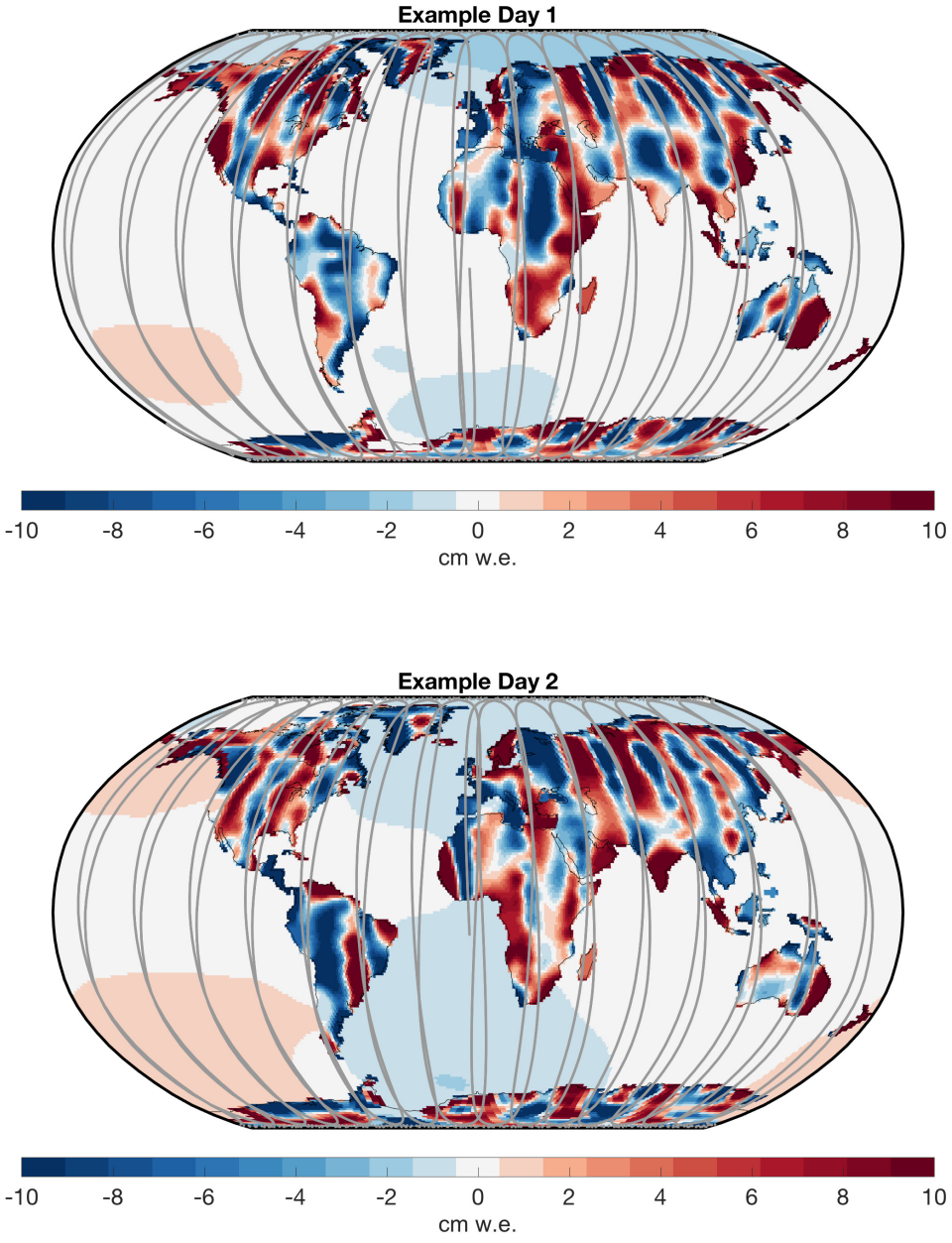

Figure 3.6: Example daily solution resulting from a poorly regularized least squares solution for two consecutive days. Daily orbit observations are depicted in gray, highlighting the low spatial sampling in the observations. Non-physical vertical striping and correlated errors dominate the recovered estimate.

mascon estimate dominated by vertical striping and correlated errors. Comparisons between days shows that these errors are also time varying, reinforcing the non-physicality of the signals.

To drive the solution toward a meaningful estimate for daily TWS changes, the design criteria for the λ parameter in the estimation is the removal of large vertical striping in the solution with the smallest possible weight λ so that the estimate can be informed by the daily observations over the regularization matrix $\mathbf{P_m}$ as much as possible. This criteria ensures maximum signal recovery spatially given the general regularization matrix design. To determine this weight, an initial λ of 10^{-6} was established and this value was iterated with increasingly larger values. A λ value of 2×10^{-4} was determined to be the minimum value where vertical striping is eliminated. Figure 3.7 shows the recovered mass signal from estimates for a sample of tested λ values for the same day.

3.3.4 Alternative regularization strategies considered

At this point, it is also appropriate to note that other mascon-dependent weighting schemes were investigated during the course of this dissertation and found to not meaningfully improve signal recovery while also adding additional challenges to quantifying errors due to these schemes. One such design imposed mascon-dependent weights based on the RMS of the de-trended monthly GSFC solution, as in Figure 3.8. Similarly, weighting based on the RMS of the de-trended solution with seasonal signals removed was also considered, which would reflect the shorter-term variations in the GRACE data. Both designs follow the general idea behind model- or GRACE-driven mascon regularization constraints in monthly products from JPL and CSR, though both RMS models are simplifications of those centers' implementations. These models did not show meaningfully different signal recovery, as shown in Figure 3.9, and ultimately were abandoned so as to not bias recovered daily signals with non-daily spatial information. A key concern with any such models is that the spatial patterns enforced by these constraint models would force the signal recovery in the daily solutions to match patterns that may or may not accurately reflect daily signal distribution, and there is low confidence that any such parameterization would perfectly represent daily spatial distributions of TWS. Further, a primary goal of the daily solution developed here is to be GRACE

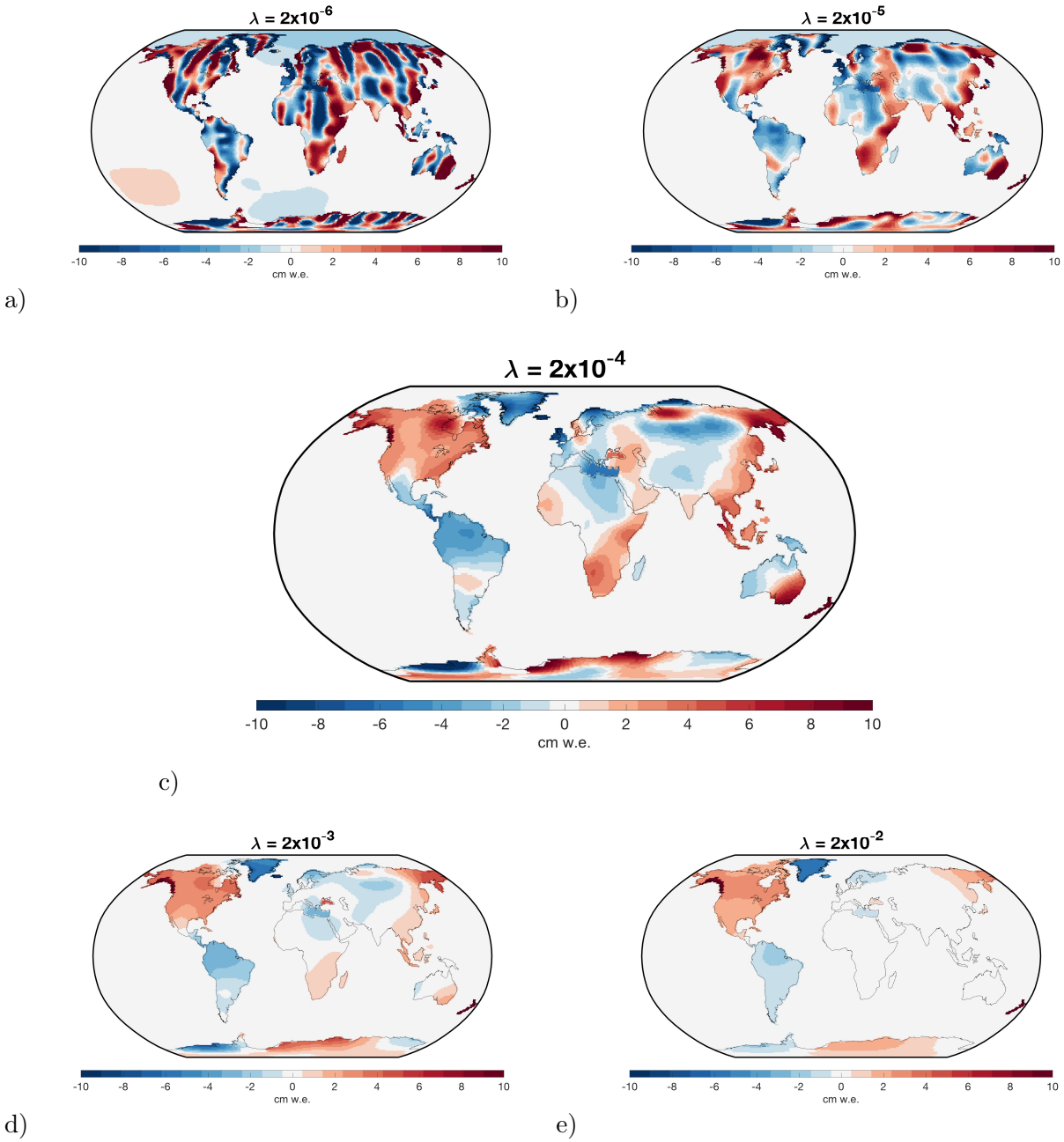

Figure 3.7: Estimated mascon solution for a single day with increasing regularization weighting factors: a) $\lambda = 2\times10^{-6}$, b) $\lambda = 2\times10^{-5}$, c) $\lambda = 2\times10^{-4}$, d) $\lambda = 2\times10^{-3}$, e) $\lambda = 2\times10^{-2}$. A weight of 2×10^{-4} was found to be the smallest weight where large vertical striping errors were eliminated. For larger values of λ, over-regularization quickly becomes a problem, and the ability of the solution to resolve any signals spatially quickly diminishes given the other constraint parameters.

data-driven alone, and any added information along these lines would move the developed solution away from this goal.

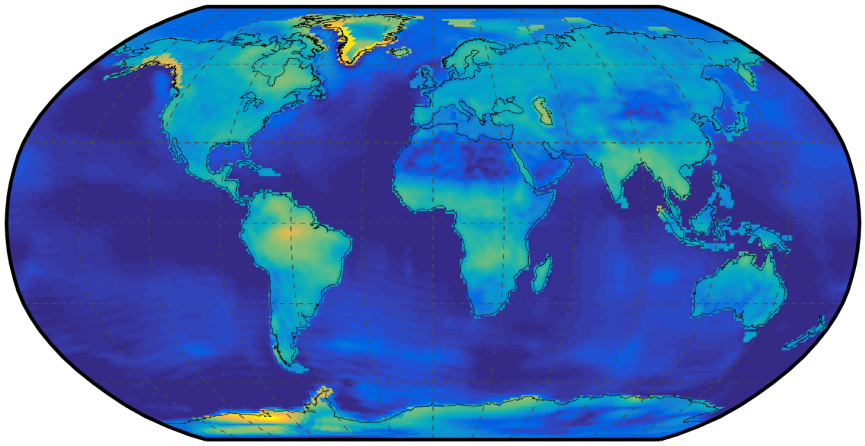

Figure 3.8: Mascon-dependent weighting based on various models, such as the RMS of the de-trended monthly GRACE solution shown here, did not measurably improve signal recovery.

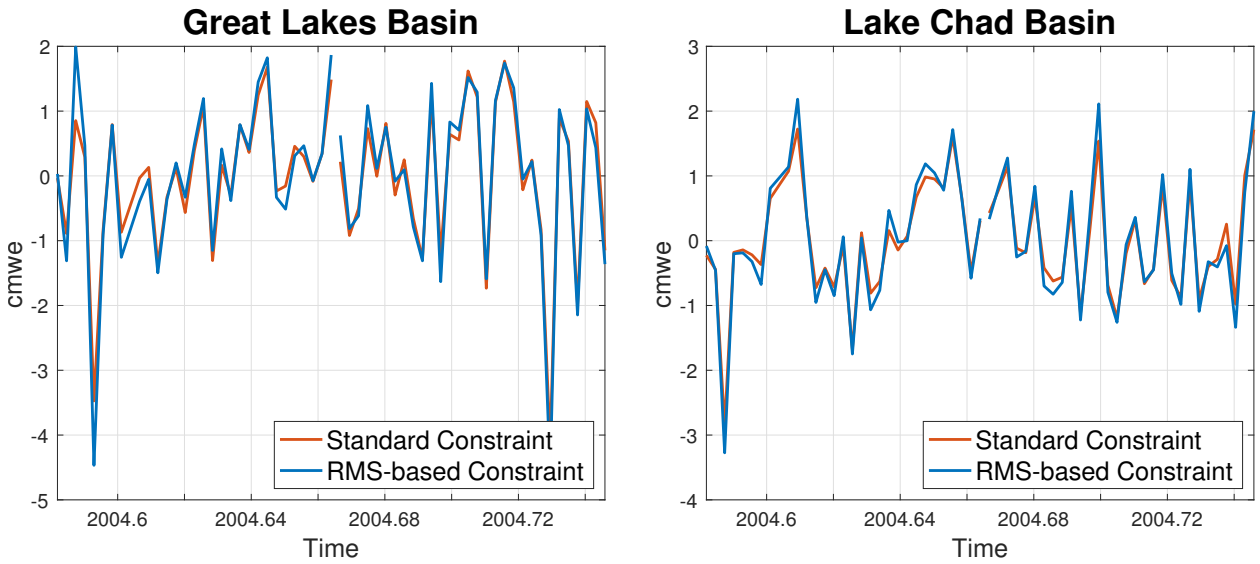

Figure 3.9: Comparison of selected "Standard Constraint" and alternative "RMS-based Constraint" schemes for two examples basins in North America (left) and Central Africa (right). Little difference was seen between two techniques, even in areas most affected by the RMS-based regularization scheme such as the Lake Chad basin on the edge of the Sahara Desert.

Additionally, other system designs were considered but ultimately not chosen. An initial proposal for a daily Kalman-filtered solution using each day's estimation as the basis for the next day's estimate was ultimately not pursued because such a solution would not be a true daily estimate, and would instead have potentially ambiguous temporal correlations. Two types of "swath" constraints were considered before being abandoned because it became impossible to objectively define the spatial structure of these swaths. One such design included a parameter where all mascons within an N kilometer swath of the GRACE orbit on a given day were fully estimated and those outside this range were help fixed, illustrated in Figure 3.10 a) for a 575 km swath. The other considered design computed variably weighted constraints for each mascon based on the proximity of that mascon to the nearest orbital pass, illustrated in Figure 3.10 b). Mascons farthest from the GRACE orbit each day would be allowed to vary least, while those closest were allowed to vary most. Both swath systems were eventually rejected because both insufficiently addressed a major question related to GRACE observability: given that along-track resolution far exceeds cross-track resolution, how can a swath of any type be defined that restricts the signal recovery cross-track in a rigorous way? In other words, if GRACE cannot tell the difference between a small signal directly below the satellites and a larger signal away from the track of the satellites, a swath design will likely artificially place signals in spatially constrained areas where they may not actually originate due to the imposed constraints of such a system. Instead, by solving for a global set of mascons each day without these swath constraints, this dissertation relies on spatial information given by the observations and regularization constraints to effectively determine the resolution of each recovered mascon, which will be discussed in Chapter 5.

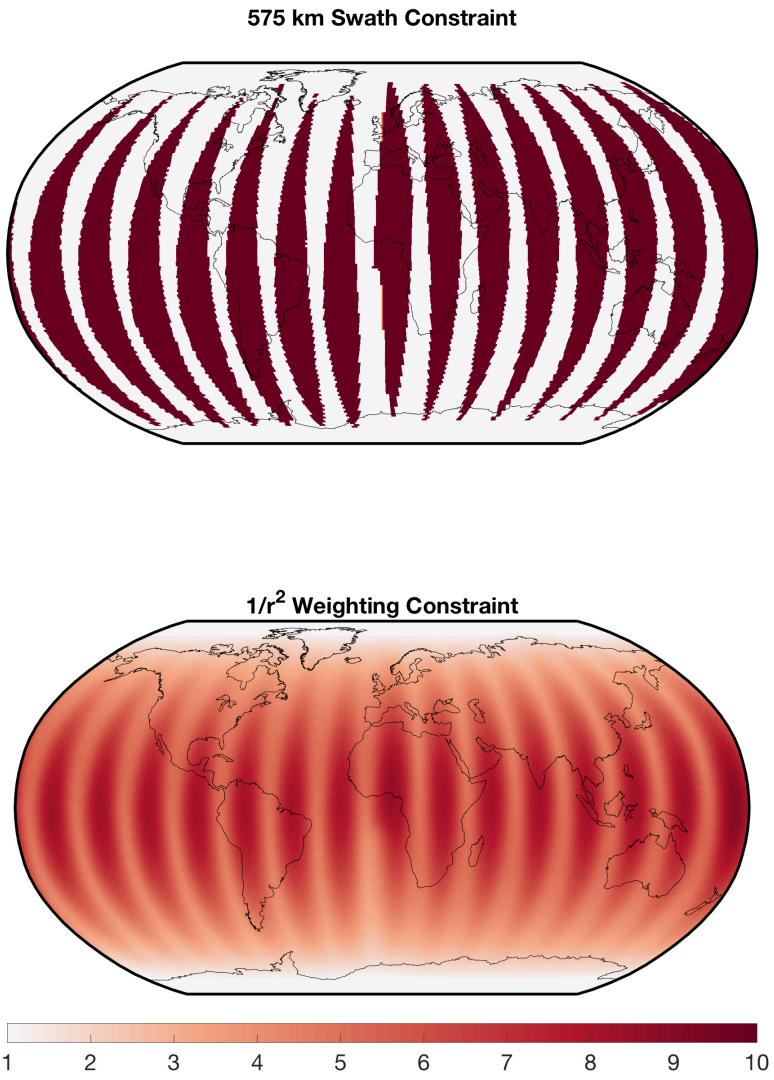

Figure 3.10: (Top) A daily "swath", or extension of the GRACE groundtrack for a given day, defines constraints allowing only those mascons within a certain cross-track distance of the groundtrack to be adjusted on a given day. Here a 575 km swath is depicted, showing mascons in white that are contained within the estimated daily swath and mascons in red that are not estimated on that day. (Bottom) An example variably weighted swath constraint defined from the square of the distance between each mascon and its nearest orbital approach, where the best observed mascons are constrained by a factor of ten less than the worst observed mascons.

3.4 Summary

Chapter 3 describes the daily mascon solution realization developed in this dissertation as an extension of the GSFC monthly mascon solution. Theory presented in Chapter 2 is developed in terms of mascon estimation, and the many parts of the least squares solution are defined. Background models informing the least squares reference state and GRACE observational information are presented. The focus of the chapter is on design considerations and decisions relating to proper regularization of the solution. The developed solution uses similar style constraints as the GSFC monthly product, adding a certain degree of consistency to the solution, but key differences in the implementation of these constraints are detailed to allow for the solution to recovery meaningful TWS signals. Finally, certain regularization strategies that were considered but ultimately not included in the final solution design are presented, and the rejection of these design strategies was discussed. In Chapter 4, the presented solution design is investigated via a simulation study to characterize expected signal recovery in the solution. Chapter 5 then analyzes the actual daily solution in depth, in the context of this chapter and the simulation.

Chapter 4

Testing performance with a simulation

Due to the unique character of GRACE observations, there is no "truth" dataset that is directly comparable to our daily solutions. In the following section, we will make use of TWS model output as an independent dataset for comparing with our final product. Before this analysis, we have first devised a simulation in order to quantify the expected signal recovery of our daily product, discussed here. These two comparisons are unique and complimentary assessments of our daily product, as the simulation results in this section test solution performance against limited known signals while the model comparison in the following section tests continental-scale signal recovery performance against other imperfect estimates of TWS.

Our simulation used a specially designed set of box function signals placed in individual, globally dispersed land mascons with 10-day periodic repeating patterns over a 30-day month defined by

$$y_i(t) = \text{ sgn}\left(\sin\left(\frac{(t-\tau_i)\pi}{5}\right)\right) \text{ (m water equivalent height)}, \tag{4.1}$$

where τ_i is an integer number of days phase shift, unique to each individual mascons containing a simulated signal, and the magnitude of the box function is the mass equivalent of one meter of water over the surface of a single mascon, or about 12.38 Gigatonnes (depicted in Figure 4.1. These functions were added to the reference forward model described in Chapter 3, amounting to a known amount of mis-modeling of the background model. Individually, each simulated signal was zero-mean over the 30-day period, while collectively the sum of all signals on any given day was zero to ensure mass was conserved globally in the simulation.

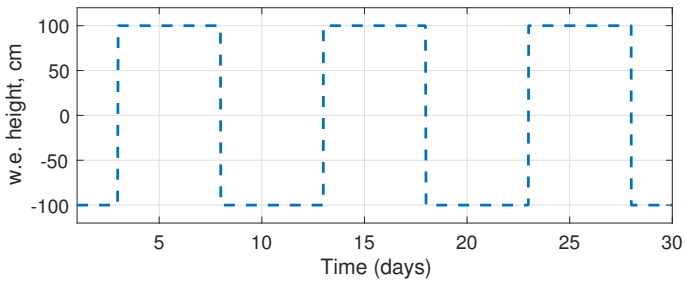

Figure 4.1: Example signal for simulation study from Equation 4.1 for $\tau = 3$

.

After including these signals in the reference model, real GRACE observations from June 2004 were processed using the mascon least squares estimation system. As these signals represent a known mis-modeling of the true state, the resulting estimated state should include a correction to this mis-modeling. In order to separate real recovered sub-monthly signals observed by GRACE from the simulated signal, a second distinct solution was estimated over the same period that excluded the simulated signals from the reference forward model. The difference of these two estimates then provides the estimated correction due to the simulated signal. The spatial extent of these corrections was then analyzed to determine the recovery performance of the estimation system.

4.1 Quantifying simulated signal recovery

The total recovered mass within specified radii of the mis-modeled mascon at seven locations included in the simulation are given in Figure 4.2, along with a key for their location. These locations include low-, mid-, and high-latitude mascons across multiple continents, providing a useful representation of mascon resolution globally. Mass is accumulated from the differenced correction field described above as the total sum of all mascons within each specified radius. Accumulating recovered mass within a 300 km radius, or approximately the spatial resolution of monthly GRACE solutions, the daily fields show low signal recovery at all latitudes. As this radius is increased, the simulated mass is more fully recovered at all locations. High latitude locations such as the East

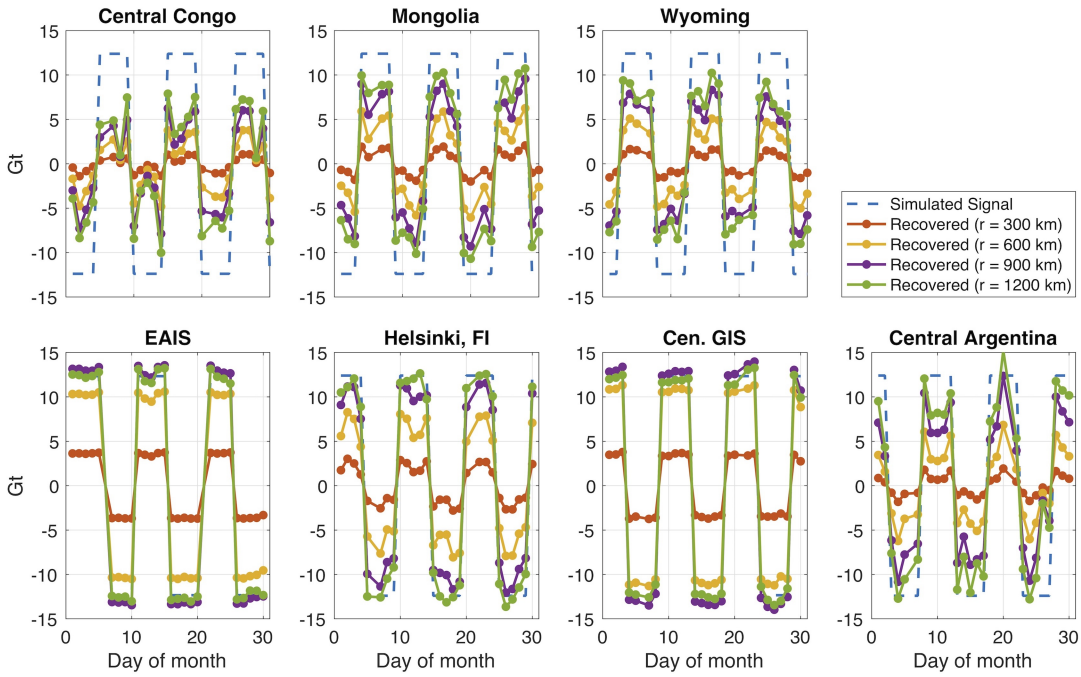

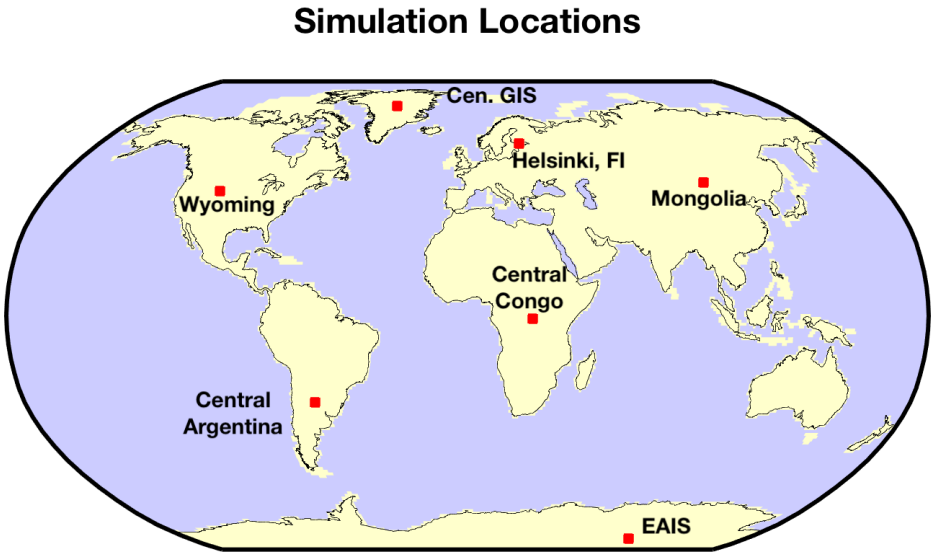

Figure 4.2: Simulated signal recovery at seven locations is presented. Recovered signals are accumulated as the total signal within a given radial distance of the simulated signal center. High-latitude locations (AIS, GIS, and Helsinki) show the best signal recovery and localization, while mid-latitude locations (Mongolia, Wyoming, and Central Argentina show diminished recoverability, and equatorial locations such as the Central Congo show poor recoverability.

Antarctic Ice Shelf (EAIS), Helsinki, FI, and the Greenland Ice Shelf (GIS) show near total signal recovery within a 600 km radius. If this radius is expanded farther, recovery performance is further refined. Mid-latitude locations near 45° latitude such as Mongolia and Wyoming perform worse. At these locations, the total recovered mass within a 900-1200 km radius is worse than for a 600 km radius at high latitude locations. Near-equatorial locations such as the Central Congo show very poor signal recovery even within large averaging radii, suggesting that poor daily coverage greatly diminishes the ability of the system to estimate equatorial TWS.

An interesting example demonstrating the benefits of regional boundary constraints can be seen in the Central Argentina mascon (approximately 30°S), which shows similar recovery performance to Mongolia and Wyoming despite being located closer to the equator. Due to the land/ocean regularization constraint used in this study, leakage in mascons close to coastlines is reduced and recovered signals are better localized. The portion of the South American continent containing this Central Argentina mascon is a relatively narrow land basin as compared to continents containing inland locations in Mongolia and Wyoming. The land/ocean boundary for this Central Argentina mascon is only 10 mascons away in both the east and west directions, whereas the only nearby coastal boundary for either the Mongolia or Wyoming mascons is the Pacific Coast boundary in the Western US, 14 mascons to the west of the Wyoming mascon. This better-than-expected signal recovery based solely on latitude in Central Argentina helps demonstrate the benefits of regional constraints in helping localize signal and improve the resolution of the estimated solution.

It should be noted that multiple iterations of this simulation were investigated. In these iterations, variables not presented in detail here were investigated, such as the temporal shapes of the simulated signals and the effects of placing a signal directly on a coastline. To briefly summarize the findings from those tests, signal shape was determined to have no effect on the signal recovery for any given day, but did reinforce that short term signals may be entirely unrecoverable if the day(s) in which those signals are present in TWS are not well observed by GRACE. Similarly, a coastal location had the same effect as a signal in a narrower continent (such as Central Argentina) but to a more pronounced degree due to regional constraints further helping to isolate signal. Both

findings are natural extensions of the more detailed results shown, and therefore not considered at length here.

4.2 Spatial recovery of the simulated signal

To better understand day-to-day variations in signal recovery, spatial maps of recovered signal are considered in Figures 4.3 and 4.4 for the East Antarctic Ice Sheet (EAIS) and Wyoming, with orbit groundtracks shown. Daily observability varies with orbital geometry, explaining daily variability in the recovered estimates in Figure 4.2. This effect is most noticeable for Wyoming, while recovery in the EAIS shows little variability in spatial recovery, suggesting that orbital observability is less of a factor at high latitudes. This is expected, as the GRACE polar orbit provides excellent coverage at high latitudes compared to low- and mid-latitudes.

To better understand leakage of the signal over Wyoming, the general spatial structure of the signal was considered. Figure 4.5 shows a breakdown of the dominating spatial pattern in daily signal recovery. The RMS of the magnitude of the recovered signal at every mascon in North America was computed and is shown. These RMS values were then analyzed versus the distance of each mascon to the simulated signal center. Signal falls off with distance in a manner similar to the Gaussian smoothing function, a function often used to describe resolution of GRACE spherical harmonic studies (*Wahr et al.*, 1998). This function will be considered further in the next chapter as part of an analysis of the real daily signals, and therefore is mentioned here only as an interesting note. The figure also shows that the rate at which these values fall off with distance is also dependent on the orientation of the mascons to the original signal. Mascons north or south of the central point (those that share a similar longitude λ) show more a steeper decline in leakage from the original signal, while mascons east or west of the point (along the said latitude, ϕ) show larger leakage extent. This can be attributed to the unbalanced observability of GRACE measurements, particularly on daily timescales. At mid latitudes, the GRACE orbit is oriented roughly north-south, and a larger number of along-track observations are able to localize north-south variations in the gravity field well. On the other hand, large gaps in observations east-west

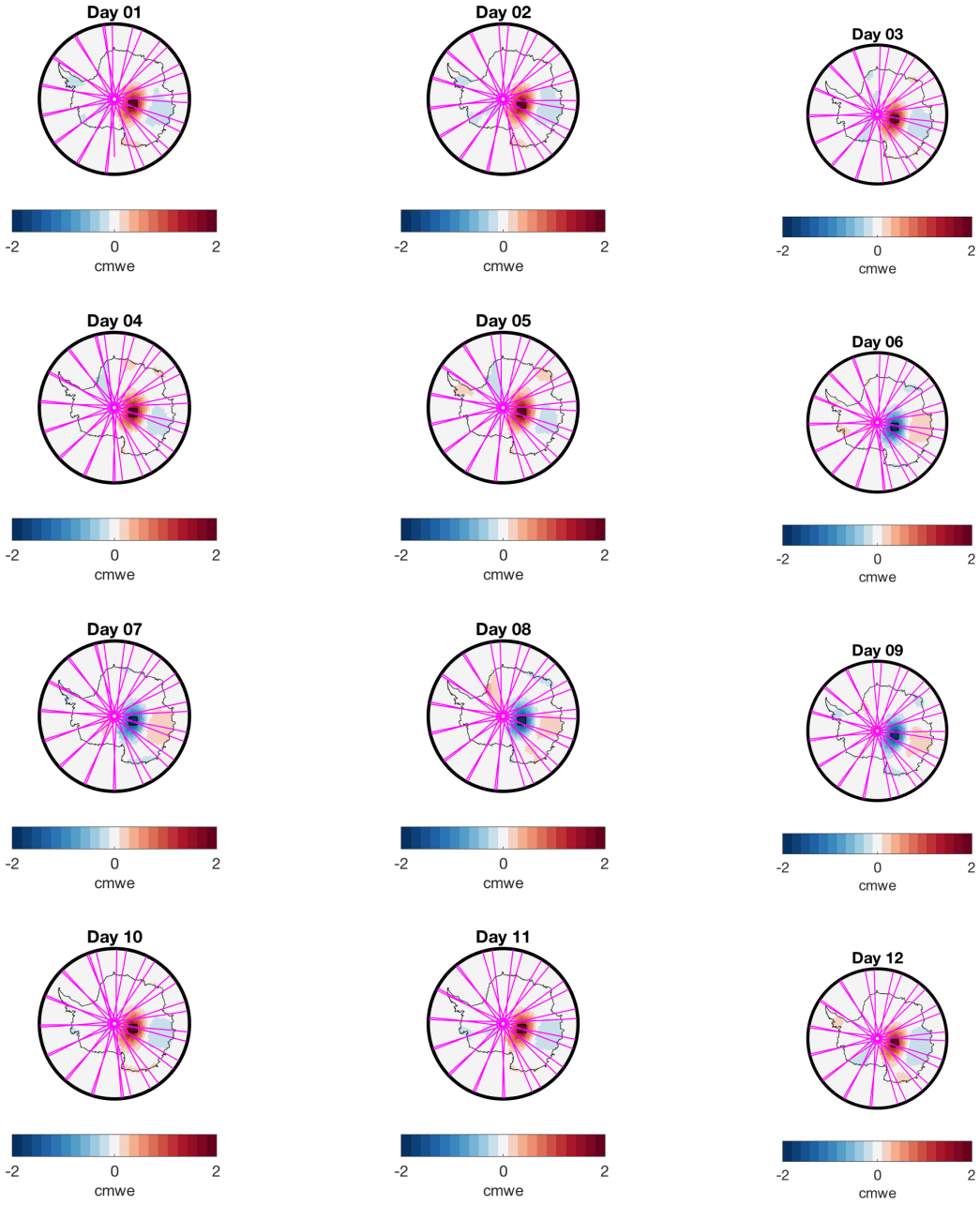

Figure 4.3: Spatial recovery of simulated signal over the East Antarctica. Total signal recovery shows a clear dependence on orbit location (pink) for each day, explaining variability in total recovery shown in Figure 4.2.

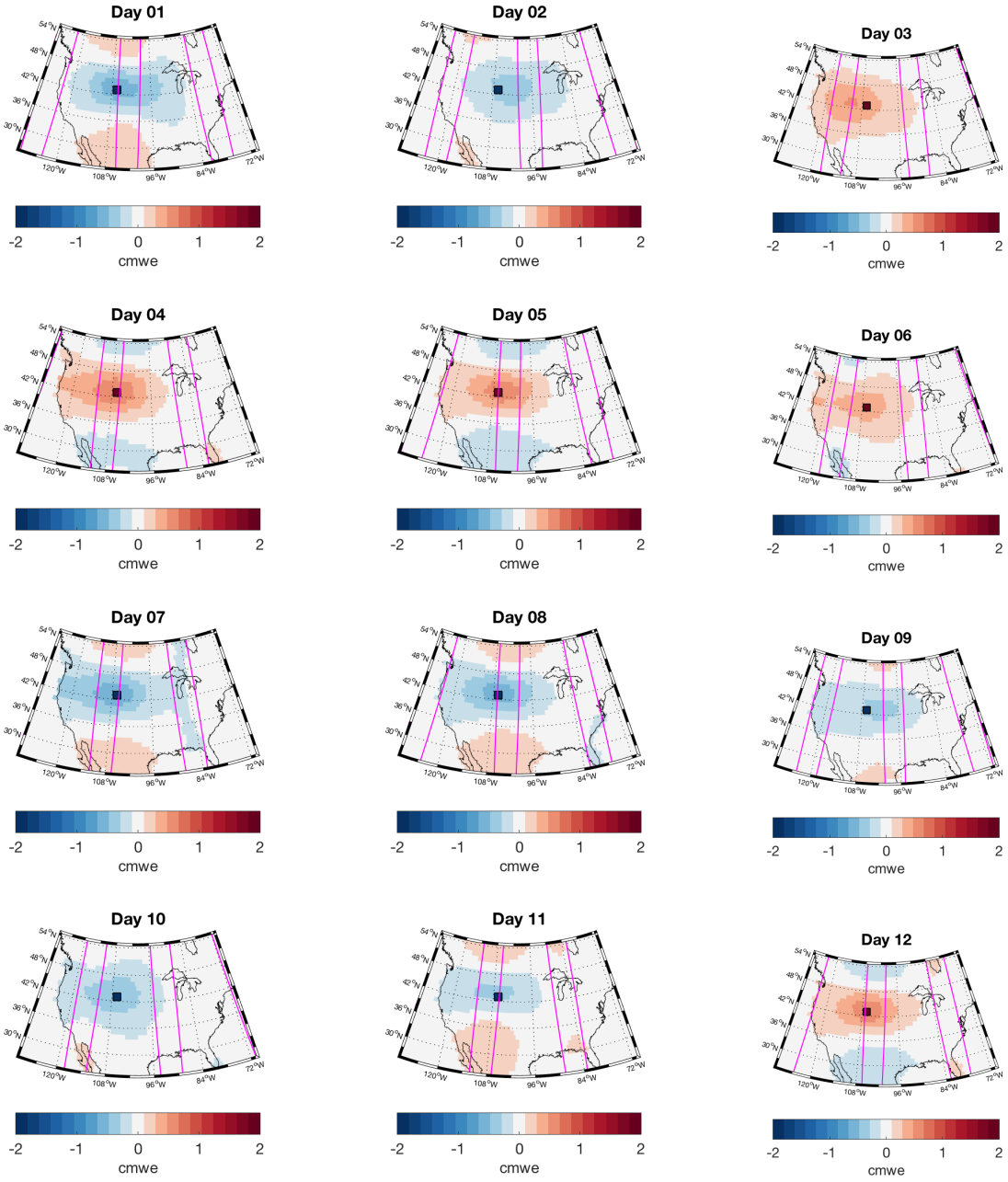

Figure 4.4: Spatial recovery of simulated signal over Wyoming. Total signal recovery shows a clear dependence on orbit location (pink) for each day, explaining variability in total recovery shown in Figure 4.2.

create a spatial ambiguity problem, where the recovered signal could be the result of smaller nearby signals or larger signals to either side. As a result, the east-west spatial recoverability with daily GRACE solutions underperforms north-south measurements, resulting in the patterns shown.

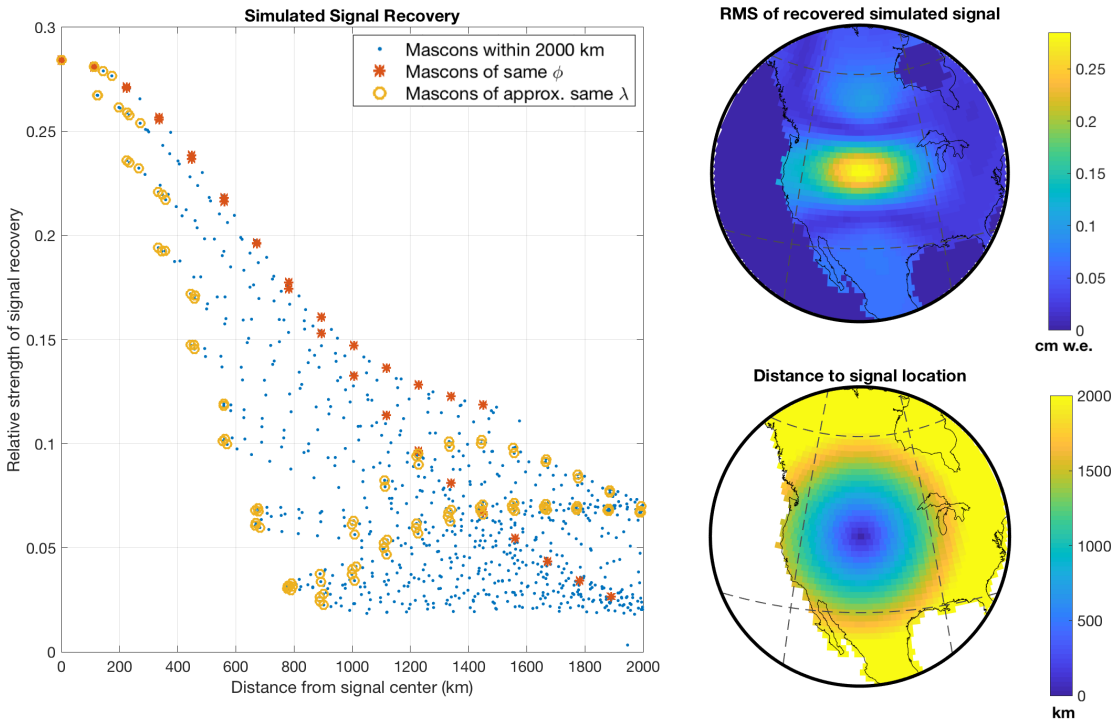

Figure 4.5: Leakage outward away from the simulated signal in Wyoming: The RMS of recovered signal at every mascon is plotted against the distance of each mascon to the original signal (left) and mapped spatially (top-right). This pattern falls off with the distance of each mascon to the signal center (bottom-right).

4.3 Summary of key simulation findings

This chapter used a simulation study to test signal recovery in land locations spatially distributed around the globe using the developed daily mascon solution presented in this dissertation. This study demonstrated that signal recoverability is dependent on latitude, where high latitude locations that are better observed by GRACE show more complete and more localized signal re-

covery.

Locations in Greenland and Antarctica, polar basins that are additionally constrained as independent basins in the solution regularization, show the greatest ability to recover signal, while other high latitude locations such as Helsinki, Finland show slightly degraded performance in comparison. This can be attributed to leakage of the simulated signal away from Helsinki into Europe and Asia due to the lack of a regional boundary in this area helping to isolate the recovered signal spatially. Mid-latitude signals such as in Wyoming and Mongolia showed further degraded performance, and their relative isolation from regional boundary constraints was shown to allow significant signal leakage away from these locations. On the contrary, a signal in Argentina was shown to be better localized despite a lower latitude, attributed to the relative proximity of both the Pacific and Atlantic coastal boundaries in this narrower continent.

As a whole, the simulation provides a "rule of thumb" of sorts, that signal leakage in high latitude locations is nearly entirely within 600 km, while at lower latitudes this leakage can extend outward to 1000 km or more. With that in mind, it would be advantageous to develop a more thorough measure of this leakage, which biases signal recovery. In the next section, which analyses actual daily signals, a method for better determining signal resolution and recovery bias is presented and applied in a model-based comparison of TWS. The rule of thumb developed in this section will be considered in comparison to these results, and used to validate the developed analysis technique.

Chapter 5

Analysis of developed daily solution

The simulation study presented in the previous section is informative because it helps to establish expectations for daily solution performance. In this section, we analyze the actual daily solution in light of results from the simulation. We present a global measure of leakage between mascons in the daily solution, which we refer to as the solution bias. A basin-scale analysis is then presented with comparisons to model estimates of TWS, so that daily solution performance can be further quantified.

The total time-variable signal content of our developed solution is a combination of the high spatial resolution and long-term information from the fully converged monthly GSFC solution in our reference background model and lower spatial resolution daily information in our daily estimate. A necessary but not sufficient condition of our estimate is therefore that the monthly average of the total daily solution is approximately equal to the GSFC converged monthly solution, with any variations from that due to the differing spatial scales of the two solution layers. Figure 5.1 compares the monthly GSFC solution for April 2012 with the corresponding monthly-averaged daily solution and shows strong agreement between the monthly resolutions of each solution. Differences between the two fields are less than 5% of the total signal and due to the different spatial resolutions of the daily and monthly solutions. Therefore, we can affirm that the estimated daily solution adds only sub-monthly information to the converged monthly solution.

Daily signal content globally can be compared to the GSFC monthly solution by computing the RMS of both solutions over a similar time period and comparing their the magnitude and shape.

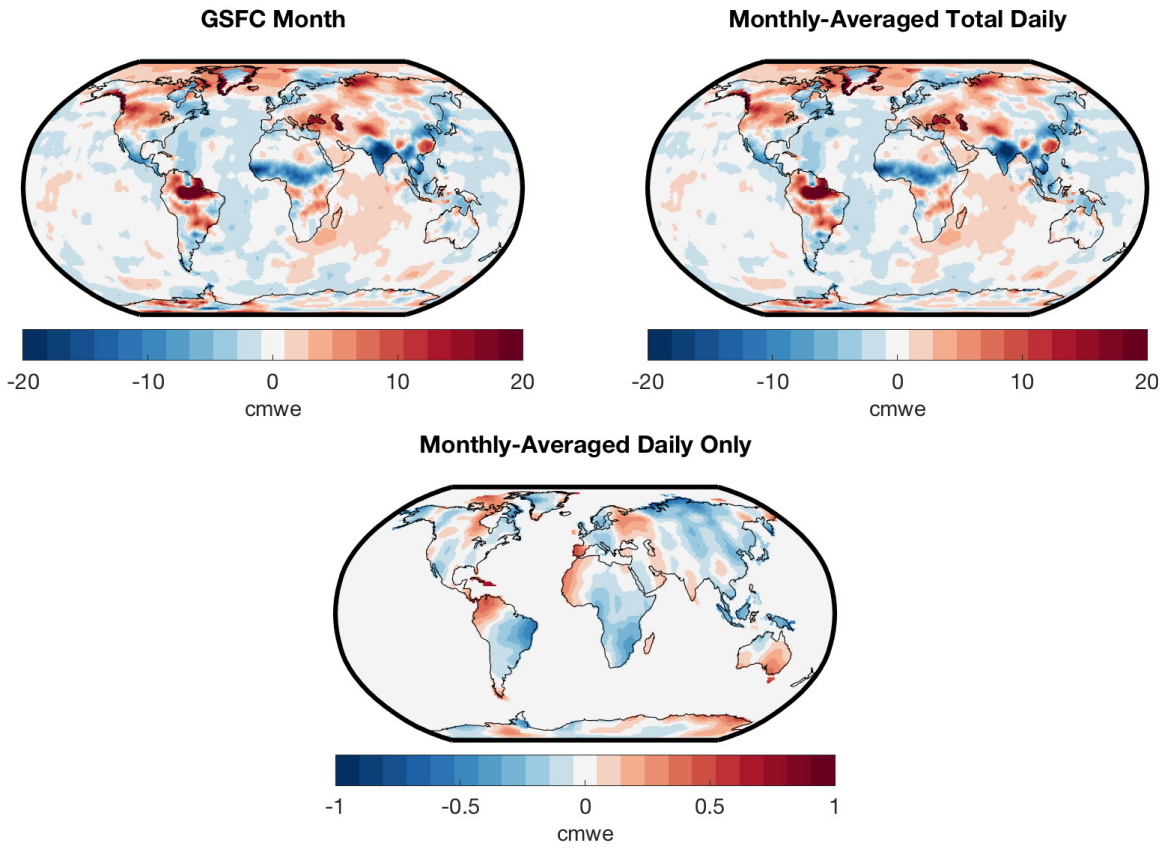

Figure 5.1: April 2012 solution content: GSFC converged solution (top-left), monthly-averaged total daily estimates with monthly reference model restored (top-right), and monthly-averaged daily estimates (bottom).

Figure 5.2 shows maps of the RMS of the daily and monthly signals for 2012 (269 days or 9 months). This measure is useful because it gives an idea of the spatial variability of the two solutions. An immediate comparison between the daily and monthly RMS maps shows that large-scale spatial patterns are consistent between the two solutions, which should be expected because monthly mass variability is driven by long-term effects of daily variability. The magnitudes of the monthly RMS map are larger in magnitude than for the daily solution. However, this is to be expected, as monthly changes in TWS are in fact accumulated daily changes. The maps show consistency in signal content in hydrologically active regions such as the Amazon, sub-Saharan Africa, India and Southeast

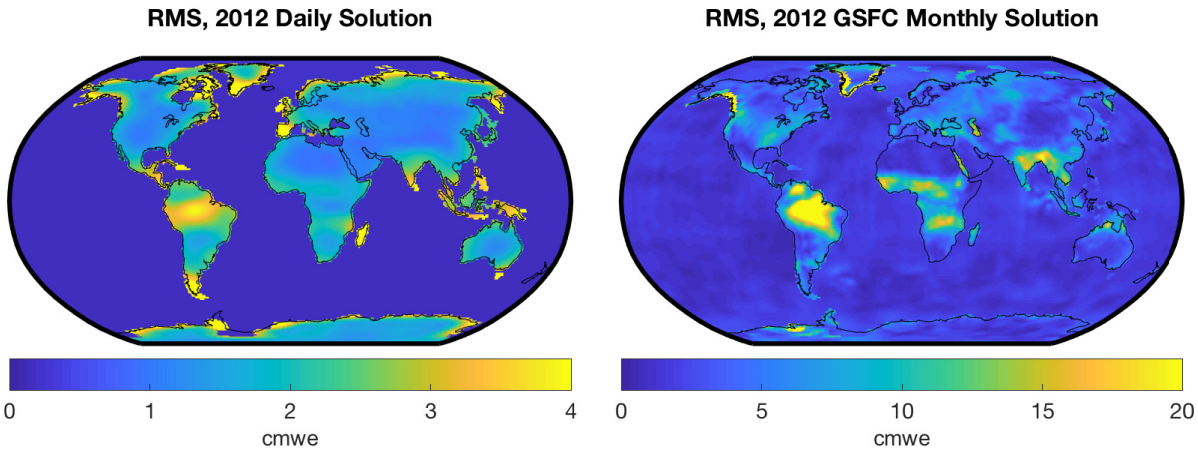

Figure 5.2: Maps of the RMS of the estimated daily solution as compared to the GSFC monthly solution for 2012, showing strong similarities in large-scale spatial patterns and highlighting differences in spatial content scales.

Asia, and the Gulf of Alaska, as well as glacial regions such as Greenland and coastal Antarctica. Differences between the two maps also highlight some of the more challenging aspects of designing a daily product, where narrow or relatively isolated regions and lower latitude regions such as Central America, the South Pacific islands, or Madagascar show larger-than-expected signal content in the daily solution, indicating likely observability issues where some days are more observable than others. Finally, the map very clearly shows the differences in spatial resolution that can be expected between the daily and monthly solutions. With far fewer observations and only 15 evenly spaced orbital tracks separated by approximately 24° in longitude, shorter-wavelength signals are simply not as recoverable as with monthly observations.

The usefulness of daily solutions can in part be demonstrated by investigating mass estimates at basin scales. We compute estimates for each basin i from the subset of N mascons in each basin, $\overline{m}_i(t) = [m_1, m_2, ..., m_N]$, by

$$B_i(\overline{m}_i(t)) = \frac{\sum_{j=1}^{N} a_j \; m_j(t)}{\sum_{j=1}^{N} a_j}, \tag{5.1}$$

where a_j is the area of the j^{th} mascon. Figure 5.3 shows the total daily signal and the daily

component of the signal for the combined Arkansas-White-Red basin, demonstrating that distinct sub-monthly signals are recovered by the daily solution.

From here, because monthly and long-term information in the total daily solution is determined *a priori*, this analysis focuses only on the estimated daily variations relative to the monthly solution. All figures and statistics presented in the remainder of this analysis relate to only these estimated daily variations except where otherwise explicitly stated. These estimates are investigated in greater detail as part of an analysis of multiple basins in North America compared to model output from NLDAS later in this section.

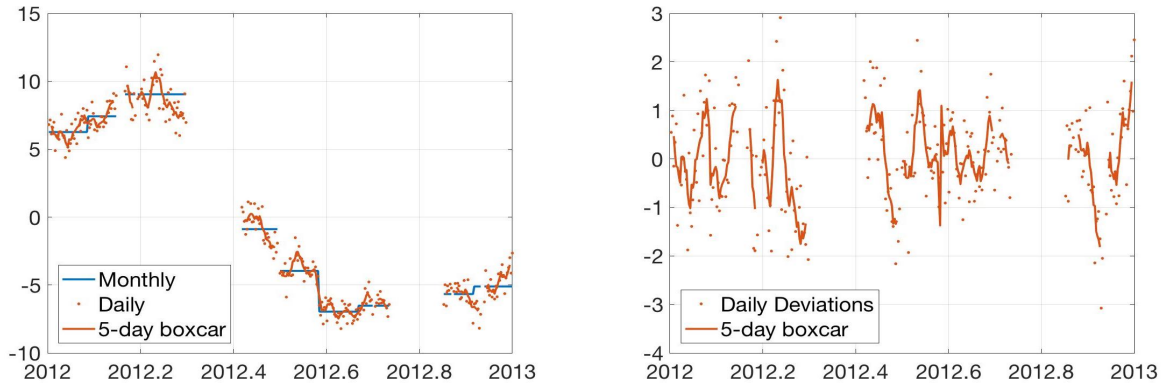

Figure 5.3: Estimated total daily signal (left) and daily deviations (right) for the combined Arkansas-White-Red basin. Daily deviations are the total signal with the GSFC monthly fields removed. A simple 5-day boxcar filter is applied to help show estimated signal structure.

5.1 Quantifying solution bias with the resolution operator

In Section 2.6.2, the resolution operator was defined as a way to transform a truth state to the regularized form of that state given the chosen estimation regularization scheme. Applying this concept to the daily mascons, the resolution operator can be used to determine how each mascon is recovered spatially. The spatial patterns of the resolution operator columns characterize the

spatial information of the daily estimate. Each column quantifies the distribution of signal leakage from a single mascon into each of the other 41,168 mascons due to the imposed regularization constraints as well as the geometry of each day's orbit observations. Figure 5.4 a) and b) depicts the spatial dispersion of a true signal over a single mascon in central North America as expressed in the corresponding column of the resolution operator. This is equivalent to computing to computing an impulse response $\hat{\mathbf{x}} = \mathbf{R}\mathbf{x}$, where $\mathbf{x}$ is an impulse function with value 1 over the single mascon and zero elsewhere. The impulse response describes the spatial extent of bias in the recovery of the original impulse. From our chosen regularization, the computed response is most dependent on relative distances between mascons and proximity to regional boundaries (such as coastlines). Orbit observations each day then contribute to the total spatial extent of this distribution, scaling this response function based on each mascon's proximity to a given day's GRACE observations. Mascons closest to the daily orbit show more confined leakage, while greater leakage extent is seen for more poorly observed mascons.

In GRACE spherical harmonic studies, Gaussian smoothing is commonly used as a post-processing technique to smooth data and reduce correlated errors due to striping and other effects, and an Gaussian smoothing radius r for such smoothing is defined as the distance where the

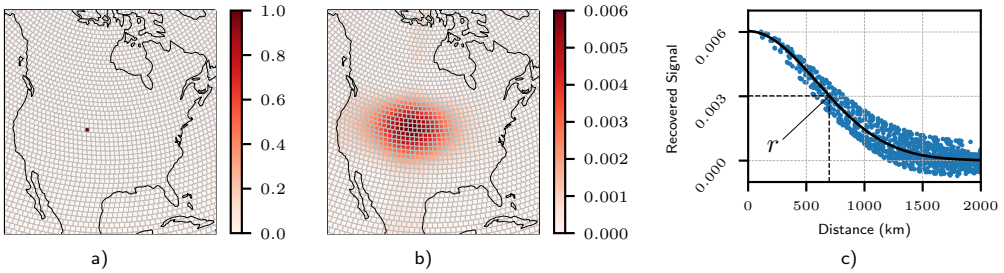

Figure 5.4: Leakage as represented by the resolution operator: a) Impulse function as a truth signal over a single mascon, b) recovered truth signal in a geographically dispersed area centered about that mascon as response to impulse response, c) The recovered signal as a function of distance to the original signal and a Gaussian smoothing radius best describing this distribution.

magnitude of the smoothing function has dropped to half of its central value *Wahr et al.* (1998); *Swenson and Wahr* (2006). This radius in then often used to describe the resolution of the smoothed GRACE solution. By considering the distribution of the recovered mascon signal strength in Figure 5.4 b) with respect to distance from the central mascon, we can similarly quantify the spatial distribution of recovered mass due to the resolution operator. Figure 5.4 c) gives these recovered signal magnitudes with respect to distance from the original central mascon. The plotted distribution of recovered magnitudes falls off with distance like a Gaussian smoothing function, and a function fitting this distribution can be determined. From this function, a comparable Gaussian smoothing radius r for the mascon solution at each mascon is calculated, as depicted in the figure for the example mascon.

By computing the Gaussian smoothing radius for every land mascon from each specific day's resolution operator, we develop a map of mascon spatial resolution for each day. Figure 5.5 shows daily maps of this resolution for four consecutive days in North America and Antarctica. Orbit tracks are depicted in red, highlighting areas with better observability. Due to differences in spatial sampling, higher latitudes show much better spatial resolution and lower dependence on daily variations in GRACE tracks, while lower latitudes show poorer spatial resolution in general and significantly poorer resolution in the least observed areas each day. Over North America, tracks of low visibility can be seen migrating across the continent as the daily orbits shift in coverage each day, while much lower dependence on orbit track location is seen in Antarctica. Well-observed, high-latitude mascons such as in Antarctica, Greenland, and Northern Canada show spatial daily spatial resolutions of 400 km or better, while even the best observed mascons at mid-range latitudes show significantly lower resolutions of 600-800 km.

In the next section, the resolution operator is applied to comparisons with model outputs of TWS. These comparisons make use of a mean daily resolution operator computed from 30 individual daily resolution operators due to computational and storage limitations for this comparison. This mean resolution operator is presented in Figure 5.6, where a) and b) show an example daily resolution map for North America and Antarctica and c) and d) show maps of the mean resolution

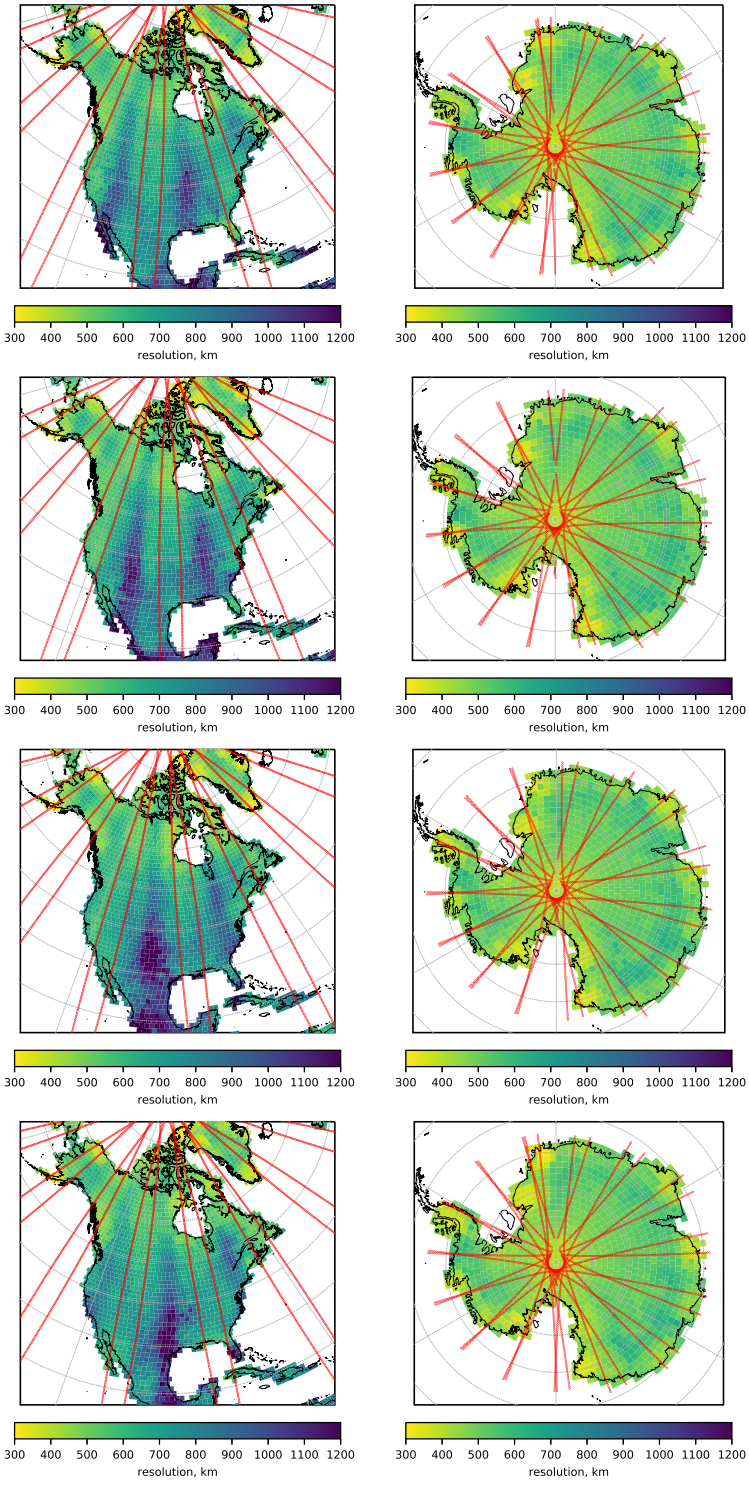

Figure 5.5: Daily maps of resolution for June 1-4, 2004 (top to bottom) in North America and Antarctica. Resolution is defined as the computed Gaussian smoothing radius describing each mascon's bias characteristics. Red lines show the GRACE orbit that day.

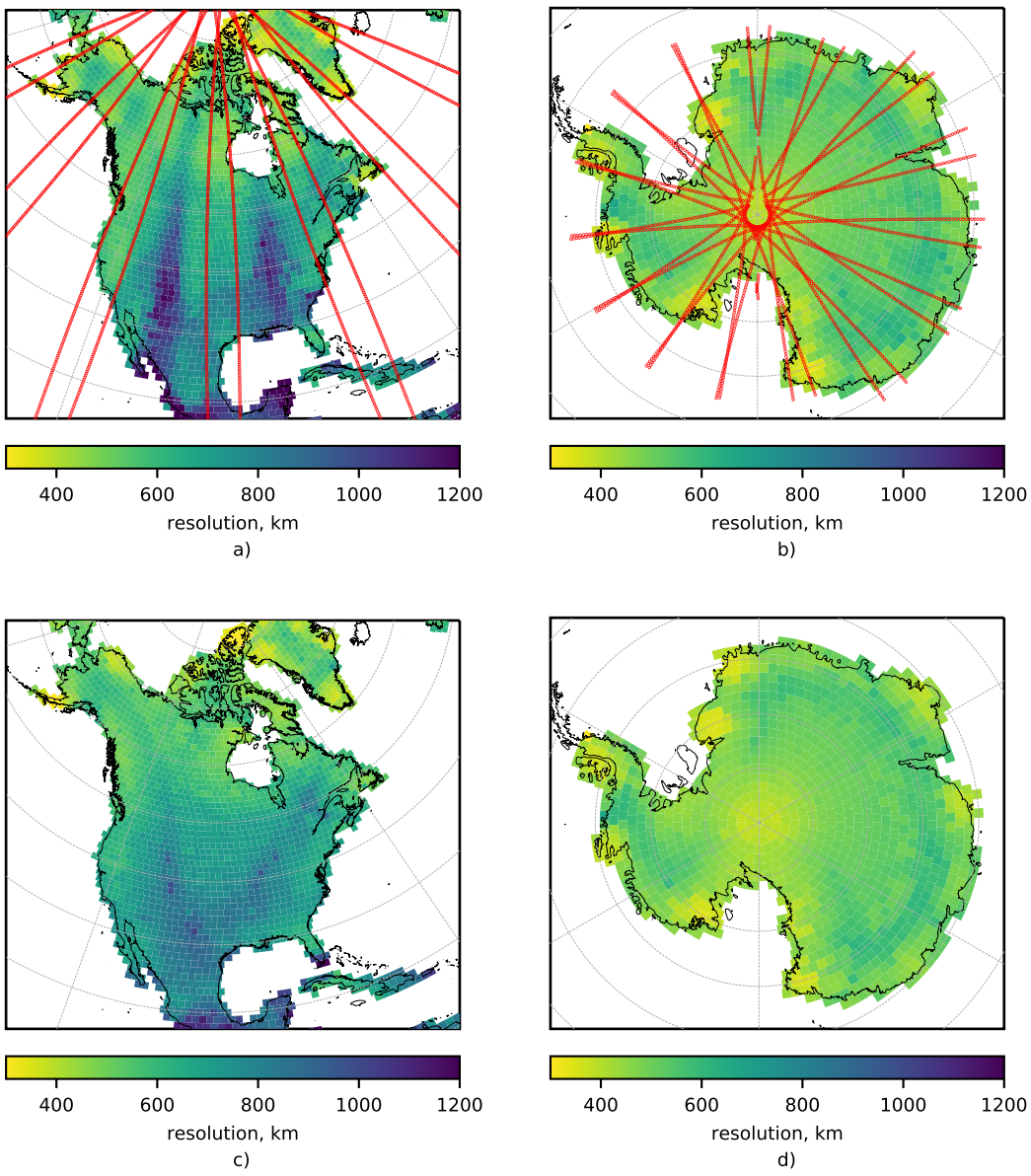

Figure 5.6: a) and b): Daily maps of resolution for June 2, 2004 in North America and Antarctica. Resolution is defined as the computed Gaussian smoothing radius describing each mascon's bias characteristics. Red lines show the GRACE orbit that day. c) and d) Maps of mean resolution from 30 daily estimates for June 2004.

operator. Computing the mean resolution operator effectively removes the orbital track information from the resolution operator, but maintains the primary regularization components in the operator. Future applications where the individual daily resolution operators are required will require upgrades to computational and storage capacities available for to solution, but are otherwise possible.

As a latitude dependence was built into the regularization matrix and is suggested by the Gaussian smoothing radius resolution maps from the resolution operator, it is informative to consider and attempt to quantify this effect. From the resolution map for the mean resolution operator in Figure 5.6, each estimated Gaussian radius is plotted with respect to mascon latitude, in Figure 5.7. While there is significant scatter in the signal, a distinct latitude dependence is obvious. This dependence can be modeled as

$$\hat{r}(\phi) = A + B\cos\phi, \tag{5.2}$$

where the model resolution $\hat{r}(\phi)$ is the best fit resolution at Latitude ϕ, A is the best fit resolution at the poles, and $A + B$ is the best fit resolution at the equator. The best fit polar resolution is then $\hat{r}(\phi = \pm 90^\circ) = 385$ km, and the best fit equatorial resolution is $\hat{r}(\phi = 0^\circ) = 836$ km.

The resolution map can then be investigated further by removing the best fit of the latitude dependence from the Gaussian smoothing resolution estimate for each mascon, and mapping the residual resolution values. Figure 5.8 shows the effect of this operation over North and South America. When a best fit latitudinal dependence is removed, a clear pattern emerges as a function of proximity to the coast. Mascons closest to the coast show smaller and therefore better resolution and inland locations show larger and therefore worse resolution. This can be directly attributed to the regional constraints built into the regularization matrix, which imposes the condition that mascons closer to regional boundaries see better resolution due to reductions in leakage across those boundaries. The figure depicts a "maximum Gaussian smoothing radius" boundary of sorts inland from the coast. Upon inspection, this maximum occurs at approximately 1000 km from the coast, which suggests that inland mascons greater than 1000 km from the nearest regional

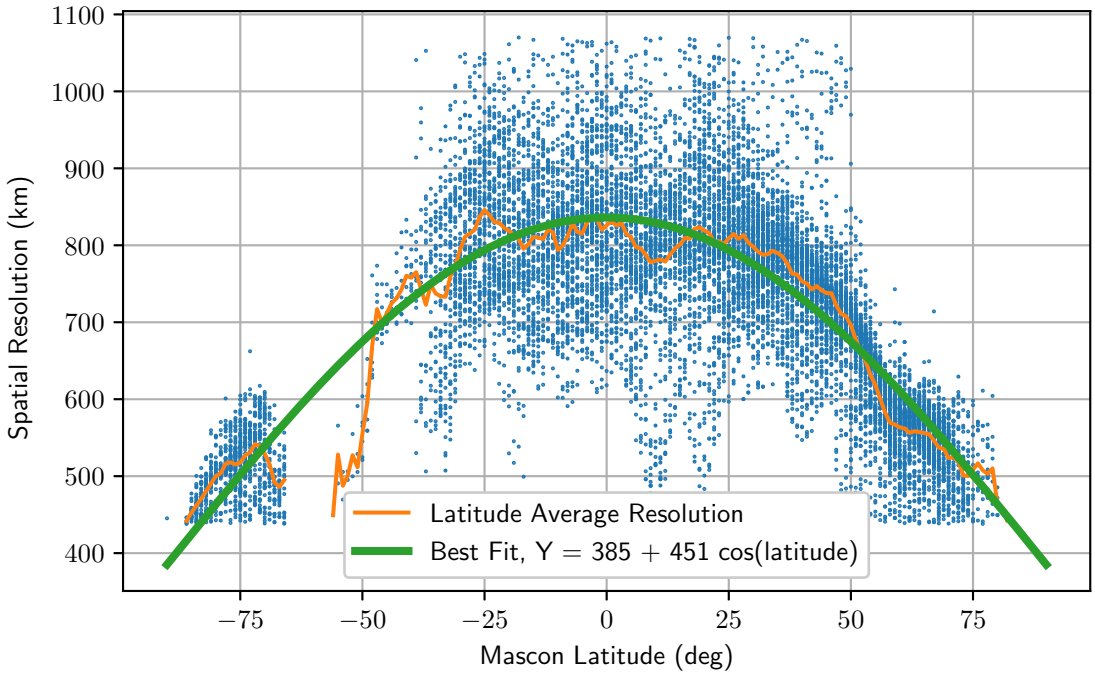

Figure 5.7: Mascon resolution as estimated by the Gaussian smoothing radius vs. Latitude. A clear Latitudinal dependence exists for all latitudes, and can be modeled by a function $\hat{r} = A + B\cos\phi$. Parameter A then represent the average the best fit resolution at the poles and $A + B$ represents the best fit resolution at the equator.

boundary are essentially not affected by those constraints, while mascons within 1000 km of the coast are impacted by those constraints. The maximum (and therefore lowest resolution) mascons occur right near this boundary, where regional constraints lose their effectiveness but still slightly impact the bias in those mascons.

It should be stressed that these latitudinal and boundary effects on solution resolution are expected, but difficult to quantify independently in the regularization scheme itself. By investigating the spatial patterns observed in the resolution operator, these effects can be better quantified. It should also be pointed out that regional boundary geometries further complicate the effects of

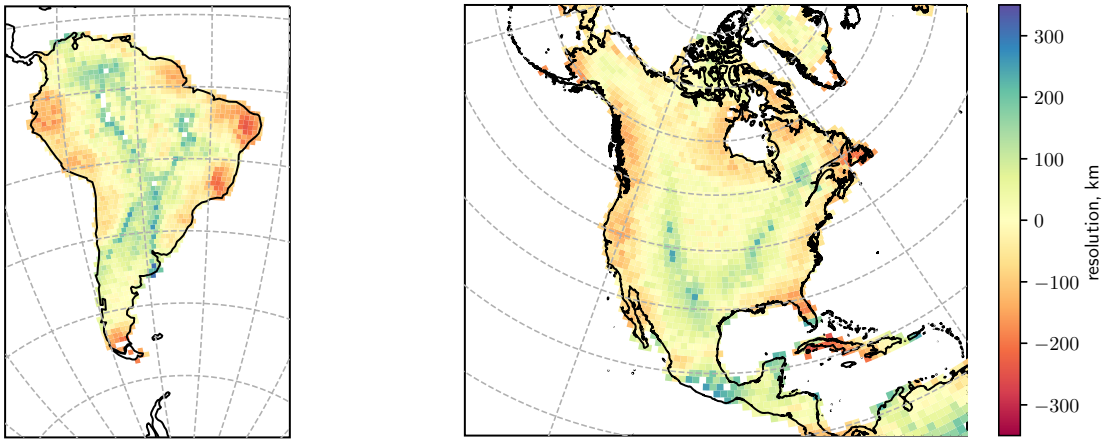

Figure 5.8: Maps of Gaussian smoothing derived resolution where latitudinal effects on resolution from Equation 5.2 have been removed (fit outliers have been masked). Residual signal is dominated by coastal effects due to the inclusion of regional constraints in the least squares regularization.

regional constraints on solution resolution, as can be seen to a lesser extent in Figure 5.8 along narrower land masses and areas with irregular boundaries. These can be considered local effects that further influence mascon resolution.

The developed resolution maps can be related back to the simulation presented in Chapter 4. In the simulation, high-latitude mascons were shown to be nearly fully recoverable within approximately 600 km of the mascon, while mid-latitude mascons were were only mostly recoverable within 900 km or more. By comparison, the Gaussian smoothing radius used in this section quantifies a distance where most but not all signal will be recovered. In fact, the area under a Gaussian smoothing function from 0 to r is approximately 75% of the total area under the function for all r in the 300-1200 km range determined here. With this in mind, a simulation recovery radius of 600 km corresponds with $r \approx 450$ km while a recovery radius of 900 km corresponds with $r \approx 675$ km, indicating that our simulation findings validate our use of the resolution operator to quantify

bias in our daily solution. Applying the resolution operator to compute an impulse response function for each location in the simulation, the recovered simulated signal can be compared to expected recovery with the resolution operator. Figure 5.9 plots the 900 km radius mass estimates from Chapter 4 and compares them to an impulse response from applying the resolution operator. The figure shows recovered impulse responses within the same 900 km radius for two tests: one where individual daily operators are applied each day, and one where the mean resolution operator over the month is applied to all days. Recovered impulse from both methods compare well, with the individual daily operator plots showing slightly more daily variation in signal recovery. Both estimates match the simulation results well, with both showing slightly better signal recovery for most locations than the simulation. At high latitude locations, little difference is observed between

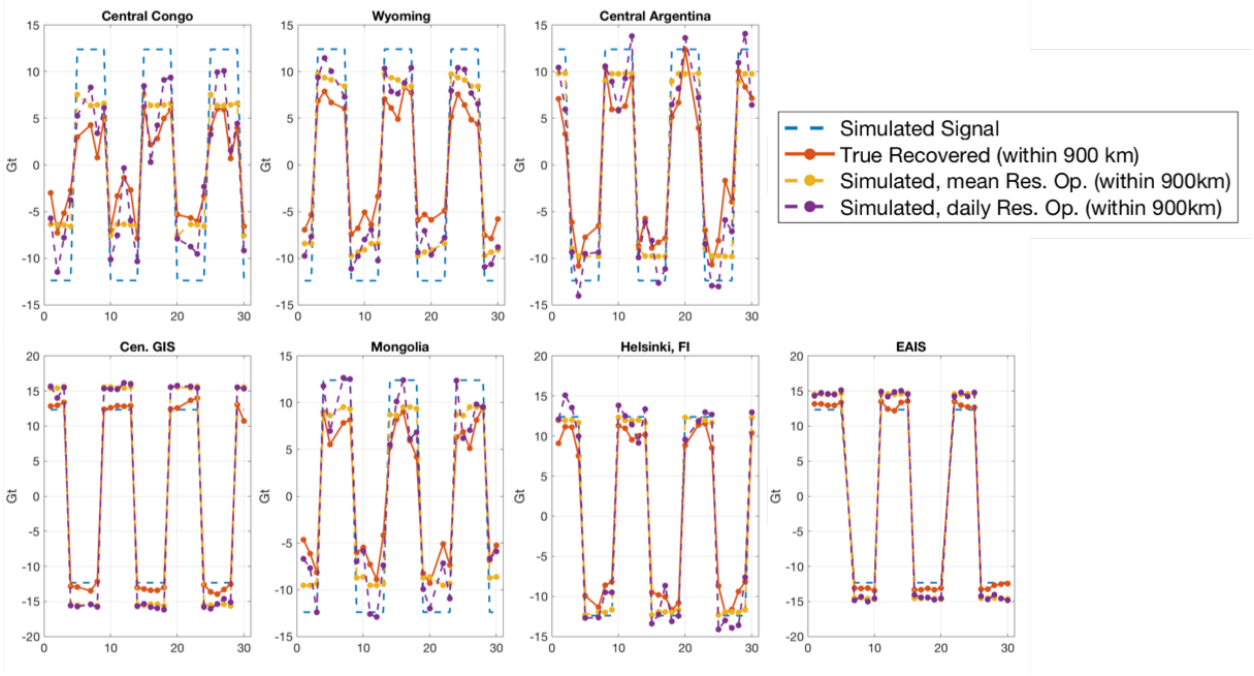

Figure 5.9: Recovered signal from the simulation in Chapter 4 at a radius of 900km versus mass estimates from an impulse response determined from individual daily resolution operators and a mean resolution operator.

use of the mean or daily resolution operators, reaffirming the finding that high latitude locations show only small orbit-based effects on recovered signal resolution. This is due to the assumption that the resolution operator maps bias assuming perfect observations, while the simulation included real GRACE observations and therefore imperfect observations.

5.2 Comparisons with Model Estimates of Terrestrial Water Storage

We compare our daily mascons with two models of TWS, VIC 4.0.3 and Noah 2.8, from Phase 2 of NLDAS(*Xia et al.*, 2012), analyzing daily recovered mass estimates over river basins in the continental United States for 2012. No TWS model is perfect, and the VIC and Noah models realize the water cycle with different assumptions and model parameters, leading to differences in estimates of TWS between the two models. As NLDAS products, these models are realized in functionally similar forms to the end user, estimating their various model parameters onto the same grids and at the same temporal resolution. We include comparisons with both models because it is not obvious which model best represents true TWS, and differences in the two models will help prevent errors in a single model from overly biasing the results of our comparison. Estimates of TWS are computed for both models by accumulating NLDAS output fields for multi-layer soil moisture content, water equivalent snow depth, and total canopy water storage. As neither model includes groundwater estimates or information for major inland water bodies such as the Great Lakes, these TWS contributions are not accounted for in the model basin estimates. Both NLDAS outputs are distributed as hourly 0.125° gridded datasets over North America. Each is averaged in space and time to properly match GRACE resolution.

For each NLDAS output, daily mascon averages of TWS are computed from the hourly gridded data binned into 1,002 land mascons over North America. At this resolution, these mascon-averaged outputs are not directly comparable with the daily GRACE product, as they do not share the same bias characteristics as the GRACE solution. To properly account for this, the mean daily

resolution operator is applied to the daily mascon-averaged VIC and Noah fields, transforming the NLDAS mascon fields into fields that now reflect the same regularization as the GRACE solution, effectively introducing bias in the GRACE estimate into the NLDAS outputs. This operation follows Equation 2.74. This transformation from the original NLDAS resolution to mascon space with bias is illustrated in Figure 5.10 and summarized in Table 5.1. The top row illustrates the effects on spatial resolution of these operations, while the bottom plots show the effects on the recovered mass estimates for two example basins. As basin size decreases, the total recovered signal increasingly differs from the true signal due to leakage both in and out of the basin.

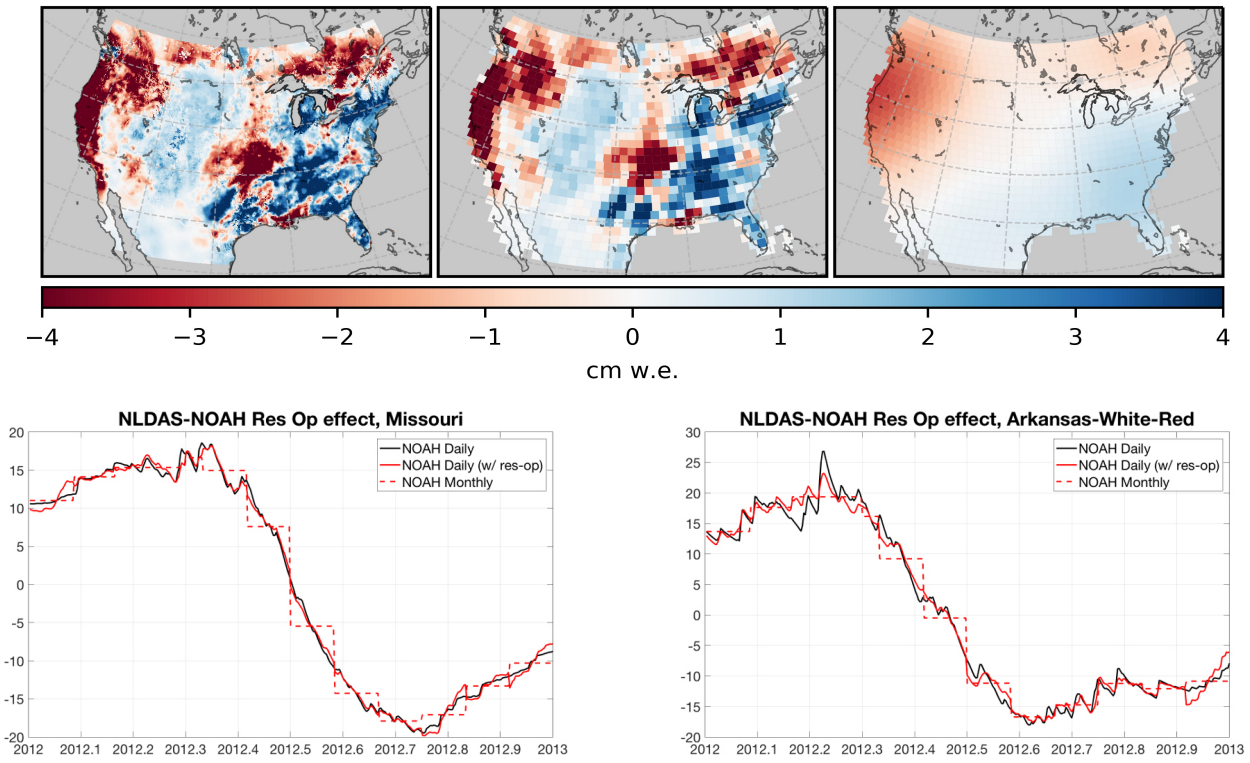

Figure 5.10: Top: Example daily NLDAS-Noah maps of TWS with monthly mean removed: native 0.125° gridded resolution (left), mascon-averaged space (center), and mascon space with mean resolution operator applied (right). Bottom: True basin mass compared to basin mass with resolution operator applied in two basins, Missouri (1,313,551 km^2) and Arkansas-White-Red (644,132 km^2).

Table 5.1: Overview of NLDAS model output processing

	Data	Dimensions	Size	Processing applied
1	Hourly 0.125° grids	[time × ϕ × λ]	[8784, 224, 464]	Compute daily mean fields
2	Daily 0.125° grids	[time × ϕ × λ]	[366, 224, 464]	Mascon-average grids
3	Daily mascons	[time × N *mascons*]	[366, 1002]	Filter days without GRACE
4	Daily mascons	[time × N *mascons*]	[269, 1002]	Apply mean res. operator
5	Daily mascons w/ $\mathbf{R}$	[time × N *mascons*]	[269, 1002]	

NLDAS-derived estimates of TWS with the resolution operator applied are compared with the developed daily solution for the 269 days with useful GRACE observation data in 2012 over 15 hydrologic basins in North America, as defined by the U.S. Geological Survey's (USGS) Hydrologic Unit Maps (*Seaber et al.*, 1987). These basins are shown in Figure 5.11. As NLDAS does not include any information for inland seas and lakes, the Great Lakes/St. Lawrence basin was not included in this comparison. In addition, certain basins near the top and bottom of the NLDAS coverage area where we do not have information about bias from signal beyond the coverage area were also excluded. Figure 5.12 compares the daily mascon estimates for 12 of these basins with the VIC and Noah outputs. Basins are ordered from largest to smallest, the majority of basins show good agreement between the models and GRACE, with this agreement breaking down significantly in the smallest basins. In addition, example maps for six consecutive days in June 2012 are compared for GRACE and both models in Figures 5.13 and 5.14, showing comparable signals spatially during this period. The figures also illustrate spatial limits resulting from solution regularization, comparing to both NLDAS models with and without the resolution operator applied.

Figure 5.11: North American hydrologic basin boundaries from the USGS Hydrologic Unit Maps. Source: *https://water.usgs.gov/wsc/map_index.html.*

Bias in the GRACE solution is approximated by quantifying bias in the NLDAS basin estimates. NLDAS-derived basin bias is approximated by computing the bias for each mascon in the global set of mascon-averaged NLDAS cells $\mathbf{x}(t)$ using Equation 2.77,

$$l(t) = (I - \mathbf{R})\mathbf{x}(t) \tag{5.3}$$

and accumulating total bias for each basin i at every time from the subset $\tilde{l}_i(t) = [l_1, l_2, ..., l_N]$ of N mascons in basin i as in Equation 5.1 by

$$L_i\left(\tilde{l}_i(t)\right) = \frac{\sum_{j=1}^{N} a_j \; l_j(t)}{\sum_{j=1}^{N} a_j}. \tag{5.4}$$

By computing the standard deviation σ_{L_i} of each basin bias estimate, a measure of the bias for each basin is determined. We then relate the ratio of the standard deviation σ_{B_i} of the basin signal B_i (from Equation 5.1) to σ_{L_i} as

$$\hat{r}_i = \frac{\sigma_{B_i}}{\sigma_{L_i}}, \tag{5.5}$$

where $\hat{r}_i$ is then a measure of signal-to-noise and $\hat{r}_i > 1$ implies meaningful signal. We also compute correlations between GRACE and NLDAS to observe how well the models agree with

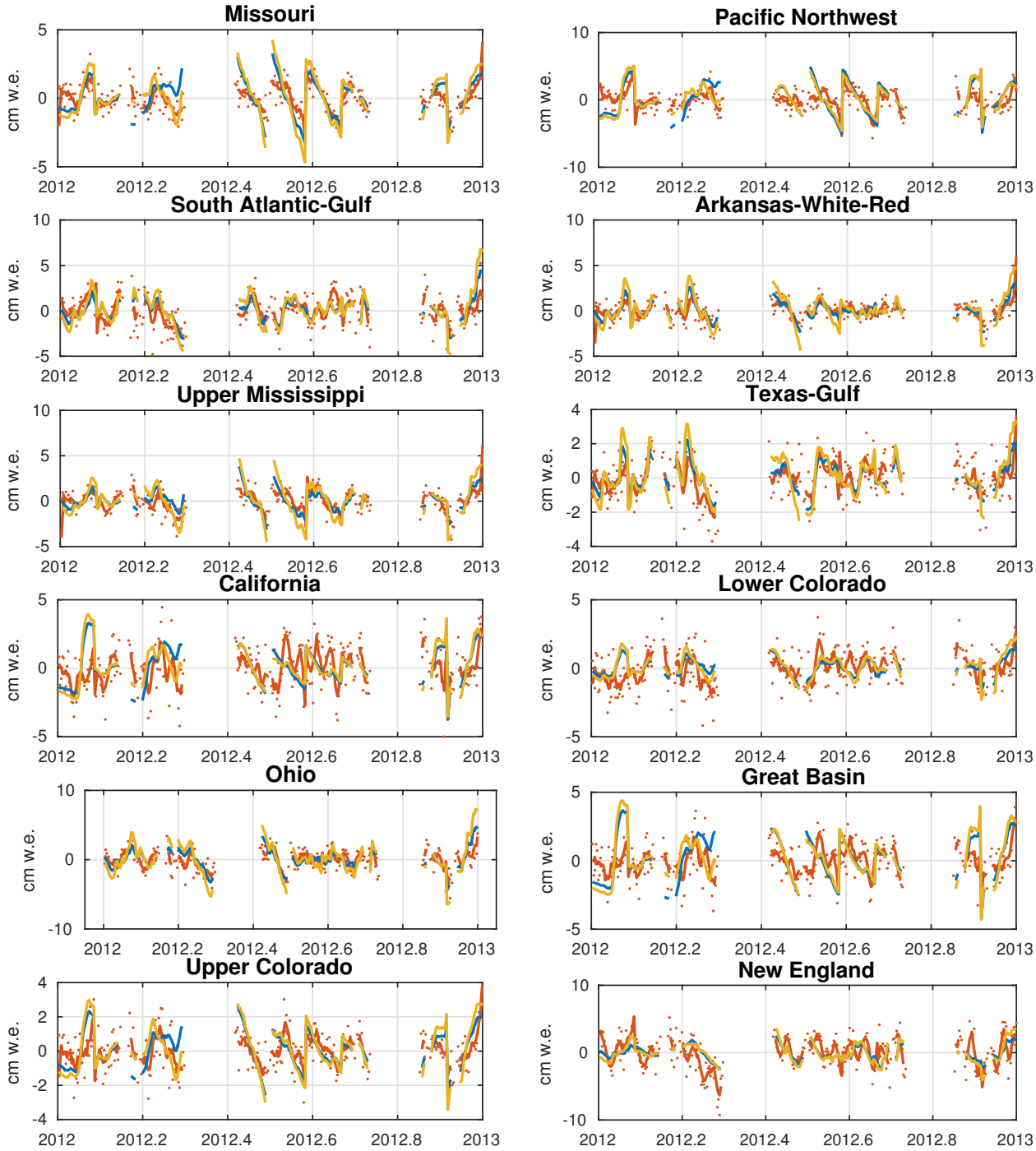

Figure 5.12: Comparison of daily estimates from GRACE with NLDAS model outputs for 12 basins in North America, with monthly means removed. GRACE daily estimates are dots in red, with a 5-day boxcar filter applied as red line. NLDAS-VIC is in blue and NLDAS-Noah is in yellow, each with the resolution operator applied. Gaps are days without GRACE observations.

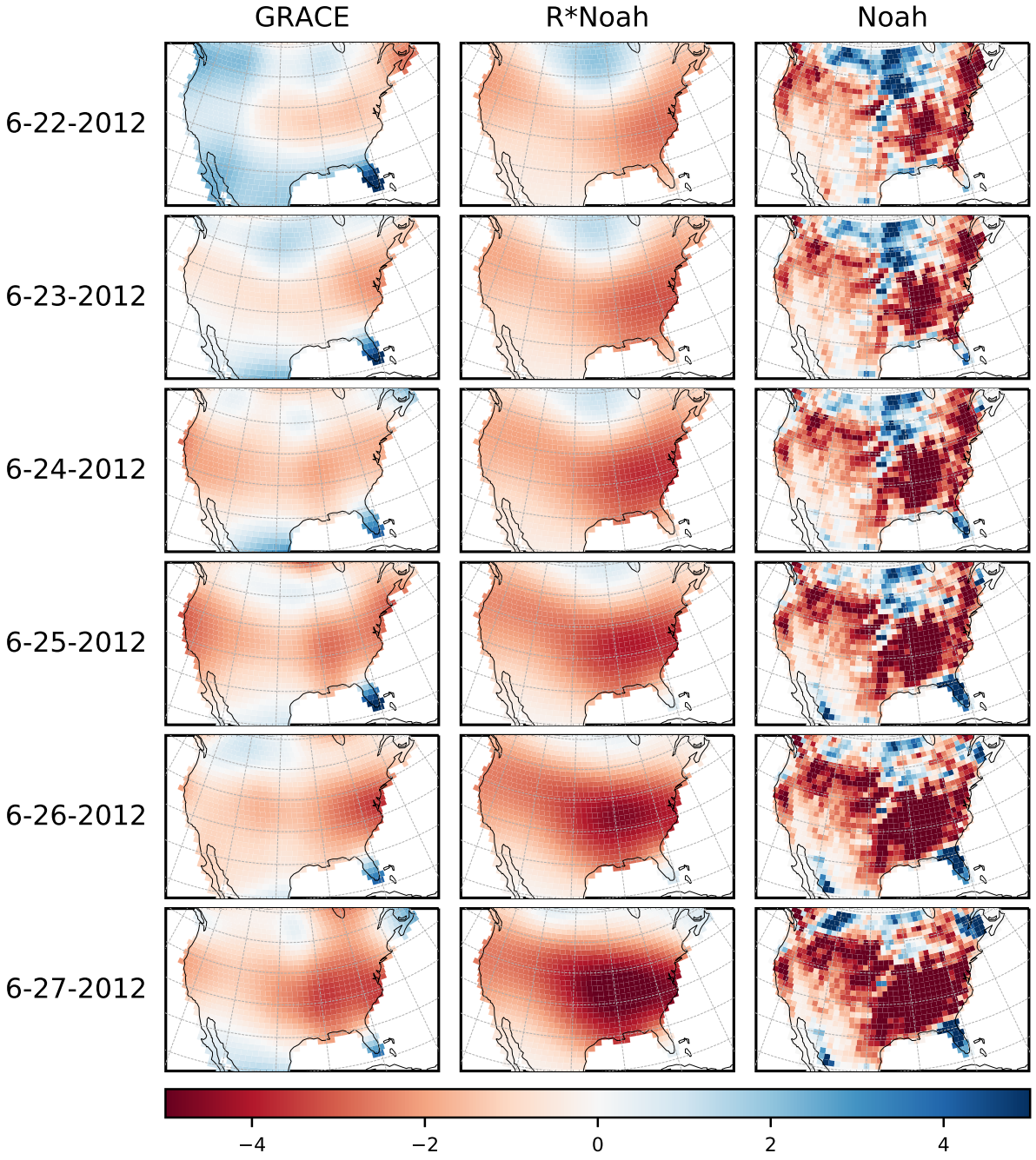

Figure 5.13: Maps for six consecutive days in June 2012 from GRACE and NLDAS-Noah. The center column depicts NLDAS with the mean resolution operator applied and the right column depicts NLDAS at mascon-averaged resolution

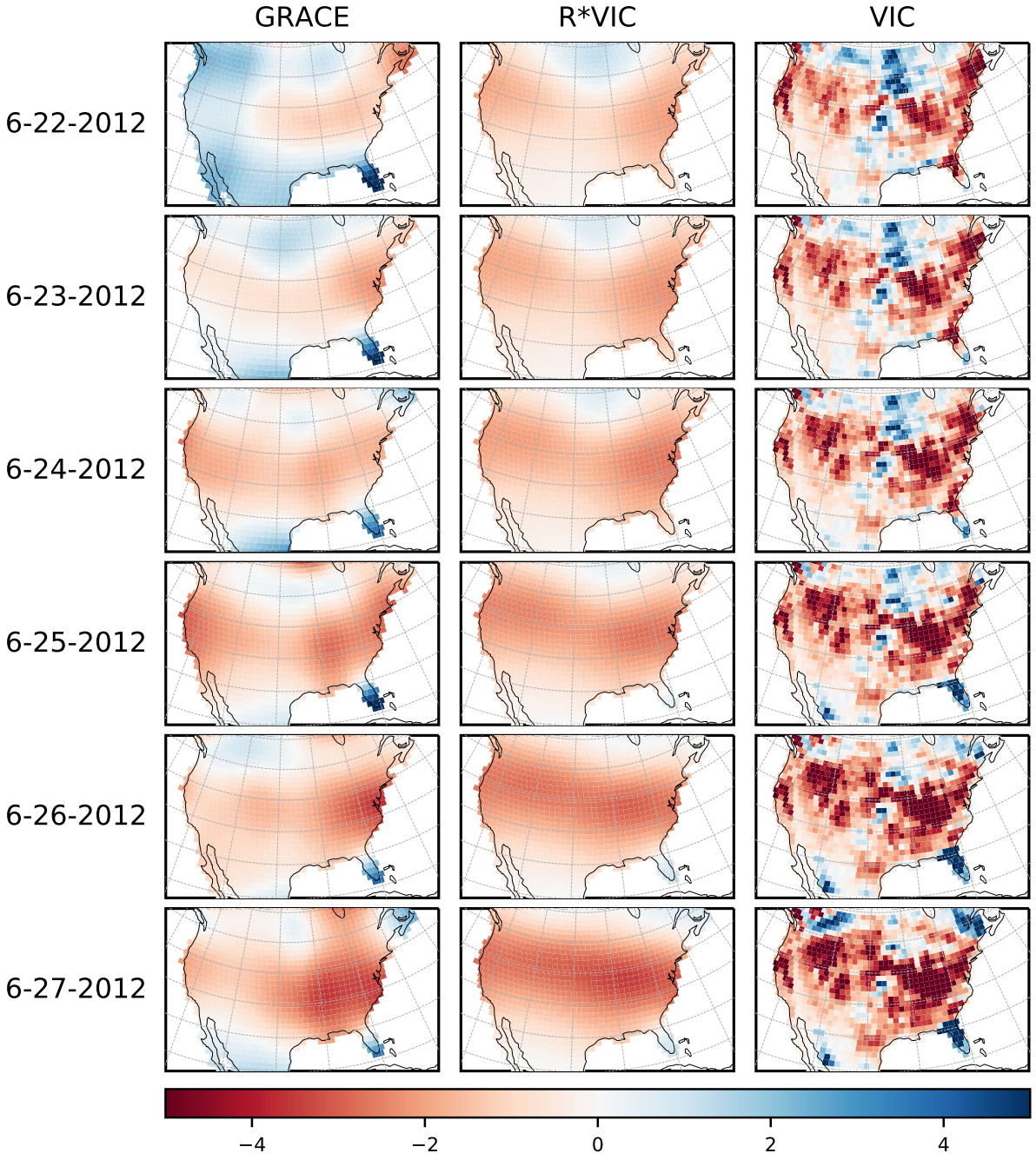

Figure 5.14: Maps for six consecutive days in June 2012 from GRACE and NLDAS-VIC. The center column depicts NLDAS with the mean resolution operator applied and the right column depicts NLDAS at mascon-averaged resolution.

GRACE estimates. These various parameters are computed for the daily deviations from monthly mean fields for 2012 for both NLDAS-Noah and NLDAS-VIC and summarized in Table 5.2.

GRACE daily solutions show the improved signal recoverability as basins increase in size and in latitude, meeting expectations. The standard deviation of recovered basin signals from GRACE, $\sigma_{i,GRACE}$, can be used as a proxy for the amount of signal recovered by the daily solution and shows a strong correlation with basin size. Signal-to-noise as determined by $\hat{r}_i$ likewise shows positive correlations basin size, though basin shape is also important. A latitude dependence in total bias is also measurable between basins of comparable sizes, with more northern basins such as the Upper Mississippi and Ohio basins showing better signal-to-noise than comparable basins in the Texas Gulf and Lower Colorado, respectively, for both models. Bias becomes increasingly dominant as basin size decreases. Wider basins, such as the Arkansas-White-Red and Ohio show better signal content than narrower basins of comparable size, such as the South Atlantic-Gulf and Lower Colorado. In general, basins 800,000 km^2 and larger show meaningful estimated signal, basins 300,000-800,000 km^2 show signal and bias to be of approximately the same size, and basins smaller than 300,000 km^2 show bias dominating signal. Similarly, correlations between GRACE and both versions of NLDAS decrease with basin size, with basins smaller than 250,000 km^2 showing reduced correlations, likely due to the limited observability of GRACE at daily timescales. For example, the Tennessee basin shows bias significantly overwhelming signal by every metric. This basin is approximately the size of the smallest observable basins with monthly GRACE data, and therefore it is not surprising that it is unobservable on daily timescales.

Finally, it is useful to consider these basins with the monthly mean fields from the GSFC solution restored. Figure 5.15 shows the same 12 basins as before, and the combined daily + monthly estimates now reflects the total mass change estimates for each basin for 2012. A few takeaways stand out in these plots. First, as suggested by the presented metrics for signal recovery and bias effects, basin estimates for the largest basins appear most realistic, with smaller basins increasingly dominated by bias. An important takeaway is that it is impossible to determine if these bias effects are due to signal from outside the basin leaking into the basin, or from signal inside the

Table 5.2: Basin analysis of daily mascon solution and model comparisons

Basin	Area, km^2	Lat. Range, °N	σ_{GRACE}, cm	$\sigma_{L,Noah}$, cm	$\sigma_{L,VIC}$, cm	$\hat{r}_{Noah}$	$\hat{r}_{VIC}$	$\rho_{G,N}$	$\rho_{G,V}$
Missouri	1,313,551	38.0-49.0	2.41	0.66	0.55	2.71	2.52	0.63	0.64
Pacific Northwest	805,526	42.0-50.0	1.99	1.14	1.14	1.99	1.97	0.63	0.61
South Atlantic-Gulf	743,538	26.0-37.0	1.69	1.63	1.21	0.95	0.96	0.63	0.57
Arkansas-White-Red	644,132	33.0-39.0	1.59	1.34	0.84	1.31	1.30	0.60	0.56
Upper Mississippi	495,659	38.0-47.0	1.59	1.40	1.01	1.44	1.33	0.57	0.55
Texas-Gulf	483,471	26.0-34.0	1.57	1.65	1.12	0.81	0.78	0.57	0.54
California	458,412	33.0-43.0	1.53	1.69	1.36	0.82	0.96	0.46	0.51
Lower Colorado	421,266	31.0-37.0	1.35	0.88	0.65	0.99	0.99	0.46	0.48
Ohio	421,218	36.0-42.0	1.33	1.69	1.22	1.22	1.20	0.45	0.45
Great Basin	371,666	36.0-42.0	1.29	0.90	0.75	1.86	2.08	0.44	0.44
Upper Colorado	297,306	36.0-43.0	1.19	0.93	0.51	1.47	2.21	0.44	0.40
Lower Mississippi	272,637	30.0-37.0	1.19	2.04	1.40	0.96	0.90	0.36	0.38
Mid-Atlantic	247,821	38.0-43.0	1.06	1.62	1.09	1.23	1.19	0.27	0.26
New England	210,622	42.0-47.0	1.02	1.87	1.40	0.82	0.77	0.24	0.20
Tennessee	111,496	35.0-37.0	1.01	2.48	1.79	0.95	0.84	0.12	0.10

$\rho_{G,N}$ and $\rho_{G,V}$ are the correlations between GRACE estimates and Noah and VIC estimates for each basin.

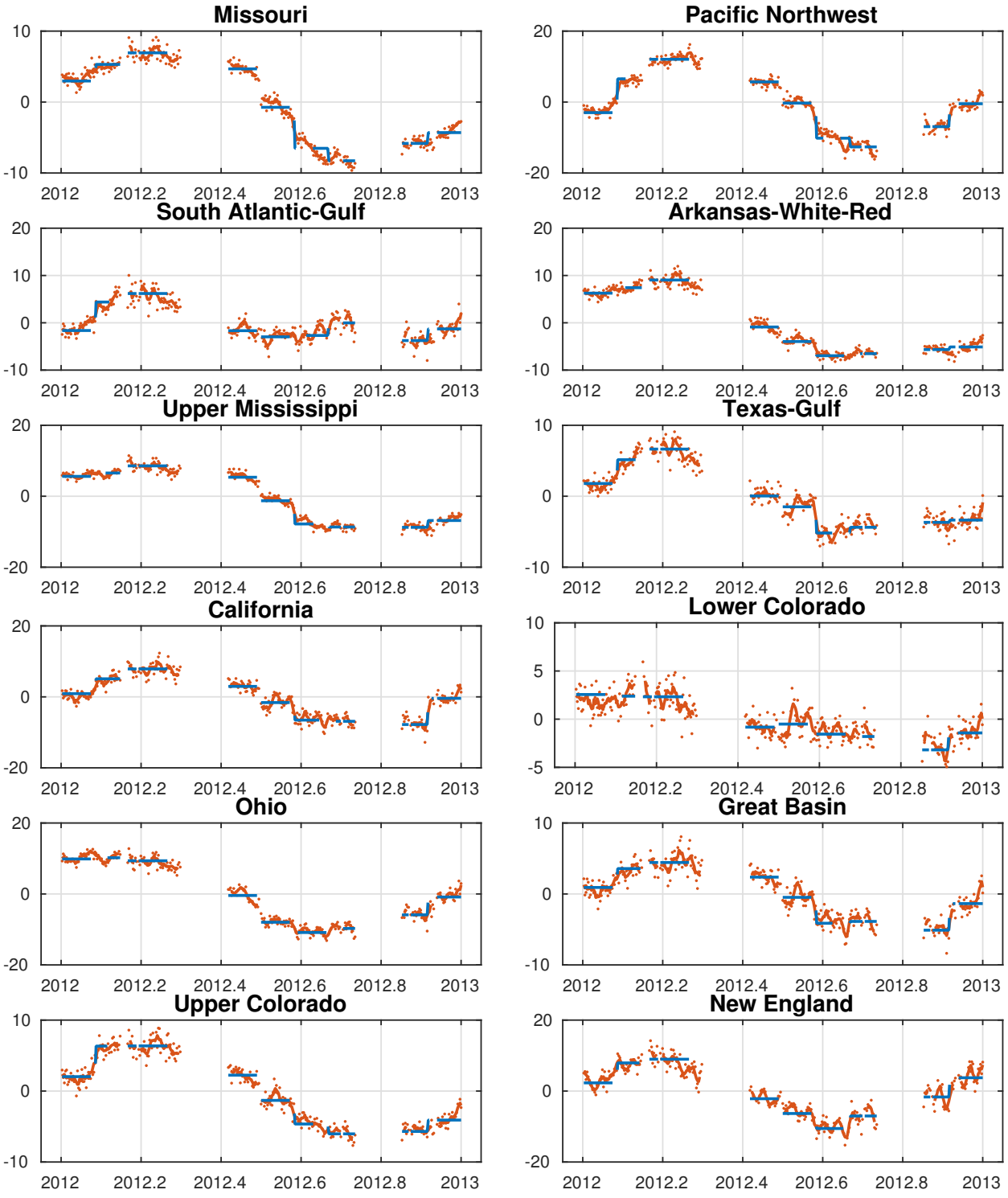

Figure 5.15: Daily basin estimates from GRACE with monthly reference restore. GRACE daily estimates are dots in red, with a 5-day boxcar filter applied as red line. The GSFC monthly solution is in blue, and data gaps are days without GRACE observations.

basin leaking outward. Second, as these basins are at mid-Latitudes where observability is greatly impacted by orbit proximity each day, these signals make it clear that any applications of TWS estimates from these daily solutions will need to adequately account for daily observability. This could take the form of using the estimation covariance matrix or the resolution operator, which both present measures of observability. For example, using either the resolution maps derived from the resolution operator or using the full resolution operator itself if enough computational resources are available, these daily solutions can be used for a variety of applications where better observed locations each day are trusted more while less well observed locations are trusted less. Considering data assimilation applications, the resolution operator can inform the assimilative system of the accuracy of surface mass estimates for each location each day, and impose observation weighting based on this information that determines how heavily each daily mascon estimate is considered. Finally, inspection of the full daily signal as it transitions from one month to another for months with large changes often results in a "jump" in the data. This jump reflects the relative differences in resolution between the monthly and daily solutions, where the monthly GSFC product is less influenced by spatial bias due to significantly better observational coverage, and therefore by default will capture more localized signals better.

5.3 Solution errors

Errors in the full daily solution are in 3 parts: errors carried forward from the monthly solution as described in *Luthcke et al.* (2013) and *Loomis et al.* (2019, under review), formal errors from the least squares fit, and bias caused by leakage as discussed above. These three components can be combined to form the total error in the solution. As the error in the monthly solution is not part of this dissertation, it will not be discussed in depth here.

As discussed in *Loomis et al.* (2019, under review), producing calibrated formal errors for the mascon solution becomes challenging. Uncalibrated errors from the least squares solution are available, but properly scaling these errors to reflect the real error in the estimate would require well known *in situ* information, and the errors of that data would have to be equally well known. Instead, similar to the method chosen for assessing the formal errors in the monthly solution (described in *Loomis et al.* (2019, under review)), a temporal filter is applied to the estimated solution and the difference between the filtered and unfiltered solution at each mascon is then used to approximate the error. This may over- or under-estimate the true error depending on the strength of the filter chosen. Any temporal filter will transform the individual daily estimates into temporally correlated estimates, but it can be assumed that days close to one another should behave similarly enough that such a filter will primarily damped noise in the estimate. For this analysis, a relatively simple 7-day boxcar smoother is applied to the daily estimate at each mascon. Figure 5.16 shows the mean of the computed noise uncertainties in the solution for 2012. A 7-day filter was chosen because the GRACE ground track passes within a few hundred kilometers of each mascon every 7 days or fewer. A longer filter would break down assumptions about signal versus noise that are damped in the filtered solution, while a shorter 5-day filter showed only minor differences. Therefore the 7-day filter is a relatively conservative approximation of the noise.

While formal error uncertainties are considered for each mascon, bias errors can be considered at either the mascon or basin level. In Equation 5.3, a relationship was developed to determine the leakage in the estimated solution from the truth $\mathbf{x}$. In reality, this truth is not known. Instead, the

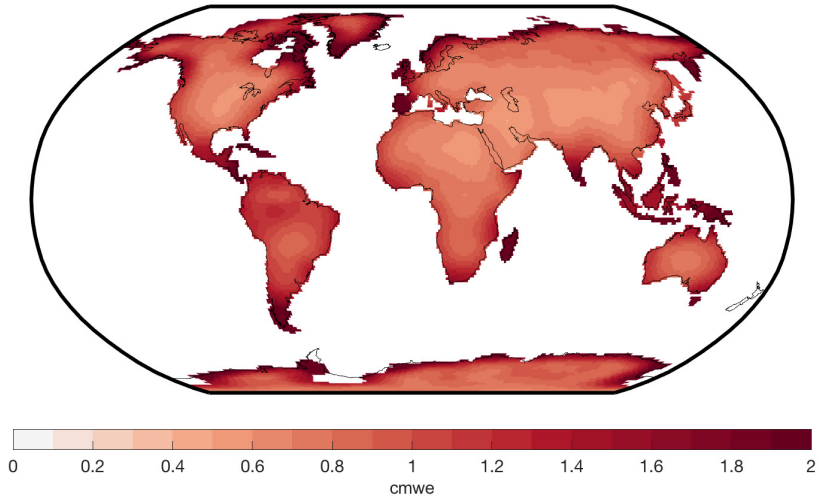

Figure 5.16: Map of the mean noise uncertainties in the daily estimate.

best estimate can be used to approximate the leakage following

$$\hat{l}(t) = (I - \mathbf{R})\hat{\mathbf{x}}(t). \tag{5.6}$$

As this approximation is determined from each day's best estimate, a more representative approximation of the bias can be determined for all days over a full month (which all shared the same background reference month from the GSFC solution) by computing the RMS of the leakage for each mascon over that month. Because this estimate of the bias is dependent on the biased daily best estimate, this estimate likely does not capture the full extent of the bias. Model output from the Global Land Data Assimilation System (GLDAS) could be substituted for $\hat{\mathbf{x}}$ and used similarly to comparisons with NLDAS in Section 5.2, but then the bias would be model-dependent. Figure 5.17 (top) shows the 2-σ bias map for July 2012 from this approximation using the mean resolution operator. However, it is often more appropriate to consider bias at a basin level, as leakage between mascons within a basin does not bias the total estimate of the basin itself. Applying the basin masks distributed with the monthly GSFC solution, the bias for each basin is shown in Figure 5.17 (bottom). The two figures show that while leakage causes substantial bias at the mascon

level globally, the geometry and location of a basin may be such that basin level bias is significantly smaller. For example, larger basins such as the Mississippi Basin and isolated basins in the designed regularization such as Greenland show significantly smaller leakage than at the mascon scale.

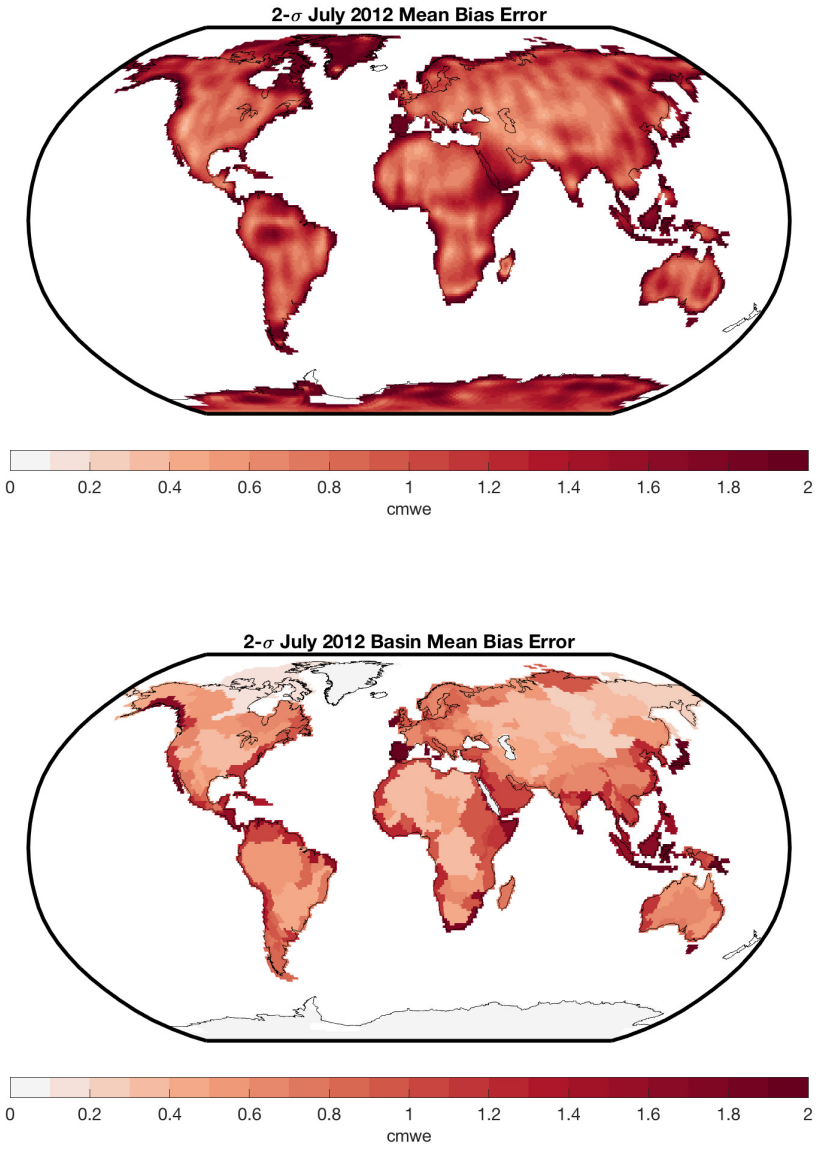

Figure 5.17: Maps of the bias uncertainties in the daily estimate for days in July 2012 using the mean resolution operator at mascon (top) and basin (bottom) scales.

5.4 Analysis of Polar Basins

While this dissertation focuses on hydrology applications and therefore the majority of this analysis has been over low- and mid-latitude basins, GRACE daily solutions show good promise for high-latitude applications as well, including in surface mass balance studies. Basin mass estimates for Greenland, Northern Canada, and Antarctica are shown in Figure 5.18. These estimates suggest that this daily solution can recovered sub-monthly hydrologic cycles with periods on the order of 10 days. Additionally, Greenland mass recovery is dominated by trends in ice melt, with secondary effects likely due to precipitation. The total signals in these regions (daily + monthly) is helpful to consider because it adds context to the recovered trends in the month. These signals are shown in Figure 5.19. The figure suggest that taken as a whole, Greenland ice melt is wholly captured in the recovered signal, as month-to-month jumps between the total daily signal due to bias effects are not seen for the region. This is different than what was observed in the NLDAS analysis of hydrologic basins, and likely due to both better observability in polar regions with GRACE and regional constraints that isolate Greenland from the rest of North America. As with the previous plot, the figure suggests a recovery of sub-monthly periodic surface mass changes in Antarctica. However, the figure now shows that these changes and the scatter in the individual daily solutions are of the same magnitude as the inter-monthly mass changes in Antarctica, suggesting that these recovered signals might be dominated by systematic bias or mis-modeling rather than completely realistic signals. This is an interesting finding, and could suggest that these daily signals may be recovering corrections to mis-modeled atmospheric mass fluctuations in Antarctica that are not well characterized in the atmospheric de-aliasing product. Further investigation of these signals is outside the immediate scope of this dissertation, but would be a natural extension of this work in the future. Statements about the accuracy of recovered signals in the Northwest Territories of Canada are less certain, but the figures suggest the recovery of some type of sub-monthly periodic mass fluctuation. Further investigation taking into account TWS and atmospheric effects from other datasets are needed to make any additional statements in this region.

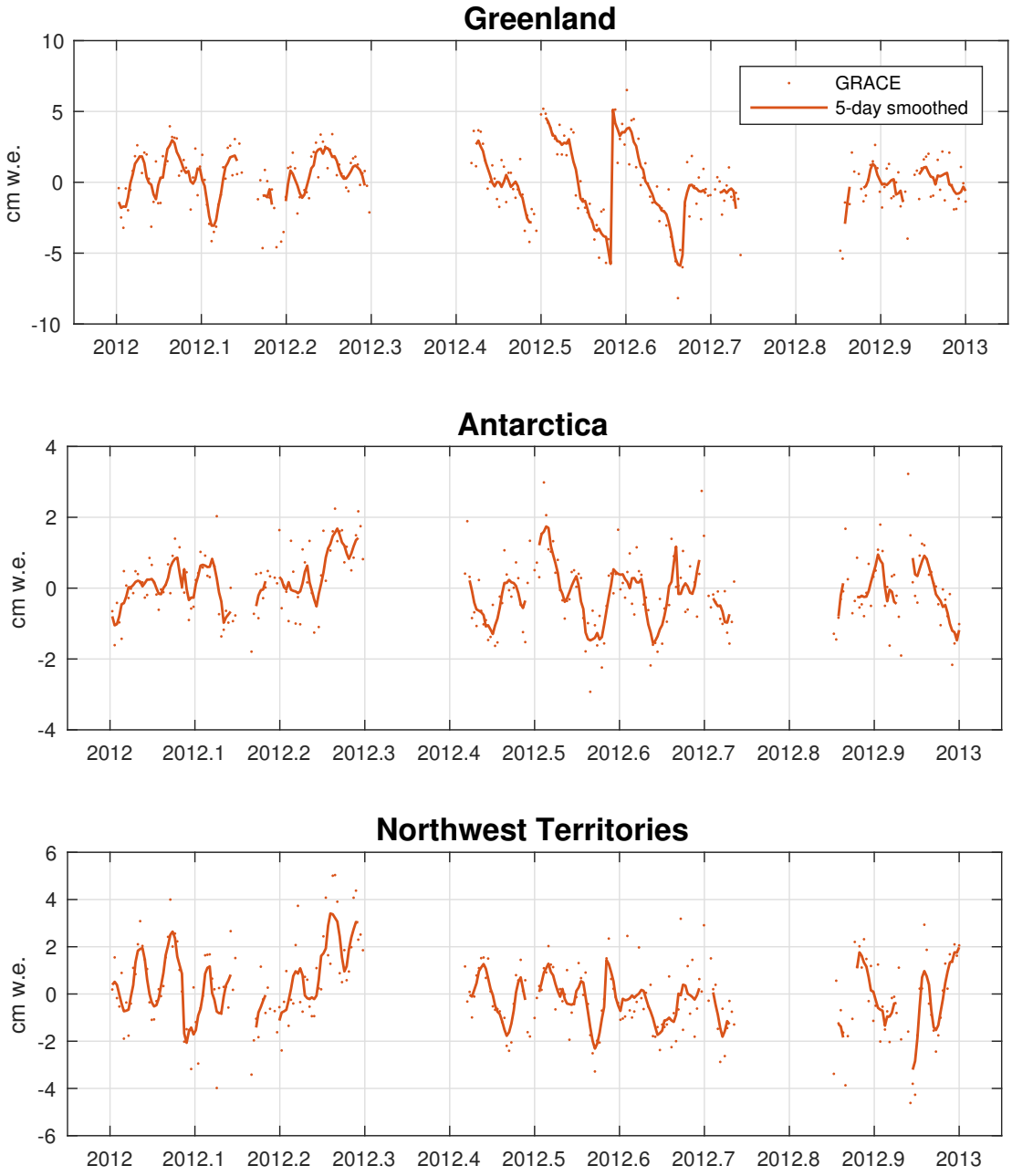

Figure 5.18: Daily-recovered signal in three polar regions: Greenland (top), Antarctica (middle), & Northwest Territories and the Canadian Archipelago.

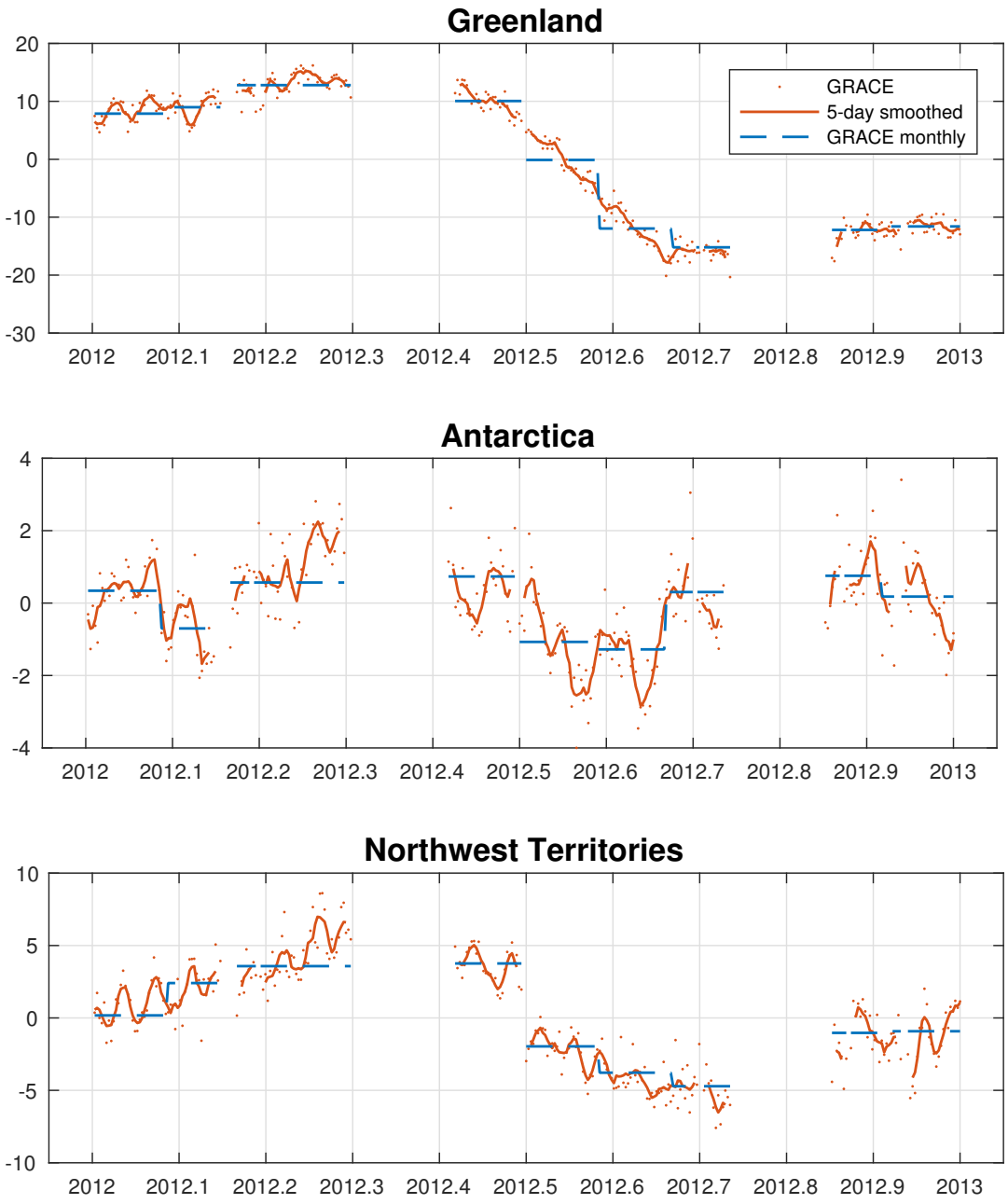

Figure 5.19: Daily-recovered signal with monthly fields restored in three polar regions: Greenland (top), Antarctica (middle), & Northwest Territories and the Canadian Archipelago.

Figure 5.20 shows polar maps of recovered daily signals for 10 consecutive days in June 2012. These maps suggest realistic recovery of hydrologic and cryospheric signals over Greenland, Northern Canada, and Russia, where maps of resolution as defined by the Gaussian smoothing radius and the columns of the resolution operator suggest signal resolution of approximately 400-450 km. Additionally, daily mass variations in coast Antarctica suggest meaningful surface mass recovery, while signals over interior Antarctica are less coherent, potentially reflecting atmospheric mismodeling.

For the presented regions and polar regions as a whole, it is likely that total basin mass estimates are influenced by the GRACE daily orbit paths, which may explain some of the periodicity in the recovered estimates. However, Figure 5.17 suggests that bias due to leakage is not a significant error source. Though GRACE has much better coverage at higher latitudes, daily solutions are still limited by the relatively space observations available from just 15 daily orbits, and best estimates of the resolution in these regions are still poorer than for most global locations monthly. Therefore, as in hydrology applications, rigorous use of this estimate for data assimilation or comparisons will require use of the full solution covariance or alternatively the resolution operator to most accurately interpret the mascon-by-mascon recovered signals.

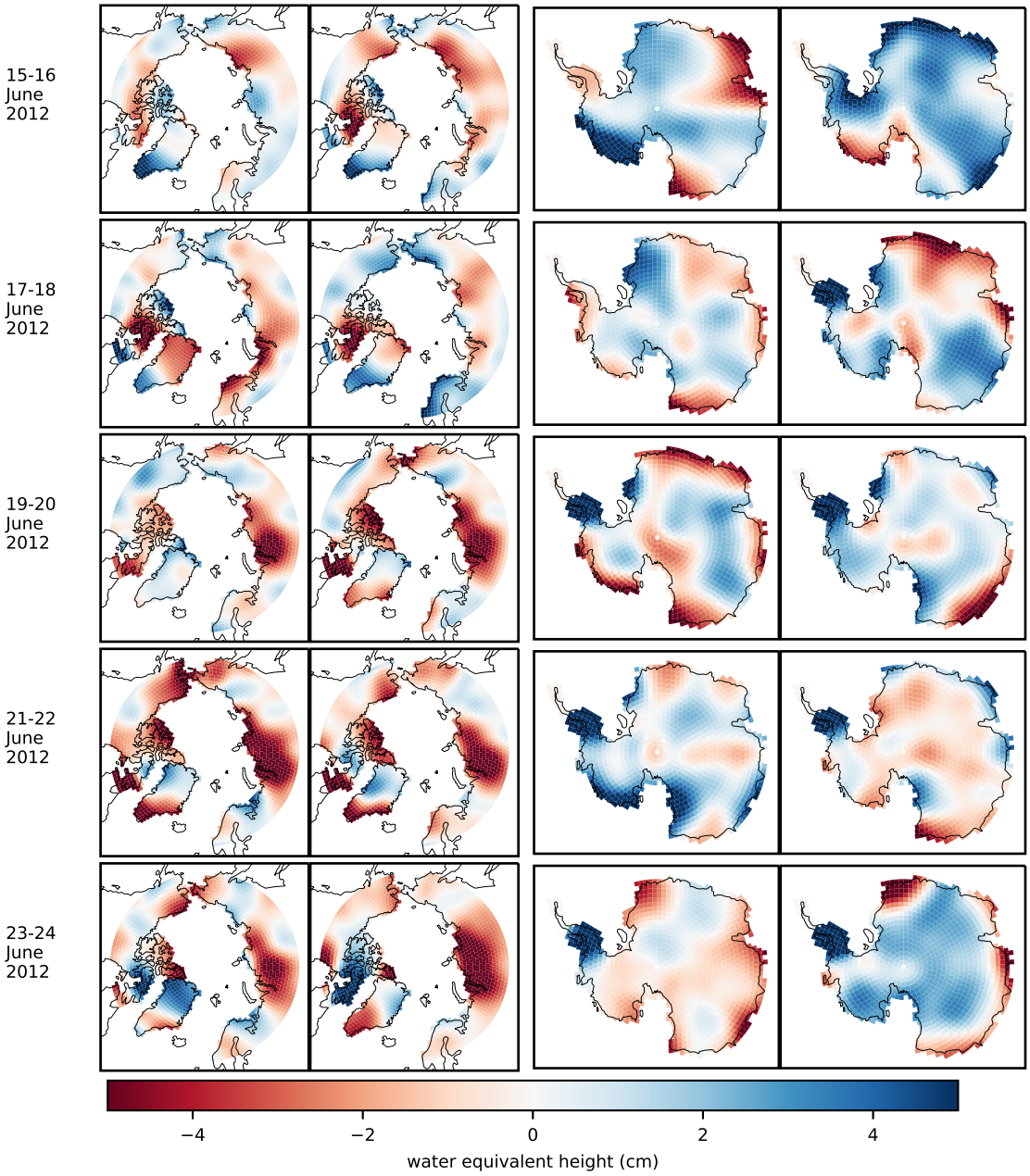

Figure 5.20: Maps for ten consecutive days in June 2012 from GRACE above 60°N and over Antarctica.

Chapter 6

Conclusions

In this dissertation, a daily GRACE estimate of TWS is designed and an analysis of the resulting solution is presented. This solution is designed as a global mascon product over land, using the same mascon definitions as the GSFC Global Mascon Solution. The daily solution is designed as an extra information layer on top of the GSFC monthly product, and the two thus form a hierarchical solution capturing high spatial information at monthly timescales and additional lower spatial information at daily timescales.

6.1 Summary of findings

Chapter 3 details the specific mascon representation used in this study and design of the least squares solution. In this chapter, the design of the estimation regularization scheme is detailed and design decisions are justified. Applying correlations between nearby mascons, regional boundary constraints, and latitude-dependent weighting, a global scaling factor was determined which provided for a minimally regularized solution. This minimal regularization was defined as the smallest weighting that fit the design criteria that a resulting solution should not show large correlated errors, manifested as vertical striping in each daily estimate. It was shown that certain small, isolated land basins are simply not observable on daily timescales. Alternative regularization strategies attempting to inform recovered signal location using various model-driven spatial distri-

butions or orbit track swaths were discussed, and the reasons for not implementing these concepts were argued.

Chapters 4 presented an analysis of a simulation utilizing the designed estimation system. This simulation showed that signal recovery has a large latitudinal dependence, with signal leakage in polar areas such as Greenland, Antarctica, or Finland being largely confined within approximately 600 km of the true signal, while mid-latitude areas showed leakage on the order of 1000 km, with many locations not fully recovering the original signal at even these distances. The simulation also showed the effectiveness of the regional constraints in the solution regularization matrix, which helped properly isolate signals in more confined land masses such as South America and showed that these lower-latitude regions could recover similar signal as better-observed mid-latitude areas not influenced by regional constraints. This simulation study provided expectations on signal recoverability in the actual daily solution.

A rigorous analysis of the actual recovered daily signal was then presented in Chapter 5. Building on the results of the simulation, a methodology was presented for determining the resolution of each estimated mascon, in terms of a Gaussian smoothing function like that used to describe GRACE spherical harmonic solution resolution. Resulting maps of this mascon-dependent resolution agreed with findings from the simulation study, justifying its use as a measure of bias in the solution and the resulting resolution of the solution. Whereas GRACE monthly solutions show signal resolutions on the order of 300 km, the developed daily solutions have latitudinally dependent resolutions ranging from approximately 450 km at high latitudes to 800+ km resolution at the equator, and these resolutions are further dependent on the geometries and proximities of regional boundaries in the solution.

A basin analysis was then conducted in comparison with two models from NLDAS, and a comparison methodology was established that ensured comparable signal resolutions between the GRACE estimates and the models. This analysis showed that basins 800,000 km^2 and larger exhibit high signal recovery compared to bias, while basins between 300,000 km^2 and 800,000 km^2 showed marginal signal recovery compared to bias, and the latitudes of these basins largely determined if

the basins were observable. In basins smaller than 250,000 km^2, bias resulting from leakage into and out of the basins dominated signal recoverability.

As high latitude locations were demonstrated to be particularly observable in the daily estimates, basins in Greenland, Northern Canada, and Antarctica were investigated. Without good estimates of surface mass variability on daily timescales to compare with, conclusions from these investigates must be somewhat muted, but the investigations showed that meaningful signals are recovered. Significant sub-monthly signal structure is recovered in all three regions, likely driven by sub-monthly precipitation- and melt-driven mass changes, though maps of interior Antarctica suggest factors such as atmospheric mis-modeling might also be drivers in the recovered mass estimates.

The resulting daily solutions capture daily surface mass variations from residual observation information aliased into the monthly GRACE solutions. These estimated variations are of significantly diminished spatial resolution as compared to the monthly solutions, but show promising signal recovery.

6.2 Applications and Future Outlook

The developed daily solution shows great promise as a low-resolution estimate of daily TWS variability, complimentary to high spatial resolution monthly and long-term information in the GSFC monthly mascon solution. Daily TWS estimates have immediate uses in applications using GRACE data to capture changes in the total water content of an area, either standalone as with basin estimates of TWS or in conjunction with measurements of soil moisture, canopy water storage, or surface water content to separate various components of TWS. Historical analyses of daily variability can provide insights into propagations of any number of TWS signals. A more immediate application, however, is to use these daily estimates as temporal constraints coupled with monthly estimates as spatial constraints to inform historical data assimilation systems and

data-driven models. The new information provided by daily mascon estimates and their associated daily errors allow assimilation efforts to use GRACE data at multiple spatiotemporal resolutions, addressing some of the challenges highlighted by *Livneh and Lettenmaier* (2012) and *Girotto et al.* (2017). Further improvements in applying GRACE to data assimilation efforts would likely require the direct inclusion of GRACE Level-1B ranging observations, which only a few centers are currently equipped to process due to the many components that must be considered when using this data. Higher resolution at polar locations suggests these solutions can likewise be used for better parameterization of surface mass balance models, allowing GRACE information to inform these models at better temporal scales while maintaining spatial resolutions close to those in monthly estimates. Resolution information from the resolution operator or the variance-covariance matrix can be used to correctly assimilate the daily information.

These daily solutions have obvious uses in any applications requiring high temporal sampling, but near real time applications requiring up-to-date daily information pose a significant hurdle. In the developed solution, the fully converged monthly estimate is used as a background forward model, allowing this daily estimate to determine only deviations from that monthly state, rather than the full gravity field. For this solution to be developed as a near real time product, significant investments will be needed, either in time or computational capacity or both. First, lag time associated with the processing of GRACE Level-1A raw observation data into estimation-ready Level-1B ranging data must be reduced. This first round of processing is not instant, and historically has required 2 or more weeks between data collection and processing completion. Assuming this time is reduced, the second obstacle is to rapidly turn around a high resolution monthly estimate for inclusion in the reference forward model. This could take many forms. For instance, every few days a new 30-day solution could be computed from the most recent 30 days of available data, and then this estimate could be used as the reference for near real time daily grid estimation. Alternatively, the most recent converged monthly solution could be extended into the future, either by attempting to project signal evolution based on some historical model or by simply maintaining that most recent field as the reference model state. In any case, overcoming these obstacles is a

logistical problem more than a research problem, and once overcome the daily solution developed in this dissertation could be applied to such a system.

This dissertation focused on recovering daily signals over land, assuming the background ocean de-aliasing product captured enough of the daily variability over the oceans to be able to heavily constrain ocean mascons. Due to the low spatial resolution of the developed daily estimates and smaller signal magnitudes over the oceans to begin with, this assumption is not likely to bias any recovered TWS signals. However, there are likely use cases where attempting to resolve daily ocean variability would be helpful, such as for improvements to ocean models, including the de-aliasing product used in the background model. In particular, such solutions could positively impact models of ocean bottom pressure on sub-monthly scales. If there is a demand for such a product, the findings in this dissertation can be used to help inform a proper regularization for recovering ocean mass variability.

This dissertation focused on daily time-variable gravity estimation from GRACE observations alone. These estimates are greatly effected by daily observability issues due to each daily orbit. If improvements to daily spatial resolution are desired, one possible option is to include additional data types in the least squares inversion along with the Level-1B K-band ranging observations. Possible data types to include are satellite laser ranging (SLR) measurements from other geodetic satellites, laser altimetry measurements of ice sheet elevation, GPS ground station measurements of vertical land motion, and radar altimetry measurements of sea surface height anomalies. SLR measurements are the most directly applicable, as these provide comparable observables of time-variable gravity to GRACE. Ice and ocean altimetry provide separate components of time variable gravity each coupled with other signals, and therefore the application of these in gravity field estimation requires additional assumptions and models related to surface mass balance and ocean temperature. GPS measurements require processing and an understanding of the various surface loading effects at each ground station, but can be related to surface mass variations. The inclusion of these data types can improve the resolvability of both long-wavelength variations (SLR) and localized signals (GPS, altimetry).

6.3 Concluding Remarks

This dissertation has developed a new type of daily GRACE solution, resolving TWS on daily timescales given daily information and establishing expected performance metrics for signal resolution in these solutions. These daily estimates are applicable in hydrology applications in basins and regionally, and show strong potential in cryospheric regions where daily GRACE observations are most available. Lower spatial resolution information from the developed solution, used in conjunction with high spatial resolution monthly solutions, can in turn be used to best characterize time-variability across multiple spatiotemporal scales.

Bibliography

A, G., J. Wahr, and S. Zhong (2013), Computations of the viscoelastic response of a 3-D compressible Earth to surface loading: an application to Glacial Isostatic Adjustment in Antarctica and Canada, *Geophysical Journal International*, *192*(2), 557–572, doi:10.1093/gji/ggs030.

AGU (2017), 2017 American Geophysical Union Fall Meeting, in *Proc. of the 2017 AGU Fall Meeting, December 11-15, 2017.*, American Geophysical Union, New Orleans, Louisiana, USA.

Bettadpur, S. (2018), Gravity recovery and climate experiment level-2 gravity field product user handbook, *GRACE Documentation GRACE 327-734 (CSR-GR-03-01)*, Center for Space Research, The University of Texas at Austin.

Beyerle, G., T. Schmidt, G. Michalak, S. Heise, J. Wickert, and C. Reigber (2005), Gps radio occultation with grace: Atmospheric profiling utilizing the zero difference technique, *Geophysical Research Letters*, *32*(13), doi:10.1029/2005GL023109.

Boening, C., J. K. Willis, F. W. Landerer, R. S. Nerem, and J. Fasullo (2012), The 2011 La Nia: So strong, the oceans fell: LA NIA 2011-SO STRONG, THE OCEANS FELL, *Geophysical Research Letters*, *39*(19), n/a–n/a, doi:10.1029/2012GL053055.

Brown, D., and S. McDonnell (2012), Nasa's grail creates most accurate moon gravity map, `https://www.nasa.gov/mission_pages/grail/news/grail20121205.html`, accessed: 2018-11-15.

Caron, L., E. R. Ivins, E. Larour, S. Adhikari, J. Nilsson, and G. Blewitt (2018), GIA Model Statistics for GRACE Hydrology, Cryosphere, and Ocean Science, *Geophysical Research Letters*, *45*(5), 2203–2212, doi:10.1002/2017GL076644.

Carrère, L., and F. Lyard (2003), Modeling the barotropic response of the global ocean to atmospheric wind and pressure forcing - comparisons with observations, *Geophysical Research Letters*, *30*(6), doi:10.1029/2002GL016473.

Chambers, D. (2012), Grace monthly ocean mass grids netcdf release 5.0. ver. 5.0., doi:10.5067/TEOCN-0N005.

Chambers, D. P., and J. A. Bonin (2012), Evaluation of Release-05 GRACE time-variable gravity coefficients over the ocean, *Ocean Science*, *8*(5), 859–868, doi:10.5194/os-8-859-2012.

Chambers, D. P., A. Cazenave, N. Champollion, H. Dieng, W. Llovel, R. Forsberg, K. von Schuckmann, and Y. Wada (2017), Evaluation of the Global Mean Sea Level Budget between 1993 and 2014, *Surveys in Geophysics*, *38*(1), 309–327, doi:10.1007/s10712-016-9381-3.

Chao, B. F., W. P. O'Connor, A. T. C. Chang, D. K. Hall, and J. L. Foster (1987), Snow load effect on the Earth's rotation and gravitational field, 1979-1985, *Journal of Geophysical Research*, *92*(B9), 9415–9422.

Cheng, M., B. D. Tapley, and J. C. Ries (2013), Deceleration in the Earth's oblateness, *Journal of Geophysical Research: Solid Earth*, *118*(2), 740–747, doi:10.1002/jgrb.50058.

Church, J., et al. (2013), *Sea Level Change. In: Climate Change 2013: The Physical Science Basis. Contribution of Working Group I to the Fifth Assessment Report of the Intergovernmental Panel on Climate Change*, 1137-1216 pp., [Stocker, T.F., D. Qin, G.-K. Plattner, M. Tignor, S.K. Allen, J. Boschung, A. Nauels, Y. Xia, V. Bex and P.M. Midgley (eds.)]. Cambridge University Press, Cambridge, United Kingdom and New York, NY, USA, doi:10.1017/CBO9781107415324.026.

Church, J. A., and N. J. White (2011), Sea-Level Rise from the Late 19th to the Early 21st Century, *Surveys in Geophysics*, *32*(4-5), 585–602, doi:10.1007/s10712-011-9119-1.

Cole, S., and A. Buis (2017), Prolific earth gravity satellites end science mission.

Croteau, M. J., and R. S. Nerem (2016), The Mascon Visualization Tool, Available from: http://ccar.colorado.edu/grace/ (Accessed 26 April 2017).

Drake, N. (2012), Twin gravity-mapping probes peer into the moon?s secrets, `https://www.wired.com/2012/12/grail-moon-probes-results/`, accessed: 2018-11-15.

Famiglietti, J. S., and M. Rodell (2013), Water in the balance, *Science*, *340*(6138), 1300–1301, doi:10.1126/science.1236460.

Flechtner, F., et al. (2016), Status of the grace follow-on mission, in *Presented at the GRACE Science Team Meeting, Potsdam, Germany, 5-7 Oct.*

Girotto, M., G. J. M. De Lannoy, R. H. Reichle, and M. Rodell (2016), Assimilation of gridded terrestrial water storage observations from GRACE into a land surface model, *Water Resources Research*, *52*(5), 4164–4183, doi:10.1002/2015WR018417.

Girotto, M., G. J. M. DeLannoy, R. H. Reichle, M. Rodell, C. Draper, S. N. Bhanja, and A. Mukherjee (2017), Benefits and pitfalls of GRACE data assimilation: A case study of terrestrial water storage depletion in India, *Geophysical Research Letters*, *44*(9), 4107–4115, doi:10.1002/2017GL072994.

Hamlington, B. D., M. W. Strassburg, R. R. Leben, W. Han, R. S. Nerem, and K.-Y. Kim (2014), Uncovering an anthropogenic sea-level rise signal in the pacific ocean, *Nature Climate Change*, *4*, 782 EP –.

Han, S.-C., C. K. Shum, M. Bevis, C. Ji, and C.-Y. Kuo (2006), Crustal Dilatation Observed by GRACE After the 2004 Sumatra-Andaman Earthquake, *Science*, *313*(5787), 658–662, doi:10.1126/science.1128661.

Han, S.-C., J. Sauber, S. B. Luthcke, C. Ji, and F. F. Pollitz (2008), Implications of postseismic gravity change following the great 2004 Sumatra-Andaman earthquake from the regional harmonic analysis of GRACE intersatellite tracking data, *Journal of Geophysical Research*, *113*(B11), doi:10.1029/2008JB005705.

Hardy, R. A., R. S. Nerem, and D. N. Wiese (2017), The Impact of Atmospheric Modeling Errors on GRACE Estimates of Mass Loss in Greenland and Antarctica: GRACE ATMOSPHERIC ERRORS OVER ICE SHEETS, *Journal of Geophysical Research: Solid Earth*, *122*(12), 10,440–10,458, doi:10.1002/2017JB014556.

Hoare, M. R. (2005), *The Quest for the True Figure of the Earth*, Routledge, Abingdon, Oxfordshire, UK.

Hoerl, A. E., and R. W. Kennard (1970), Ridge regression: Biased estimation for nonorthogonal problems, *Technometrics*, *12*(1), 55–67, doi:10.1080/00401706.1970.10488634.

Houborg, R., M. Rodell, B. Li, R. Reichle, and B. F. Zaitchik (2012), Drought indicators based on model-assimilated Gravity Recovery and Climate Experiment (GRACE) terrestrial water storage observations, *Water Resources Research*, *48*(7), W07,525, doi:10.1029/2011WR011291.

Jekeli, C. (2009), Potential theory and static gravity field of the earth, in *Treatise on Geophysics: Geodesy*, edited by G. Schubert and T. Herring, chap. 2, pp. 11–42, Elsevier, Amsterdam, the Netherlands.

Johnson, G. C., and D. P. Chambers (2013), Ocean bottom pressure seasonal cycles and decadal trends from GRACE Release-05: Ocean circulation implications, *Journal of Geophysical Research: Oceans*, *118*(9), 4228–4240, doi:10.1002/jgrc.20307.

Jones, B. A. (2010), Efficient models for the evaluation and estimation of the gravity field, Ph.D. thesis, UNIVERSITY OF COLORADO AT BOULDER.

Kaula, W. M. (2000), *Theory of Satellite Geodesy: Applications of Satellites to Geodesy*, Dover Publications, Mineola, New York, USA.

Kumar, S. V., et al. (2016), Assimilation of Gridded GRACE Terrestrial Water Storage Estimates in the North American Land Data Assimilation System, *Journal of Hydrometeorology*, *17*(7), 1951–1972, doi:10.1175/JHM-D-15-0157.1.

Kurtenbach, E., A. Eicker, T. Mayer-Grr, M. Holschneider, M. Hayn, M. Fuhrmann, and J. Kusche (2012), Improved daily GRACE gravity field solutions using a kalman smoother, *Journal of Geodynamics*, *59-60*, 39–48, doi:10.1016/j.jog.2012.02.006.

Landerer, F. W., D. N. Wiese, K. Bentel, C. Boening, and M. M. Watkins (2015), North Atlantic meridional overturning circulation variations from GRACE ocean bottom pressure anomalies: Namoc from Grace Observations, *Geophysical Research Letters*, *42*(19), 8114–8121, doi:10.1002/2015GL065730.

Lemoine, F. G., et al. (1998), The development of the joint nasa gsfc and nima geopotential model egm96, *Tech. Rep. NASA/TP-1998-206861*, NASA Goddard Space Flight Center, Greenbelt, Maryland, 20771 USA.

Lemoine, F. G., et al. (2013), High-degree gravity models from GRAIL primary mission data: HIGH-DEGREE GRAIL GRAVITY MODELS, *Journal of Geophysical Research: Planets*, *118*(8), 1676–1698, doi:10.1002/jgre.20118.

Livneh, B., and D. P. Lettenmaier (2012), Multi-criteria parameter estimation for the Unified Land Model, *Hydrology and Earth System Sciences*, *16*(8), 3029–3048, doi:10.5194/hess-16-3029-2012.

Loomis, B. D., S. B. Luthcke, and T. J. Sabaka (2019, under review), Regularization and error characterization of grace mascons.

Luthcke, S. B., H. J. Zwally, W. Abdalati, D. D. Rowlands, R. D. Ray, R. S. Nerem, F. G. Lemoine, J. J. McCarthy, and D. S. Chinn (2006), Recent greenland ice mass loss by drainage system from satellite gravity observations, *Science*, *314*(5803), 1286–1289, doi:10.1126/science.1130776, PMID: 17053112.

Luthcke, S. B., T. J. Sabaka, B. D. Loomis, A. A. Arendt, J. J. McCarthy, and J. Camp (2013), Antarctica, greenland and gulf of alaska land-ice evolution from an iterated GRACE global mascon solution, *Journal of Glaciology*, *59*(216), 613–631, doi:10.3189/2013JoG12J147.

Mayer-Gürr, T., S. Behzadpour, M. Ellmer, A. Kvas, B. Klinger, and N. Zehentner (2016), Itsg-grace2016 - monthly and daily gravity field solutions from grace, in *GFZ Data Services. http://doi.org/10.5880/icgem.2016.007.*

Merriam-Webster (), Geodesy.

Muller, P. M., and W. L. Sjogren (1968), Mascons: Lunar mass concentrations, *Science*, *161*(3842), 680–684, doi:10.1126/science.161.3842.680, PMID: 17801458.

National Governors Association Center for Best Practices, C. o. C. S. S. O. (2010), *Common Core State Standards*, National Governors Association Center for Best Practices, Council of Chief State School Officers, Washington D.C.

Nerem, R. S., C. Jekeli, and W. M. Kaula (1995), Gravity field determination and characteristics: Retrospective and prospective, *Journal of Geophysical Research: Solid Earth*, *100*(B8), 15,053–15,074, doi:10.1029/94JB03257.

Nerem, R. S., D. P. Chambers, C. Choe, and G. T. Mitchum (2010), Estimating Mean Sea Level Change from the TOPEX and Jason Altimeter Missions, *Marine Geodesy*, *33*(sup1), 435–446, doi:10.1080/01490419.2010.491031.

Nerem, R. S., B. D. Beckley, J. T. Fasullo, B. D. Hamlington, D. Masters, and G. T. Mitchum (2018), Climate-changedriven accelerated sea-level rise detected in the altimeter era, *Proceedings of the National Academy of Sciences*, p. 201717312, doi:10.1073/pnas.1717312115.

Newton, I. (1687), *Philosophiae naturalis principia mathematica*, J. Societatis Regiae ac Typis J. Streater.

Pail, R., et al. (2010), Combined satellite gravity field model goco01s derived from goce and grace, *Geophysical Research Letters*, *37*(20), doi:10.1029/2010GL044906.

Panet, I., S. Bonvalot, C. Narteau, D. Remy, and J.-M. Lemoine (2018), Migrating pattern of deformation prior to the Tohoku-Oki earthquake revealed by GRACE data, *Nature Geoscience*, *11*(5), 367–373, doi:10.1038/s41561-018-0099-3.

Ray, R. D. (1999), A global ocean tide model from TOPEX/Poseidon altimetry/GOT99.2, *NASA Technical Report NASA/TM-1999-209478*, NASA Goddard Space Flight Center.

Rodell, M., J. Chen, H. Kato, J. S. Famiglietti, J. Nigro, and C. R. Wilson (2006), Estimating groundwater storage changes in the Mississippi River basin (USA) using GRACE, *Hydrogeology Journal*, *15*(1), 159–166, doi:10.1007/s10040-006-0103-7.

Rodell, M., J. S. Famiglietti, D. N. Wiese, J. T. Reager, H. K. Beaudoing, F. W. Landerer, and M.-H. Lo (2018), Emerging trends in global freshwater availability, *Nature*, *557*(7707), 651–659, doi:10.1038/s41586-018-0123-1.

Rowlands, D. D., S. B. Luthcke, S. M. Klosko, F. G. R. Lemoine, D. S. Chinn, J. J. McCarthy, C. M. Cox, and O. B. Anderson (2005), Resolving mass flux at high spatial and temporal resolution using GRACE intersatellite measurements, *Geophysical Research Letters*, *32*(4), n/an/a, doi: 10.1029/2004GL021908.

Sabaka, T. J., D. D. Rowlands, S. B. Luthcke, and J.-P. Boy (2010), Improving global mass flux solutions from gravity recovery and climate experiment (GRACE) through forward modeling and continuous time correlation, *Journal of Geophysical Research*, *115*(B11), doi:10.1029/2010JB007533.

Sakumura, C., S. Bettadpur, H. Save, and C. McCullough (2016), High-frequency terrestrial water storage signal capture via a regularized sliding window mascon product from grace, *Journal of Geophysical Research: Solid Earth*, *121*(5), 4014–4030.

Save, H., S. Bettadpur, and B. D. Tapley (2016), High-resolution csr grace rl05 mascons, *Journal of Geophysical Research: Solid Earth*, *121*(10), 7547–7569.

Seaber, P. R., F. P. Kapinos, and G. L. Knapp (1987), Hydrologic unit maps, *United States Geological Survey Water-Supply Paper 2294*, U.S. Department of the Interior.

Shepherd, A., et al. (2012), A Reconciled Estimate of Ice-Sheet Mass Balance, *Science*, *338*(6111), 1183–1189, doi:10.1126/science.1228102.

Shepherd, A., et al. (2018), Mass balance of the Antarctic Ice Sheet from 1992 to 2017, *Nature*, *558*(7709), 219–222, doi:10.1038/s41586-018-0179-y.

Shuman, C. A., H. J. Zwally, B. E. Schutz, A. C. Brenner, J. P. DiMarzio, V. P. Suchdeo, and H. A. Fricker (2006), ICESat Antarctic elevation data: Preliminary precision and accuracy assessment, *Geophysical Research Letters*, *33*(7), doi:10.1029/2005GL025227.

Swenson, S., and J. Wahr (2002), Methods for inferring regional surface-mass anomalies from gravity recovery and climate experiment (grace) measurements of time-variable gravity, *Journal of Geophysical Research: Solid Earth*, *107*(B9).

Swenson, S., and J. Wahr (2006), Post-processing removal of correlated errors in GRACE data, *Geophysical Research Letters*, *33*(8), doi:10.1029/2005GL025285.

Swenson, S., D. Chambers, and J. Wahr (2008), Estimating geocenter variations from a combination of GRACE and ocean model output, *Journal of Geophysical Research: Solid Earth*, *113*(B8), doi: 10.1029/2007JB005338.

Swenson, S. C. (2012), Grace monthly land water mass grids netcdf release 5.0. ver. 5.0., doi: 10.5067/TELND-NC005.

Tapley, B. (2018), Grace satellite and instrument status at the end of the mission, in *Abstract GSTM-2018-85 presented at 2018 GRACE/GRACE-FO Science Team Meeting, Potsdam, Germany, 9-11 Oct.*

Tapley, B., F. Flechtner, C. Boening, and S. Bettadpur (2016), Grace mission: Status and prospects, in *Presented at 2016 GRACE Science Team Meeting, Potsdam, Germany, 5-7 Oct.*

Tapley, B. D. (2004), GRACE Measurements of Mass Variability in the Earth System, *Science*, *305*(5683), 503–505, doi:10.1126/science.1099192.

Tapley, B. D., S. Bettadpur, M. Watkins, and C. Reigber (2004a), The gravity recovery and climate experiment: Mission overview and early results, *Geophysical Research Letters*, *31*(9).

Tapley, B. D., B. E. Schutz, and G. H. Born (2004b), *Statistical Orbit Determination*, Elsevier Academic Press, Burlington, MA, USA.

Tebaldi, C., B. H. Strauss, and C. E. Zervas (2012), Modelling sea level rise impacts on storm surges along US coasts, *Environmental Research Letters*, *7*(1), 014,032, doi:10.1088/1748-9326/7/1/014032.

Thomas, A. C., J. T. Reager, J. S. Famiglietti, and M. Rodell (2014), A GRACE-based water storage deficit approach for hydrological drought characterization, *Geophysical Research Letters*, *41*(5), 2014GL059,323, doi:10.1002/2014GL059323.

Tourian, M. J., J. T. Reager, and N. Sneeuw (2018), The Total Drainable Water Storage of the Amazon River Basin: A First Estimate Using GRACE, *Water Resources Research*, *54*(5), 3290–3312, doi:10.1029/2017WR021674.

Vallado, D. (2001), *Fundamentals of astrodynamics and applications*, vol. 12, Springer.

Velicogna, I., and J. Wahr (2006), Acceleration of greenland ice mass loss in spring 2004, *Nature*, *443*(7109), 329–331.

Velicogna, I., T. C. Sutterley, and M. R. vanden Broeke (2014), Regional acceleration in ice mass loss from Greenland and Antarctica using GRACE time-variable gravity data, *Geophysical Research Letters*, *41*(22), 8130–8137, doi:10.1002/2014GL061052.

Wahr, J. (2009), Time variable gravity from satellites, in *Treatise on Geophysics: Geodesy*, edited by G. Schubert and T. Herring, chap. 8, pp. 213–237, Elsevier, Amsterdam, the Netherlands.

Wahr, J., M. Molenaar, and F. Bryan (1998), Time variability of the earth's gravity field: Hydrological and oceanic effects and their possible detection using grace, *Journal of Geophysical Research: Solid Earth*, *103*(B12), 30,205–30,229.

Wahr, J., S. Swenson, and I. Velicogna (2006), Accuracy of GRACE mass estimates, *Geophysical Research Letters*, *33*(6), doi:10.1029/2005GL025305.

Wahr, J., R. S. Nerem, and S. V. Bettadpur (2015), The pole tide and its effect on GRACE time-variable gravity measurements: Implications for estimates of surface mass variations, *Journal of Geophysical Research: Solid Earth*, *120*(6), 4597–4615, doi:10.1002/2015JB011986.

Watkins, M. M., D. N. Wiese, D.-N. Yuan, C. Boening, and F. W. Landerer (2015), Improved methods for observing Earth's time variable mass distribution with GRACE using spherical cap mascons: Improved Gravity Observations from GRACE, *Journal of Geophysical Research: Solid Earth*, *120*(4), 2648–2671, doi:10.1002/2014JB011547.

Xia, Y., et al. (2012), Continental-scale water and energy flux analysis and validation for the North American Land Data Assimilation System project phase 2 (NLDAS-2): 1. Intercomparison and application of model products, *Journal of Geophysical Research: Atmospheres*, *117*(D3), n/a–n/a, doi:10.1029/2011JD016048.

Zaitchik, B. F., M. Rodell, and R. H. Reichle (2008), Assimilation of GRACE Terrestrial Water Storage Data into a Land Surface Model: Results for the Mississippi River Basin, *Journal of Hydrometeorology*, *9*(3), 535–548, doi:10.1175/2007JHM951.1.

Zhang, X., S. Okubo, Y. Tanaka, and H. Li (2016), Coseismic gravity and displacement changes of Japan Tohoku earthquake (Mw 9.0), *Geodesy and Geodynamics*, *7*(2), 95–100, doi:10.1016/j.geog.2015.10.002.

Zwally, H. J., J. Li, J. W. Robbins, J. L. Saba, D. Yi, and A. C. Brenner (2015), Mass gains of the Antarctic ice sheet exceed losses, *Journal of Glaciology*, doi:10.3189/2015JoG15J071.

Appendix A

Mascon Visualization Tool

In conjunction with this thesis, an extensive set of skills were developed working with not only the GSFC mascon solution but also the JPL mascon solution. These solutions differ in many ways, from the background models used to determine the least squares reference state, to the processing assumptions, to the realization of the gravity as a set of mascons itself. This last difference makes comparisons between the two solutions somewhat challenging, and even makes moving from one solution to the other less than straightforward. During the development of this thesis, a collaborative opportunity presented itself with a simple yet nonetheless challenging goal: develop a platform where GRACE mascon products can be analyzed according to their own unique requirements in a straightforward manner where it is difficult to use the data incorrectly.

To achieve this goal, an extensive amount of work was put into building the Mascon Visualization Tool (MVT), a Javascript-based web platform where users can analyze local, basin, and regional signals of interest from both the GSFC and JPL mascon solutions with just a few mouse clicks. As part of this platform, users are able to download data and plots from their analyses for use elsewhere in their own research. As a result, this platform has created what might be considered a brand new "Level 4" GRACE product type aimed at non-experts and experts alike and not even requiring the user download gridded data products that are made available as user-friendly "Level 3" data types. The site continues to be updated, with support from Bryant Loomis at GSFC and David Wiese at JPL, the primary points of contact for each center's mascon solution, and through the ongoing support of Steve Nerem and CCAR. The MVT was publicly introduced at the GRACE

Science Team Meeting in Austin, TX in 2017, but has been in use since mid-2016 (*Croteau and Nerem*, 2016).

The MVT began as a simple tool to look at local signals in the JPL mascon solution. A user could click a location on a map and a plot of the time series at that location would be presented. Over time, this platform grew and expanded, and today users can investigate trends and annual signals, compute local, basin, and continental mass change, and select subsets of the GRACE time series for more specific investigations. Figure A.1 depicts the tool interface, with a time series of a single mascon in Colorado plotted and a trend map for the JPL RL06 mascon solution for the entire GRACE mission depicted in the background.

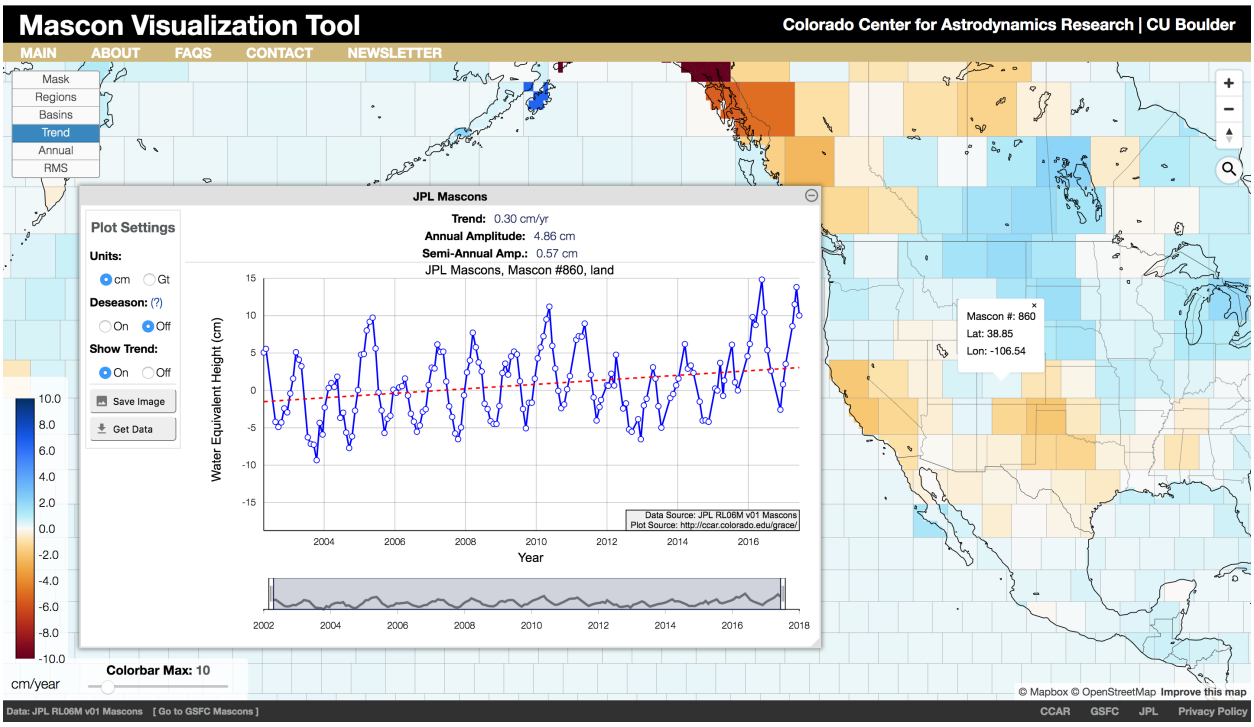

Figure A.1: Mascon Visualization Tool interface, showing TWS for a single mascon in Colorado with a trend map over the entire GRACE timeframe in the background from the JPL RL06 mascon solution.

The MVT has seen considerable user growth since its public introduction. While hundreds of researchers were already using the tool prior to that official launch, the site as seen considerable

growth in the year since. Through November 15, 2018, over 1,800 individual users were tracked for the site, from 48 states and 91 countries.

Technologies used in building this site include but are not limited to:

- Mapbox GL JS Javascript mapping library
- D3.js Javascript visualization library
- Custom mascon and plotting Javascript code
- Matlab and Python 3.6

As of the publication of this dissertation, the MVT is available at: http://ccar.colorado.edu/grace/. Complete documentation for the tool and data products used is available on the site.

Appendix B

Fast vectorized spherical harmonic computations in MATLAB

As part of work building to this thesis, extensive use of GRACE Level 2 spherical harmonic solutions and other spherical harmonic datasets required the heavy optimization of inherited Matlab code for computations in Equations 2.41 and 2.48. The code takes advantage of extensive pre-computations and Matlab's vector math operations to see a more than 20× increase over naive implementations and 2× speed performance over other optimized versions of the original software. Extra features of the code have been simplified and is presented here for archival and reference purposes.

```
function [lons,lats,weq_grid,N_grid] = calc_Earth_gravity(C,S,Nmax,block_size)
% CALC_EARTH_GRAVITY_GRIDS_FASTER calculates various Earth gravity grids
% for a set of spherical harmonic coefficients.  This is a speed-optimized
% version of 'calc_Earth_gravity_grids.m' from Bryant Loomis and others.
%-
% block_size = 0.5;
% [lons,lats,weq_grid,N_grid] = calc_Earth_gravity(C,S,Nmax,block_size);
%-
% INPUTS:
%     Variable          Description
%     --------------    ---------------
%     C                 Cosine harmonic coeffs,      size: [Nmax+1, Nmax+1]
%     S                 Sine harmonic coeffs,        size: [Nmax+1, Nmax+1]
%     Nmax              Max degree/order of spherical harmonic expansion
%     block_size        Size (deg) of equal-angle grids for grid
%
% OUTPUTS:
%     Variable          Description                  Units
%     --------------    ---------------              ---------
%     lambda            Longitude array              [deg]
%     phi               Latitude array               [deg]
```

```
%     weq_grid          Water equivalent height grid    [cm H2O]
%     N_grid            Geoid height grid               [m]
%
% ------------------------------------------------------------------------
% Based on 'calc_Earth_gravity_grid.m' by B. Loomis, M. Croteau, T. Rebold.
% Author: Michael Croteau

% Load Love Numbers
load('love_hkl_N719.mat')
h = love.data(:,2);
k = love.data(:,3);

% Truncate expansion if degree exceeds degree of love numbers:
NLove = length(k)-1;
if Nmax > NLove
    fprintf('Cannot plot higher than Nmax=%i. ', NLove);
    fprintf('Expansion will be truncated.\n\n');
    Nmax = NLove;
end

% Truncate love numbers if expansion is smaller than love numbers:
if NLove > Nmax
    if (calc_sum_vdisp > 0)
        h = h(1:(Nmax+1));
    end
    k = k(1:(Nmax+1));
end

% Precompute n-indexed scale factors:
if (calc_sum_deltaG > 0)
    nsf_2nplus1_over_1plusk = (2*(0:Nmax)'+1) ./ (1+k); % [Nmax+1, 1]
end

% Load constants from function at bottom:
rho_water = 1000;     % [kg/m^3]  Density of Water
rho_Earth = 5517;     % [kg/m^3]  Dens of Earth
rE  = 6378136.3;      % [m]       Radius of Earth
muE = 398600.4415e9;  % [m^3/s^2] Earth Gravitational Parameter
m2cm = 100;           % 1 [m] = 100 [cm]
CONST  = (rE*rho_Earth)/(3*rho_water); % Constant for water equiv height

% Define latitudes (phi) and longitudes (lambda)
bso2 = block_size/2;
phi = ((-90+bso2):block_size:(90-bso2)) * pi/180;
lambda = ((-180+bso2):block_size:(180-bso2)) * pi/180;
l_lam = length(lambda);
l_phi = length(phi);
```

```
% Precompute 'cos m lambda', 'sin m lambda', and 'sin phi' terms:
ems = (0:Nmax)';
cos_m_lambda = cos(ems*lambda); % [Nmax+1, l_lam]
sin_m_lambda = sin(ems*lambda); % [Nmax+1, l_lam]
sin_phi      = sin(phi);        % [1,      l_phi]

% Calculate base grids from C and S
sum_N      = zeros(l_phi,l_lam);  end
sum_deltaG = zeros(l_phi,l_lam);  end

for n=2:Nmax % Loop through n,m to calculate grids:
    in = n+1;

    Pnm = legendre(n,sin_phi,'sch');
    renorm = sqrt(2*n+1);
    renormed_Pnm = zeros(l_phi,Nmax+1);
    renormed_Pnm(:,1:in) = renorm * Pnm';

    sum_Ynm = zeros(l_phi,l_lam);
    for m=0:n
        im = m+1;
        sum_Ynm = sum_Ynm + renormed_Pnm(:,im) * ...
            (C(in,im)*cos_m_lambda(im,:) + S(in,im)*sin_m_lambda(im,:));
    end

    sum_N = sum_N + sum_Ynm;
    sum_deltaG = sum_deltaG + nsf_2nplus1_over_1plusk(in) * sum_Ynm;
end

% Calculate grids to output based on what was called in 'output_grids':
lats = phi * 180/pi;
lons = lambda * 180/pi;
weq_grid = CONST * sum_deltaG * m2cm;
N_grid = rE * sum_N;

end % END OF MAIN FUNCTION
```

Appendix C

Executive Summary

Traditional GRACE solutions provide monthly high spatial resolution time-variable gravity estimates. These estimates are useful in applications spanning hydrology, cryosphere, oceans, and more, but their monthly realizations lead to problems using GRACE data when sub-monthly information is needed. The GRACE orbit design results in approximately 15 evenly spaced daily orbits, and the daily orbit coverage propagates longitudinally each day. Most GRACE solutions compile these observations in monthly increments, resulting in a high density of time-variable gravity field observations for informing the monthly solution, but this results in daily variations over the span of each month being aliased in the resulting gravity field estimate. For applications such as drought monitoring, flood prediction, data assimilation, and GRACE-informed mass balance models, better temporal coverage would allow GRACE to better inform these efforts.

This dissertation presents an analysis of a new, unique daily GRACE estimate of terrestrial water storage. Resolution of the new solution is quantified and basin estimates of TWS are compared with models. Validated by simulation results, the new daily solution is shown to recover estimates of water storage with approximately 400 km resolution at the poles and 800 km resolution at the equator. This distinct latitudinal dependence on signal resolution results from the GRACE orbit geometry, which provides better coverage at higher latitudes. The newly developed daily solution is shown to successfully capture meaningful water storage signals on daily timescales with quantified leakage errors. These findings and errors hold promise in addressing the many needs for better temporal information from GRACE.